

Absolute Determination of the  $^{22}\text{Na}(p, \gamma)^{23}\text{Mg}$  Reaction Rate:  
Consequences for Nucleosynthesis of  $^{22}\text{Na}$  in Novae

A. L. S.

A dissertation submitted in partial fulfillment of  
the requirements for the degree of

Doctor of Philosophy

University of Washington

2010

Program Authorized to Offer Degree: Physics Department

University of Washington

## Abstract

### Absolute Determination of the $^{22}\text{Na}(p, \gamma)^{23}\text{Mg}$ Reaction Rate: Consequences for Nucleosynthesis of $^{22}\text{Na}$ in Novae

Hydrodynamic simulations of classical novae on ONe white dwarfs predict substantial production of  $^{22}\text{Na}$ . Observation of  $^{22}\text{Na}$  decay should be correlated with the corresponding nova because the half life of  $^{22}\text{Na}$  is only 2.6 years. The 1275-keV gamma ray from the  $\beta$  decay of  $^{22}\text{Na}$  is, therefore, an excellent diagnostic for the nova phenomenon and a long-sought target of gamma-ray telescopes. Nova simulations determine the maximum  $^{22}\text{Na}$ -detection distance to be  $< 1$  kpc for the INTEGRAL spectrometer SPI, consistent with its non-observation to date. However, model estimates are strongly dependent on the thermonuclear rate of the  $^{22}\text{Na}(p, \gamma)^{23}\text{Mg}$  reaction, which is the main destruction mechanism of  $^{22}\text{Na}$  in novae. The  $^{22}\text{Na}(p, \gamma)^{23}\text{Mg}$  rate is expected to be dominated by narrow, isolated resonances with  $E_p < 300$  keV. The currently employed rate is based on a single set of absolute resonance-strength measurements with  $E_p \geq 290$  keV, and one relative measurement of resonances with  $E_p \geq 214$  keV. Recently, a new level has been found in  $^{23}\text{Mg}$  which would correspond to a resonance at  $E_p = 198$  keV that might dominate the reaction rate at nova temperatures.

We have measured the  $^{22}\text{Na}(p, \gamma)^{23}\text{Mg}$  resonance strengths directly and absolutely, in addition to resonance energies and branches. Proton beams were produced at the University of Washington and delivered to a specially designed beam line that included rastering and cold vacuum protection of the  $^{22}\text{Na}$ -implanted targets (fabricated at TRIUMF-ISAC). Two high-purity germanium detectors were employed and surrounded by anticoincidence shields to reduce cosmic backgrounds. Measurements

were made on known  $^{22}\text{Na} + p$  resonances, which we observed at laboratory energies  $E_p = 213, 288, 454, 610 \text{ keV}$  and on proposed resonances at  $E_p = 198, 209,$  and  $232 \text{ keV}$ . The proposed resonances were not observed, and the upper limit placed on the 198-keV resonance strength indicates that the resonance at  $E_p = 213 \text{ keV}$  still dominates the reaction rate across the temperature range important to novae. However, we measured the strengths of the known resonances to be higher than previous direct measurements by factors of 2.4 to 3.2. Using both post-processing network calculations and hydrodynamic simulations to estimate the effect of the new  $^{22}\text{Na}(p, \gamma)^{23}\text{Mg}$  reaction rate, we find the amount of  $^{22}\text{Na}$  produced by novae to be lower by a factor of 2 from current estimates, revising the prospects for its observation. Full analysis of results are presented. Experimental improvements and future prospects are discussed.

## TABLE OF CONTENTS

	Page
List of Figures . . . . .	iv
List of Tables . . . . .	vi
Chapter 1: Introduction . . . . .	1
1.1 Motivation . . . . .	1
1.2 The Experiment: Measuring the $^{22}\text{Na}(\text{p},\gamma)$ Reaction Rate . . . . .	2
1.2.1 Strategy . . . . .	4
1.2.2 Challenges . . . . .	5
1.3 Previous Measurements of $^{22}\text{Na}(\text{p},\gamma)$ Resonances . . . . .	6
1.3.1 Seuthe . . . . .	7
1.3.2 Stegmüller . . . . .	9
1.3.3 Jenkins . . . . .	10
Chapter 2: Theory . . . . .	12
2.1 Stellar Evolution . . . . .	12
2.2 Stellar Death and Nucleosynthesis . . . . .	15
2.3 Nova Nucleosynthesis . . . . .	21
2.3.1 White Dwarf Mechanics . . . . .	26
2.4 Nuclear Reactions . . . . .	27
2.4.1 Structure of the Nucleus and Selection Rules . . . . .	28
2.4.2 Decays . . . . .	31
2.4.3 A( $x,\gamma$ )B Reactions . . . . .	32
Non-resonant Reactions . . . . .	32
Resonant Reactions . . . . .	33
2.5 Thermonuclear Reaction Rates . . . . .	37
2.5.1 Narrow Resonance Reaction Rates . . . . .	38
2.6 Reaction Yield in the Laboratory . . . . .	39
2.6.1 Thick-Target Yield: Peak Method . . . . .	40

2.6.2	Thick-Target Yield: Integrated Method . . . . .	40
Chapter 3:	Experimental Setup . . . . .	43
3.1	Chamber . . . . .	44
3.1.1	Cold Shroud . . . . .	44
3.1.2	Apertures . . . . .	45
3.1.3	Target Mount . . . . .	46
3.2	Detectors . . . . .	47
3.2.1	High-Purity Germanium Detectors . . . . .	48
Shielding	. . . . .	48
3.2.2	Cosmic-Ray Anticoincidence Shields . . . . .	49
3.3	Data Acquisition . . . . .	53
3.3.1	Signals: Amplitude, TAC/Veto, Scalers . . . . .	54
TAC	. . . . .	56
3.3.2	Rastering . . . . .	58
3.4	Targets . . . . .	60
3.4.1	$^{22}\text{Na}$ Targets . . . . .	61
3.4.2	$^{23}\text{Na}$ Targets . . . . .	63
Chapter 4:	Characterization of Experimental Properties . . . . .	66
4.1	Detector Efficiency . . . . .	66
4.1.1	Direct measurements: $^{60}\text{Co}$ , $^{24}\text{Na}$ , $^{27}\text{Al}$ . . . . .	66
4.1.2	PENELOPE Simulations . . . . .	67
4.1.3	Systematic Errors for the Efficiency . . . . .	71
4.2	Initial Total Number of Target Atoms . . . . .	71
4.3	Beam Properties . . . . .	72
4.3.1	Normalized Beam Density . . . . .	72
4.3.2	Beam Energy Calibration with $^{27}\text{Al}(p, \gamma)$ . . . . .	74
Chapter 5:	$^{22}\text{Na}(p, \gamma)$ Measurements and Analysis . . . . .	76
5.1	Absolute yields: $E_p = 610, 454, 288, 213$ keV . . . . .	77
5.2	Upper limits for yield: $E_R = 232, 198, 209$ keV . . . . .	78
5.3	Corrected area for $E_R = 213$ keV . . . . .	90
5.4	Degradation in the Total Number of Target Atoms . . . . .	90
5.5	Resonance Energies . . . . .	93
5.5.1	Doppler, Recoil, and Rate-Dependent Corrections . . . . .	94

5.6	Branches . . . . .	95
5.7	Verification of Experimental Method: $^{23}\text{Na}(p, \gamma)$ Measurement . . . . .	96
5.7.1	Area Correction . . . . .	97
Chapter 6: Results and Discussion . . . . .		99
6.1	Resonance Energies . . . . .	99
6.2	Branches . . . . .	99
6.3	Resonance Strengths . . . . .	101
Chapter 7: Astrophysical Implications . . . . .		107
7.1	Re-evaluating the Thermonuclear Reaction Rate of $^{22}\text{Na}(p, \gamma)^{23}\text{Mg}$ . . . . .	107
7.2	Consequences for Nucleosynthesis of $^{22}\text{Na}$ . . . . .	110
Chapter 8: Conclusions, Improvements, and Future Prospects . . . . .		114
Bibliography . . . . .		116

## LIST OF FIGURES

Figure Number		Page
1.1	$^{22}\text{Na}(p, \gamma)$ thermonuclear reaction rate according to Ref. [1] . . . . .	3
1.2	Decay scheme of $^{22}\text{Na}$ . . . . .	6
2.1	Quantitative Hertzprung-Russell diagram . . . . .	13
2.2	Qualitative Hertzprung-Russell diagram . . . . .	13
2.3	Three sample lifecycles of stars . . . . .	13
2.4	Chart of nuclides . . . . .	14
2.5	Sample stellar burning cycle . . . . .	16
2.6	Overproduction factors for different nova models . . . . .	18
2.7	Nova Cygni 1992 . . . . .	20
2.8	Scheme of nova explosion . . . . .	21
2.9	CNO cycle . . . . .	23
2.10	NeNa reaction cycle . . . . .	24
2.11	Energy level diagram for $^{23}\text{Mg}$ . . . . .	25
2.12	White dwarf radius as a function of mass . . . . .	28
2.13	Scheme of direct capture . . . . .	32
2.14	Scheme of resonant capture . . . . .	32
2.15	Breit-Wigner cross section . . . . .	37
3.1	Panorama of $0^\circ$ beamline . . . . .	43
3.2	Chamber cross section . . . . .	44
3.3	Cooling of cold shroud . . . . .	45
3.4	Photo of target and mount . . . . .	46
3.5	Top view of detector setup . . . . .	47
3.6	Photo of detector setup. . . . .	48
3.7	Photo of detector setup, close-up. . . . .	48
3.8	Cross section of germanium detector. . . . .	49
3.9	Background spectrum . . . . .	50
3.10	Photo of cosmic ray shields . . . . .	51
3.11	Sketch of anticoincidence concept . . . . .	51

3.12	Effect of anticoincidence shielding for test setup . . . . .	52
3.13	Electronics diagram . . . . .	55
3.14	TAC spectrum . . . . .	57
3.15	Energy verses TAC spectrum . . . . .	57
3.16	Effect of anticoincidence shielding . . . . .	58
3.17	Sample raster plot . . . . .	59
3.18	TRIM simulation of implantation depth . . . . .	60
3.19	$^{22}\text{Na}$ target distribution . . . . .	62
3.20	Sketch of $^{23}\text{Na}$ implantation setup . . . . .	64
4.1	Cross section of simulated detector geometry . . . . .	67
4.2	Sample PENELOPE spectrum . . . . .	68
4.3	Simulated photopeak efficiency and its agreement with measurement . . . . .	69
4.4	Sample $^{27}\text{Al}(p, \gamma)$ excitation function . . . . .	74
4.5	Beam-energy calibration . . . . .	75
5.1	Excitation functions for $E_p = 454$ keV, 610 keV . . . . .	79
5.2	Summed gamma-ray spectra for $E_p = 454$ , 610 keV . . . . .	80
5.3	Raster plot for $^{22}\text{Na}(p, \gamma)$ with target #3 . . . . .	81
5.4	Excitation functions for $E_p = 288$ , 213 keV . . . . .	82
5.5	Summed gamma-ray spectra for $E_p = 288$ , 213 keV . . . . .	83
5.6	Excitation functions for $E_p = 232$ , 198 keV . . . . .	84
5.7	Summed gamma-ray spectra for $E_p = 232$ , 198 keV . . . . .	85
5.8	2D $\chi^2$ plot for $E_p = 198$ keV . . . . .	86
5.9	2D $\chi^2$ plot for $E_p = 232$ keV . . . . .	87
5.10	Excitation function for $E_p = 209$ keV . . . . .	89
5.11	2D $\chi^2$ plot for $E_p = 209$ keV . . . . .	89
5.12	Target degradation as a function of implanted charge . . . . .	91
5.13	Excitation function for $^{23}\text{Na}(p, \gamma)$ . . . . .	96
5.14	Large amplitude raster plot for $^{23}\text{Na}(p, \gamma)$ . . . . .	97
5.15	Model of the target to estimate missing area. . . . .	97
7.1	Thermonuclear $^{22}\text{Na}(p, \gamma)^{23}\text{Mg}$ reaction rate as a function of temperature . . . . .	108
7.2	Relative reaction rate . . . . .	109
7.3	$^{22}\text{Na}$ predicted abundance as a function of $^{22}\text{Na}(p, \gamma)$ reaction rate . . . . .	110

## LIST OF TABLES

Table Number	Page
2.1 Properties of cosmic gamma-ray emitters . . . . .	17
2.2 Multipole moments . . . . .	30
4.1 Numerical efficiency comparison of simulation to measurement . . . . .	70
5.1 Summary of $^{22}\text{Na}(p, \gamma)$ gamma-ray energies . . . . .	76
6.1 Resonance energies . . . . .	100
6.2 Branches and partial strengths . . . . .	104
6.3 Systematic error summary . . . . .	105
6.4 Resonance strengths . . . . .	106
7.1 Reaction rate . . . . .	111
7.2 Results from hydrodynamic simulation . . . . .	113

## Chapter 1

### INTRODUCTION

Classical novae are an excellent laboratory in which to explore the details of explosive nucleosynthesis. Nova temperatures are high enough to ignite a chain of nucleosynthetic processes far above what main sequence stars can synthesize, yet they remain low relative to other explosive events. Therefore, before attempting to deconstruct much hotter and more complicated events such as supernovae, it is beneficial to unravel the nova system. A key to demystifying explosive nucleosynthesis in general is the detection of specific radionuclides in our Galaxy. The elusive  $^{22}\text{Na}$  radionuclide is thought to be produced by nova and Type II supernova explosions and has yet to be observed by orbiting gamma-ray telescopes. This isotope, in particular, is pivotal because its half life (2.6 yr) is long enough to survive the explosion yet short enough to allow identification of its progenitor star. Although other radionuclides have been observed, as discussed in Sec. 2.2, none have this unique property and are specifically associated with nova outbursts above other astrophysical phenomena. With the aid of low-energy accelerators and radioactive targets, one can recreate some of these important reactions directly in a laboratory setting and aid in validating or nullifying theoretical models of these violent stellar events.

#### 1.1 *Motivation*

A classical nova is the consequence of thermonuclear runaway on the surface of a white-dwarf star that is accreting hydrogen-rich material from its partner in a binary system. Discussed in detail in Sec. 2.3, such novae are ideal sites for the study of explosive nucleosynthesis because the observational [2], theoretical [3, 4], and nuclear-experimental [5, 6] aspects of their study are each fairly advanced. In particular, due to the relatively low peak temperatures in nova outbursts ( $0.1 < T < 0.4$  GK), most of the nuclear reactions involved are not too far from the valley of beta stability to be studied in the laboratory, and the corresponding thermonuclear reaction rates are mostly based on experimental information [5]. It may also be quite helpful to obtain a more firm grasp of nova

nucleosynthesis before venturing to the more complicated system of nucleosynthesis in supernovae.

It is important to reduce uncertainties in the rates of key reactions that are expected to affect the production of  $^{22}\text{Na}$  so that accurate comparisons can be made between observations and models [7]. The production of  $^{22}\text{Na}$  in novae depends strongly on the thermonuclear rate of the  $^{22}\text{Na}(p, \gamma)^{23}\text{Mg}$  reaction [5, 7, 8], which is the predominant mechanism for destruction of  $^{22}\text{Na}$ . The thermonuclear  $^{22}\text{Na}(p, \gamma)$  reaction rate in novae is dominated by narrow, isolated resonances with laboratory proton energies  $E_p < 300$  keV. Consequently, the rate is dependent on the energies and strengths of these resonances, which have been investigated both indirectly and directly in the past. Indirect information on potential  $^{22}\text{Na}(p, \gamma)$  resonances has been derived from measurements of the  $^{24}\text{Mg}(p, d)$  [9],  $^{25}\text{Mg}(p, t)$  [10], and  $^{22}\text{Na}(^3\text{He}, d)$  [11] reactions, and from the beta-delayed proton- and gamma-decays of  $^{23}\text{Al}$  [12, 13, 14]. The first published attempt to measure the  $^{22}\text{Na}(p, \gamma)$  reaction directly employed a chemically prepared, radioactive  $^{22}\text{Na}$  target and produced only upper limits on the resonance strengths [15]. A measurement contemporary to Ref. [15] in the range  $E_p > 290$  keV by Seuthe *et al.* employed ion-implanted  $^{22}\text{Na}$  targets [16], resulting in the first direct observation of resonances and the only absolute measurement of resonance strengths. Later, Stegmüller *et al.* [17] discovered a new resonance at 213 keV and determined its strength relative to the strengths from Ref. [16]. More recently, a new level in  $^{23}\text{Mg}$  ( $E_x = 7770$  keV) has been discovered using the  $^{12}\text{C}(^{12}\text{C}, n\gamma)$  [1] reaction. This level corresponds to a  $^{22}\text{Na}(p, \gamma)$  laboratory proton energy of 198 keV, and the authors of Ref. [1] proposed that this potential resonance could dominate the  $^{22}\text{Na}(p, \gamma)$  reaction rate at nova temperatures, shown in Fig. 1.1. With the advent of radioactive ion-beam facilities coming online in the last decade, the doors have been opened to directly explore (in inverse kinematics) a plethora of reactions relevant to nuclear astrophysics which have previously been unmeasurable; however, the  $^{22}\text{Na}$  half life is long enough that a direct measurement in regular kinematics is still a viable option.

## 1.2 The Experiment: Measuring the $^{22}\text{Na}(p, \gamma)$ Reaction Rate

We have measured the energies, strengths, and branches of known resonances [16, 17] and searched for proposed [1, 12, 13, 14] resonances in the energy range  $E_p \sim 195$  to 630 keV. The measurements were performed on a new 0° beamline of the tandem Van de Graaff accelerator at the Center for

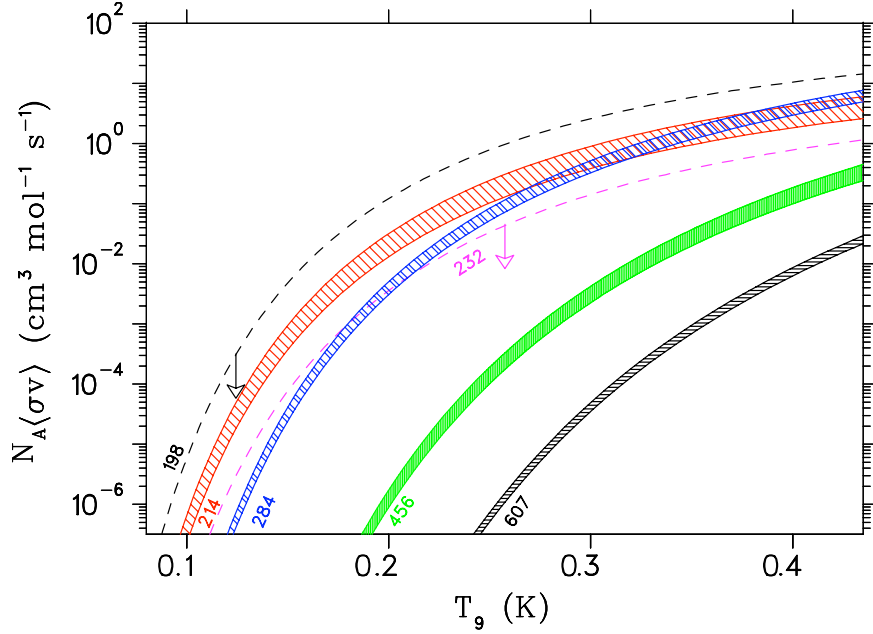


Figure 1.1: Individual resonance contributions to the thermonuclear reaction rate for  $^{22}\text{Na}(p, \gamma)$  derived from the strengths and energies tabulated in Jenkins *et al.* [1]. Uncertainties shown are calculated analytically.

Experimental Nuclear Physics and Astrophysics (CENPA) of the University of Washington with ion-implanted  $^{22}\text{Na}$  targets prepared at TRIUMF-ISAC. To achieve high currents at low energies, we utilized a terminal ion source (TIS). Two high-purity 100% (as compared to 3 in  $\times$  3 in NaI) germanium (HPGe) detectors were used at  $\pm 55^\circ$  to the beam axis to detect the gamma rays produced from the bombardment of protons on the  $^{22}\text{Na}$  target. Because of the harsh environment generated from the radioactivity, 26 mm of lead was placed between the detector and the target to lower the detector rate to an acceptable level. Although the radioactivity provides an extremely large background signal around 1 MeV, the dominant background signal (not beam-related) in the energy region of interest to the resonance measurements ( $\sim 5$  MeV) is from cosmic rays. Therefore, cosmic-ray anticoincidence shields, consisting of planar and annular plastic scintillator detectors surrounded by lead, were installed around each germanium detector. Thanks to evaporated protective layers [18], the targets exhibited little to no degradation over  $\sim 20$  C of bombardment. Using mainly the strengths and energies obtained in this work together with supplemental information

from other work [16, 19], we have re-evaluated the thermonuclear reaction rate of  $^{22}\text{Na}(p, \gamma)$ , and full hydrodynamic simulations have been performed to estimate the effect of the new rate on the flux of  $^{22}\text{Na}$  from novae. This is a detailed presentation of our experiment, its results, and their implications, expanding on our previous reports [20, 21].

### 1.2.1 Strategy

The number of reactions,  $N_R$ , produced by a beam of incident particles with areal density  $dN_b/dA$  on a target with areal density  $dN_T/dA$  is given by

$$N_R = \sigma \int \frac{dN_T}{dA} \frac{dN_b}{dA} dA, \quad (1.1)$$

where  $\sigma$  is the cross section. Conventional methods employ a small-diameter beam that impinges on a large-area target, where the target density is nearly uniform. However, this technique can lead to target damage in cases where large beam currents are used, and there is a long history of differing results on resonance strengths that have been attributed to target instabilities [22, 23, 24, 25]. We designed our experiment closer to the opposite limit, similar to Ref. [26], where the beam was swept over an area larger than the full extent of the target with a rastering device. In the limit of uniform beam density over the target area, Eq. 1.1 becomes

$$N_R = \sigma N_T \frac{dN_b}{dA}. \quad (1.2)$$

This method requires knowledge of only the *total* number of target atoms and, thus, is not very sensitive to target non-uniformities. On the other hand, this method also requires a determination of the beam density. The reaction yield,  $Y$ , is defined as the number of reactions per incident particle [27] and is given by

$$Y = \sigma N_T \rho_b, \quad (1.3)$$

where  $\rho_b = \frac{dN_b}{dA}/(Q/e)$  is a beam density normalized to the accumulated charge,  $Q$ .

In addition, we determined the *integrated yield* of the excitation function over the beam energy, minimizing uncertainties associated with the energy loss in the target and beam energy distribution, which can be substantial in determinations using only the yield at a particular energy. The latter method, which was used in Ref. [16], depends on knowing the energy loss in the target, the tar-

get stoichiometry and uniformity, and often assumes stable target conditions, which are unlikely in experiments with currents of tens of microamps, such as ours.

Beginning with Eq. 1.3, the integrated yield for a finite-thickness target is given by

$$\int Y_i dE = 2\pi^2 \lambda^2 \frac{m+M}{M} N_T \rho_b \omega \gamma_i, \quad (1.4)$$

where  $\int Y_i dE$  is the integral over the laboratory beam energy  $E$  with a range spanning the resonance for branch  $i$ ,  $m$  is the projectile mass,  $M$  is the target mass, and  $\omega \gamma_i$  is the partial resonance strength. The total resonance strength,  $\omega \gamma$ , is simply equal to the sum of the partial strengths for all branches.  $\lambda$  is the center-of-mass de Broglie wavelength and is given by:

$$\lambda = \frac{m+M}{M} \frac{\hbar}{\sqrt{2mE_{\text{lab}}}}. \quad (1.5)$$

A complete derivation of Eq. 1.4 is given in the next chapter.

### 1.2.2 Challenges

Although this experiment was straightforward in theory—proton beams bombard a target, and the gamma rays produced in the reaction are detected—it was quite challenging in practice. The main challenge was acquiring data in a very harsh radioactive environment.  $^{22}\text{Na}$  beta decays to an excited state of  $^{22}\text{Ne}$ , which then de-excites to the ground state by emitting a 1275-keV gamma ray, as shown in Fig. 1.2. In the substrate, the positron annihilated with an electron, producing two 511-keV gamma rays. This onslaught of 511- and 1275-keV gamma rays led to very high detector rates, which in turn caused massive detector dead times. In addition to high detector thresholds, shielding was necessary to decrease detector rate, and the details are discussed in Sec. 3.2.1.

Another challenge for this experiment was that the resonance strengths are weak, ranging from only a few meV to a few hundred meV due to the Coulomb barrier at low proton energies. As is derived in the next chapter, the reaction rate is proportional to the negative exponential of the resonance energy, so even resonances with very weak strengths can have significant contributions to the total rate if the corresponding proton energy is low. Weak resonances signify that copious amounts of data for extended periods of time or high beam currents are needed to achieve decent statistics. This in turn could cause target degradation, another non-trivial experimental challenge. Longer or more intense irradiations begin to erode any protective layer and then the target substrate. Because

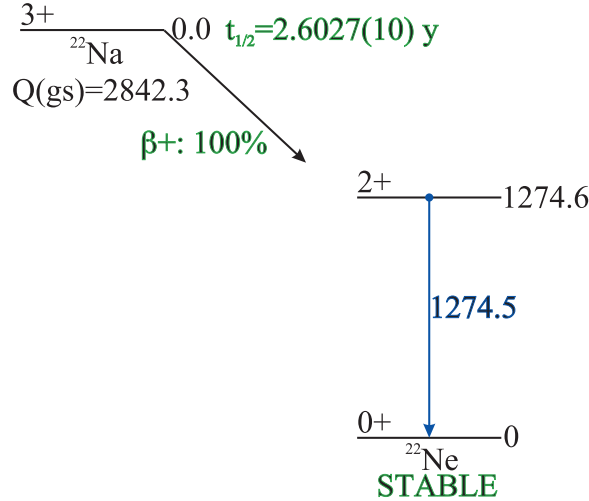


Figure 1.2: Decay scheme of  $^{22}\text{Na}$ .

we integrated resonance yields, our method was not very sensitive to evolving target distributions within the substrate due to proton bombardment; however, the possible sputtering of  $^{22}\text{Na}$  nuclei out of the substrate does affect our method and must be taken into account. Characterizing this transformation can be very difficult so much effort was expended to design targets which suffered minimal degradation [18]. Target fabrication is discussed in Sec. 3.4, and details of possible degradation and how it was handled in the analysis are outlined in Sec. 5.4.

### 1.3 Previous Measurements of $^{22}\text{Na}(p,\gamma)$ Resonances

In 1990, Seuthe *et al.* [16] was the first to measure the strengths of the  $^{22}\text{Na}(p,\gamma)$  reaction rate directly and absolutely. In 1996, Stegmüller *et al.* [17] followed with a direct, relative measurement and discovered an additional resonance at  $E_p = 213$  keV and concluded that it dominated the reaction rate. Eight years later, Jenkins *et al.* [1] performed an indirect measurement of the rate using heavy-ion fusion of  $^{12}\text{C} + ^{12}\text{C}$ , which unveiled a new level in  $^{23}\text{Mg}$ . The corresponding  $^{22}\text{Na}(p,\gamma)$  resonance to this level would supersede all others for nova temperatures if its strength was found to be on the order of 4 meV. The following subsections detail each of these key papers, leading to previous determinations of the  $^{22}\text{Na}(p,\gamma)$  reaction rate.

### 1.3.1 Seuthe

Before the experiment detailed in this dissertation was conducted, the measurement by Seuthe *et al.* [16] was the first and only direct, absolute measure of  $^{22}\text{Na}(p, \gamma)$  resonance strengths. (Previously, only upper limits had been set with chemically fabricated targets [15].) Seuthe *et al.*'s  $^{22}\text{Na}$  targets were ion implanted, like our own; however, with the ISOLDE-II mass separator at CERN, they implanted 700  $\mu\text{Ci}$  into a pure Ni layer ( $40 \text{ mg/cm}^2$  thick) on a 0.2 mm Ta backing at 60 keV. After scanning the target area with a NaI(Tl) detector (similar to our method with a Geiger counter described in Sec. 3.4.1), Seuthe *et al.* estimated that their target was homogenous with a mean radius of  $4.25 \pm 0.25$  mm.

Using the 450-kV Sames accelerator and the 4-MV Dynamitron tandem accelerator at the Ruhr-Universität Bochum, they achieved up to 80  $\mu\text{A}$  proton currents for  $E_p = 0.17\text{-}1.29$  MeV. In their chamber, a 1-m long liquid-nitrogen cold trap was employed with a 9-mm diameter collimator on the downstream end. A thin, copper disc (1 cm downstream of the cold trap and 2 cm upstream of the target) served as an electron suppressor, biased at  $-300$  V, and as a final collimator with an open diameter of 11 mm. The chamber maintained a pressure of  $\sim 2 \times 10^{-7}$  torr, and the target was directly water-cooled. A significant difference between this experiment and our own is the absence of a rastering mechanism for their proton beam. It is possible that their non-rastered beam effectively carved out a hole in the middle of their target, since the intense heat from the beam spot was more concentrated and not moved to different positions on the target continuously throughout bombardment.

Seuthe *et al.* utilized three different detector systems. First was a D<sub>2</sub>O cylindrical tank (242 liters), surrounded by 30  $^3\text{He}$  proportional counters. This detector provides no gamma-ray energy resolution, but because its threshold is at 2.22 MeV for the photodisintegration of deuterium, the detector rate in the presence of the hot  $^{22}\text{Na}$  target was quite low (only a few events per second). Secondly, a separate, exchangeable detector system was installed in a beam pipe passing in the center of the tank at  $0^\circ$  to the beam axis. For low-resolution measurements, a 7.6 cm diameter  $\times$  7.6 cm NaI(Tl) crystal was used and for higher resolution was replaced with a 145 cm<sup>3</sup> intrinsic Ge detector. For reference, our two Ge detectors, discussed in detail in Sec. 3.2.1, *each* had a crystal volume of 356 cm<sup>3</sup> and were protected by cosmic-ray anticoincidence shielding to filter out excess

backgrounds.

Before Seuthe *et al.*'s measurement, no  $^{22}\text{Na}(p, \gamma)$  resonances had ever been observed in the laboratory. Therefore, the first effort was to search for their possible presence with the D<sub>2</sub>O and NaI(Tl) detector combination by stepping in 5 keV increments over the energy range from 0.17–1.29 MeV. Throughout 100 C of deposited charge, this search produced observable resonances at  $E_p = 290, 457, 503, 613, 740$ , and 796 keV. For the resonances at 290- and 613-keV, branches to the second and fourth excited states and to the ground state, first, and second excited states, respectively, were determined with the Ge detector. Because of  $^{22}\text{Na}$  target deterioration and a fivefold increase in backgrounds during the 100 C bombardment, no other resonances yielded meaningful branching information. However, even after 140 C, the  $^{22}\text{Na}$  loss was only 35%. Resonance energy information was obtained with methods similar to ours, described in Sec. 5.5.

In order to extract the resonance strengths, they used the conventional method mentioned in Sec. 1.2.1, whereby a narrow beam irradiates an extended target. This method employs peak yields and a determination of both the target density and effective stopping power. In order to determine the density, the target activity was measured to be  $0.69 \pm 0.07$  mCi with the NaI(Tl) detector. After assuming a spatial distribution as discussed above, a density,  $N_{\text{Na}}$ , of  $(4.3 \pm 0.5) \times 10^{15}$  atoms/cm<sup>2</sup> was calculated. An *effective* stopping power,  $\epsilon_{\text{eff}}$ , was necessary because the active  $^{22}\text{Na}$  atoms were embedded in a matrix of inactive Ni host atoms. This quantity is calculated via:

$$\epsilon_{\text{eff}} = \frac{\Delta_{\text{eff}}}{N_{\text{Na}}} = \epsilon_{\text{Na}} + x\epsilon_{\text{Ni}}, \quad (1.6)$$

where  $\Delta_{\text{eff}}$  is the effective target thickness measured at the 613-keV resonance,  $\epsilon_i$  is the stopping power for  $i = \text{Na}$  or  $\text{Ni}$ , and  $x$  is the ratio of Ni to Na areal density. The extracted value for  $x$  was equal to 130.

Absolute efficiency is a necessary component in both this measurement and in ours. The efficiency was measured with calibrated  $^{60}\text{Co}$  and RdTh sources, in addition to using gamma rays from  $^{15}\text{N}(p, \alpha\gamma)$  and  $^{19}\text{F}(p, \alpha\gamma)$  reactions, and was in good agreement with calculation. Results for the yield from each detector are in fairly good agreement with each other (additionally validating the efficiency determination), and their weighted average was used to calculate the strength. A dead time correction ranging from 10-40% was also applied. There is a notation that in addition to the peak yield analysis, an integrated yield analysis was performed, and the two methods agreed. No

further documentation of this agreement has been published.

Using the same narrow-resonance formalism as our experiment, Seuthe *et al.* also calculated the thermonuclear reaction rate and determined that the resonance at  $E_p = 290$  keV dominated the rate in the temperature region of interest to novae. Contributions from direct capture were also calculated.

### 1.3.2 Stegmüller

Building on the results of Seuthe *et al.* [16], Stegmüller *et al.* [17] also performed a direct (but relative) measurement of the  $^{22}\text{Na}(p, \gamma)$  reaction rate. This group did not attempt an absolute measurement and aimed only to probe the possible resonances at lower energies than Seuthe *et al.* observed, as it is possible for a lower-energy resonance to dominate the reaction rate even with a smaller value for the resonance strength. The accelerator facility utilized by Seuthe *et al.* was also used to measure the resonances, in addition to using a similar experimental setup. Stegmüller *et al.*'s  $^{22}\text{Na}$  targets were also ion-implanted on a Ni backing and had an activity of  $190\ \mu\text{Ci}$  at the time of proton bombardment. A similar target distribution scan was performed with a Ge detector. This target, however, did not withstand bombardment like Seuthe *et al.*'s did: after  $\sim 15$  C, a catastrophic loss of target was discovered, when the peak yield of the 290-keV resonance used to monitor target degradation dove by nearly an order of magnitude due to an increase of the beam current from 60 to  $90\ \mu\text{A}$ . Yet, even up to 11 C, the target had deteriorated by 20%, which is fairly high compared to its predecessor in the Seuthe *et al.* measurement.

Stegmüller *et al.* employed a high-purity Ge detector with 100% efficiency as compared to NaI. A 5-cm thick lead shield was placed between the target and detector to decrease the event rate to an acceptable level. The efficiency was determined using resonances from the  $^{11}\text{B}(p, \gamma)$ ,  $^{14}\text{N}(p, \gamma)$ , and  $^{27}\text{Al}(p, \gamma)$  reactions. An additional element this experiment possessed that ours did not was that all efficiency measurements were carried out in the presence of the strong  $^{22}\text{Na}$  source. (We did, however, verify that this difference in dead time had a negligible effect on our gamma-ray yields (Sec. 3.3), although it did cause a slight shift of the gamma-ray energies (Sec. 5.5.1), which we corrected.)

Stegmüller *et al.* observed a new resonance at  $E_p = 213$  keV and determined the strength

relative to the 290- and 613-keV resonances measured by Seuthe *et al.* Skirting potential problems with peak yields, integrated yields were used to extract the relative strength. As a check, Stegmüller *et al.*'s ratio of the 613- to the 290-keV resonance strength was  $16.1 \pm 1.3$ , as compared to Seuthe *et al.*'s ratio of  $16.8 \pm 4.3$ , which are clearly in stellar agreement. Due to rapid target deterioration that occurred during the bombardment of the 213-keV resonance, its strength was more difficult to extract, and the excitation function had to be split up into three regions with different assumptions about the state of the target. In order to account for unobserved branches, the value of the resonance strength was increased from  $1.4 \pm 0.3$  to  $1.8 \pm 0.7$  meV.

Stegmüller *et al.* also observed a new branch for the 290-keV resonance, and, in the absence of a finite measurement, upper limits were placed on branches to the first four levels of  $^{23}\text{Mg}$  for resonances at  $E_p = 213, 225, 288$ , and 613 keV. The reaction rate was also re-evaluated, which indicated that the newly discovered 213-keV resonance dominated the rate in novae.

### 1.3.3 Jenkins

Using the heavy-ion fusion of  $^{12}\text{C} + ^{12}\text{C}$ , Jenkins *et al.* [1] performed an indirect measure of the  $^{22}\text{Na}(p, \gamma)$  reaction rate. This indirect method avoided the difficulty of 1) fabricating a hot radioactive  $^{22}\text{Na}$  target, and 2) working in its vicinity that could cause not only health and safety problems but massive detector rates and dead times. Jenkins *et al.* populated the particle-unbound states of  $^{23}\text{Mg}$  by bombarding a  $40 \mu\text{g}/\text{cm}^2$  thick  $^{12}\text{C}$  target with a 22 MeV  $^{12}\text{C}$  beam from the ATLAS accelerator at Argonne National Laboratory. Gammasphere, a  $4\pi$  gamma-ray spectrometer consisting of 100 HPGe detectors, was used to detect the following gamma rays with excellent energy resolution.

This measurement indicates there are possible resonances at  $198.2(19)$  and  $209.4(17)$  keV, which have never been observed previously. The potential 198-keV resonance decays to  $9/2^+$  and  $5/2^+$  states (strongest branch), and, by mirror symmetry with the  $^{23}\text{Na}$  nucleus, Jenkins *et al.* associate this initial  $^{23}\text{Mg}$  state with  $9/2^-$ . Further documentation on the rationale behind this assignment was never published. However, if this spin-parity assignment is accurate, Jenkins *et al.* set an upper limit of 4 meV on the resonance strength, thereby non-negligibly increasing the  $^{22}\text{Na}(p, \gamma)$  reaction rate. It is difficult to say whether or not the 209-keV resonance is a separate resonance or has mistakenly been separated from the 214-keV resonance, as the density of states in this energy region is quite

high. We investigate both possibilities in Sec. 5.2.

## Chapter 2

# THEORY

This chapter describes the theory behind various aspects of nuclear astrophysics. First, a brief description of stellar evolution is given, followed by a more detailed account of the type of stellar path relevant to this dissertation: the nova. The main motivation for this dissertation is to further understand the nucleosynthesis that occurs in these violent explosions by helping in the search for their signatures, certain cosmic gamma-ray emitters. Two very important quantities in nuclear astrophysics are the yield of an interaction between two particles, whether in the laboratory or in a stellar environment, and the rate of the interaction. Both will be described in detail later in this chapter for narrow resonant reactions.

### **2.1 Stellar Evolution**

The beginning stages of stellar life originate from the gravitational coalescing of gas and dust particles, which gradually converts gravitational energy into thermal energy, heating the protostar. Depending on the mass of the initially formed object, different paths are available for evolution. Figs. 2.1 and 2.2 illustrate a snapshot into the lives of stars (Hertzsprung-Russell diagrams), and Fig. 2.3 shows several sample life cycles of stars with varying masses. The Hertzsprung-Russell diagrams of Figs. 2.1 and 2.2 plot increasing luminosity,  $L$ , as a function of decreasing surface temperature,  $T_s$ , or increasing color index, or spectra class. In a simplistic model of a star radiating as a black body, luminosity, star radius  $R$ , and temperature are related by:

$$L = 4\pi R^2 \sigma T_s^4, \quad (2.1)$$

where  $\sigma$  is the Stefan-Boltzmann constant. Depending on their temperature and where they are in their life cycle, these stars can synthesize different nuclei, a partial chart of which is shown in Fig. 2.4.

Nuclear reactions provide the energy source in stars and temporarily halt gravitational contraction, maintaining a balanced equilibrium until the element fueling the reactions is depleted. Once

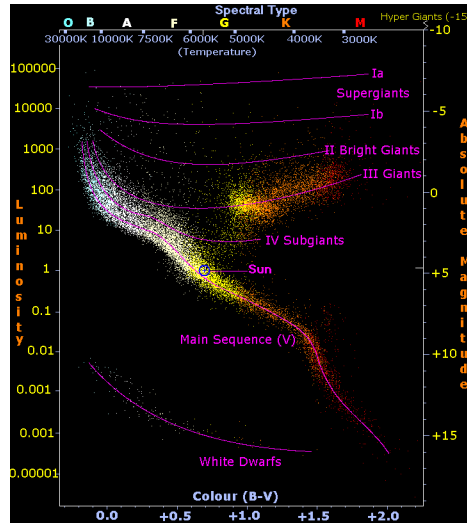


Figure 2.1: Detailed Hertzsprung-Russell diagram [28]. Luminosity is relative to the sun. Temperature, color index, and spectral type are all shown on the x-axis. Position of the sun is indicated slightly left of center.

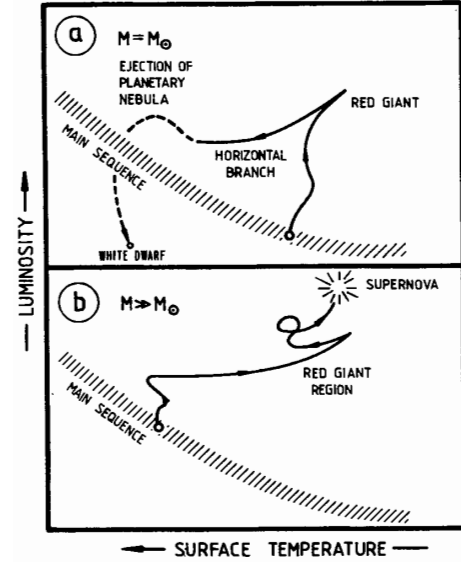


Figure 2.2: Qualitative Hertzsprung-Russell diagram, comparing two sample lifecycles of a sun-like star and a much more massive star. Reproduced from [27].

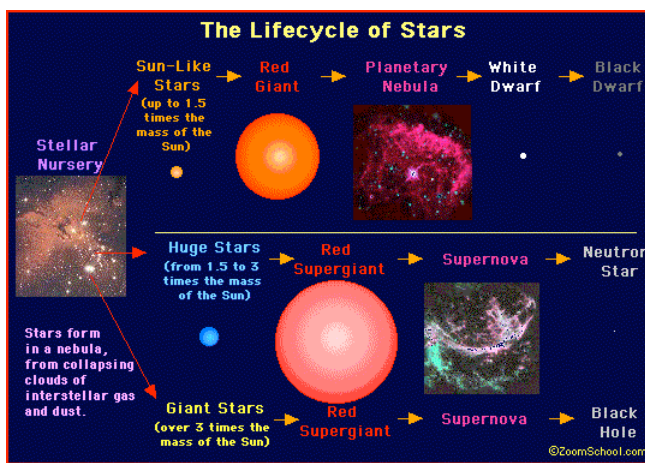


Figure 2.3: Three sample lifecycles of stars [29].

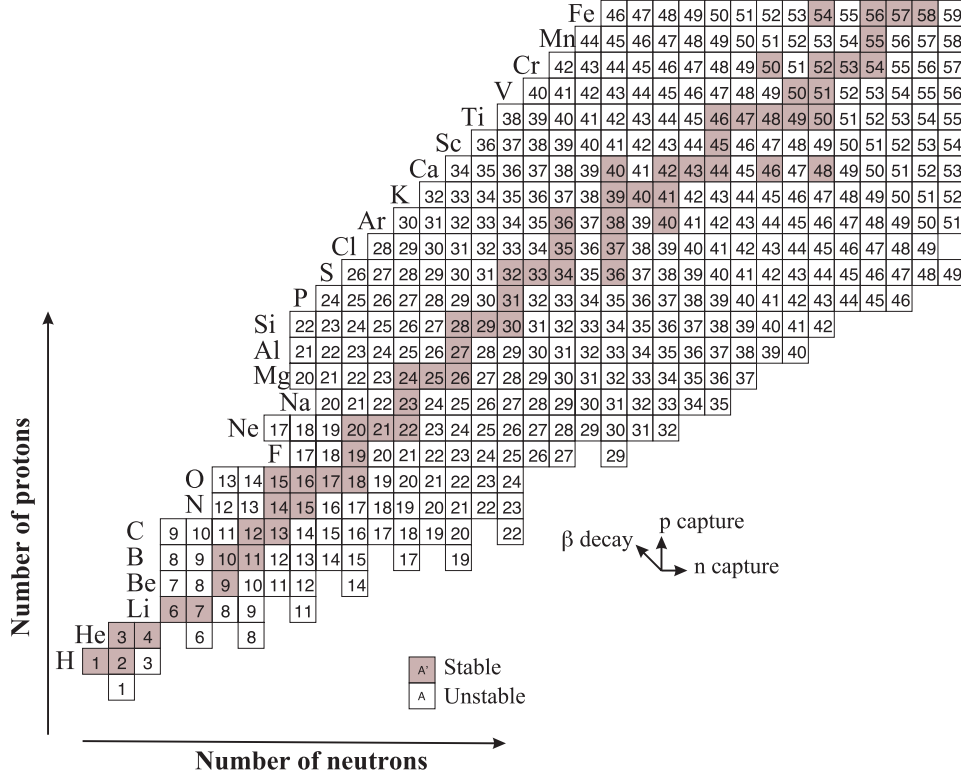


Figure 2.4: Partial chart of nuclides. Reproduced and expanded from Ref. [30].

formed, most stars start out on the main sequence sector, burning hydrogen into helium which provides the pressure to combat collapse due to gravity. The simplest energy generation cycle is this p-p chain, taking 4 protons and, through a series of nuclear reactions, ending with  ${}^4\text{He}$ , two positrons, two electron neutrinos, and 27 MeV of liberated energy. Quantum mechanical tunneling is essential to most processes occurring in stars, as the kinetic energy of the initial nuclei is below the Coulomb barrier.

If the temperature is high enough ( $\sim 1.7 \times 10^7$  K) and some remnant carbon is already present, these stars can ignite the CNO cycle as a path to produce helium [31]. When the hydrogen fuel has been depleted, helium burning then commences. The triple-alpha process, which forms  ${}^{12}\text{C}$  from  ${}^4\text{He}$ , circumvents elements in between these cycles (lithium, beryllium, and boron) from being formed with any high probability. As lithium, beryllium, and boron are highly reactive, upon formation during the p-p cycle, they are almost immediately destroyed. However, their measured solar

system abundance is much higher than is estimated from stellar nucleosynthesis owing to production in the interstellar medium via interactions of protons with very energetic cosmic rays; the density in free space is drastically lower than in stars, therefore their ability to react with other neighboring nuclei is greatly reduced.

Depending on the mass, stars can survive on the main sequence path for tens of millions to tens of billions of years, until the initial hydrogen fuel in the core has been consumed. A degenerate helium core surrounded by a hydrogen burning shell then remains. When the core ignites, the outer layers are heated, can expand immensely, and the surface reddens as the temperature drops due to the large increase in surface area. This is the red giant phase shown in Figs. 2.2 and 2.3.

Most stars have masses comparable to the sun and will then continue into the next phase, planetary nebula, where the outer layers of the star are shed and released into the interstellar medium. What remains is a white dwarf (Fig. 2.2 (a)), which can then become a black dwarf. A much different end to the life cycle can occur, however, if the white dwarf is in a binary system, described in the following section. If the star is massive enough, instead of following the path of a white dwarf, a supernova might take place (Fig. 2.2 (b)) in which the star explosively ejects most of its nuclei, leaving either a neutron star or black hole. Fig. 2.5 illustrates the interplay of gravitational contraction and fresh fuel ignition for such a massive star, leading to a supernova explosion.

## 2.2 Stellar Death and Nucleosynthesis

The most interesting phenomena for nuclear astrophysicists manifests in systems that occur at the end of stellar life cycles, such as novae, supernovae, or X-ray and gamma-ray bursts, where deviations from the quiescent hydrogen burning of main-sequence stars is staggering. Novae and supernovae are cataclysmic variable systems, wherein a significant fraction of their mass is ejected into the interstellar medium during their violent explosions and their increase in energy output is dramatic. Specifically, a classical nova is a thermonuclear outburst on the surface of a white dwarf star that is accreting hydrogen-rich material from its binary companion. Type Ia supernovae originate from a similar system, although the underlying white dwarf is entirely destroyed, as mentioned in the previous section, unlike in novae. Other types of supernovae include core-collapse supernovae, which require no binary companion to trigger the explosion.

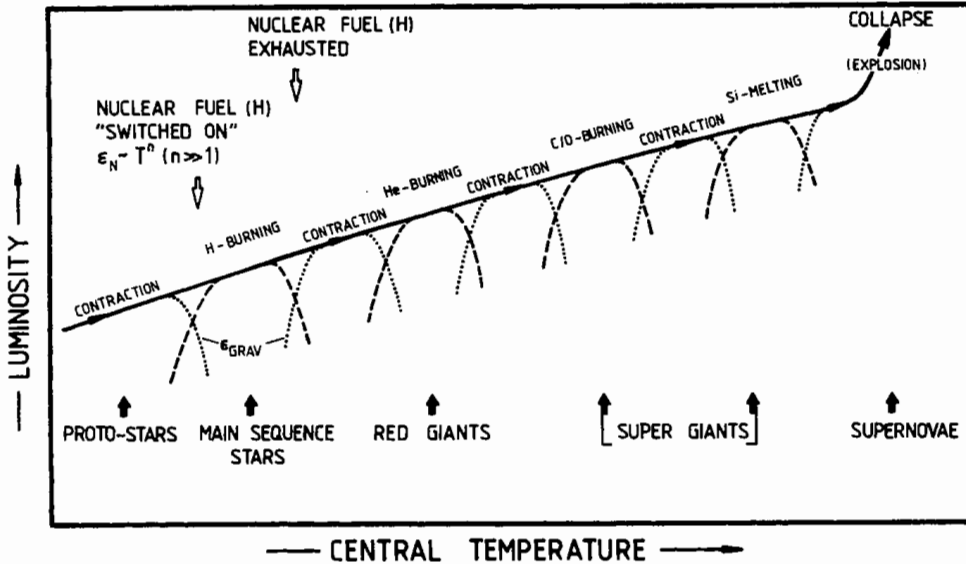


Figure 2.5: Sample burning cycle for a massive star leading to a supernova explosion. Reproduced from [27].

Because these cataclysmic variable systems have such a dramatic increase in temperature, they have the ability to synthesize nuclei much heavier than is produced in main-sequence stars. Proton fusion allows up nuclei up to Fe to be produced; however, above the Fe peak the Q value for fusion is no longer positive, as it has the largest binding energy per nucleon. Therefore, neutron capture reactions, which also are unaffected by the large Coulomb barrier, dominate above the Fe peak with the s-process and r-process which help to complete the chart of nuclides by successive neutron captures and beta decays, albeit on different time scales and paths. Because peak nova temperatures are several orders of magnitude less than peak supernova temperatures, only nuclides up to  $^{40}\text{Ca}$  can be produced [6]. Although novae are expected to account for only 0.03% of the mass of the gas and dust in the Galactic disk, they are thought to contribute significantly to the overproduction of specific nuclei above the solar abundances, such as  $^7\text{Li}$ ,  $^{13}\text{C}$ ,  $^{15}\text{N}$ ,  $^{17}\text{O}$ ,  $^{22}\text{Na}$ , and  $^{26}\text{Al}$  [3]. This is shown in Fig. 2.6 for various models. Both the models and the specifics of nova nucleosynthesis will be discussed in Sec. 2.3. If the potential ejecta are radioactive gamma-emitters, they have the ability to be detected by orbiting gamma-ray telescopes. INTEGRAL, the International Gamma-Ray Astrophysics Laboratory, is currently searching for these characteristic gamma-ray lines. It was deployed

by the European Space Agency in 2002 and currently has funding through 2012. SPI is a gamma-ray spectrometer consisting of 19 cooled, masked Ge detectors with massive anticoincidence shielding of BGO detectors [32]. Its range is 20 keV to 10 MeV and, along with its detection of  $^{26}\text{Al}$ , it has also detected  $^{44}\text{Ti}$  and  $^{60}\text{Fe}$ . It has not yet observed the characteristic line from  $^{22}\text{Na}$ . Examples of these cosmic gamma-ray emitters from various astronomical sources are listed in Table 2.1.

Table 2.1: Table of cosmic gamma-ray emitters, reproduced from Ref. [33]. Isotopes above the horizontal line are from individual objects or events. Those below the line are cumulative from many events. Elements with  $A > 40$  cannot be produced by novae.

Isotope	Mean lifetime	Decay chain	$E_\gamma$ (keV)
$^7\text{Be}$	77 d	$^7\text{Be} \rightarrow ^7\text{Li}^*$	478
$^{56}\text{Ni}$	111 d	$^{56}\text{Ni} \rightarrow ^{56}\text{Co}^* \rightarrow ^{56}\text{Fe}^* + e^+$	158, 812; 847, 1238
$^{57}\text{Ni}$	51 d	$^{57}\text{Co} \rightarrow ^{57}\text{Fe}^*$	122
$^{22}\text{Na}$	3.8 y	$^{22}\text{Na} \rightarrow ^{22}\text{Ne}^* + e^+$	1275
$^{44}\text{Ti}$	85 y	$^{44}\text{Ti} \rightarrow ^{44}\text{Sc}^* \rightarrow ^{44}\text{Ca}^* + e^+$	78, 68; 1157
$^{26}\text{Al}$	$1.04 \times 10^6$ y	$^{26}\text{Al} \rightarrow ^{26}\text{Mg}^* + e^+$	1809
$^{60}\text{Fe}$	$3.8 \times 10^6$ y	$^{60}\text{Fe} \rightarrow ^{60}\text{Co}^* \rightarrow ^{60}\text{Ni}^*$	59, 1173, 1332

Along with enriching the chemicals in the interstellar medium, nova may also be responsible for anomalous ratios discovered in pre-solar grains [34]. The outer nova shells in which most of the ejected material originates are much cooler and have much lower densities than the shells near the white dwarf core, thereby allowing dust particles to condense before leaving the system. One of the first anomalous ratios to be discovered was in the Orgueil meteorite [35], in which  $^{22}\text{Ne}/^{20}\text{Ne} \geq 0.67$ , as compared to a value equal to 0.1 on Earth. Because  $^{22}\text{Na}$  beta decays to  $^{22}\text{Ne}$ , this enrichment is likely due to an overabundance of  $^{22}\text{Na}$ . Recently, additional SiC and graphite grains have been identified to have enrichments that could be attributed to nova: low ratios for  $^{12}\text{C}/^{13}\text{C}$ ,  $^{14}\text{N}/^{15}\text{N}$ ,  $^{29}\text{Si}/^{28}\text{Si}$ ,  $^{27}\text{Al}/^{26}\text{Al}$ , and again for  $^{20}\text{Ne}/^{22}\text{Ne}$  [34, 36]. Excesses were also measured for  $^{30}\text{Si}$ . These ratios greatly help to constrain nova models [6].

As mentioned in Chapter 1, novae are ideal sites to probe explosive nucleosynthesis and mech-

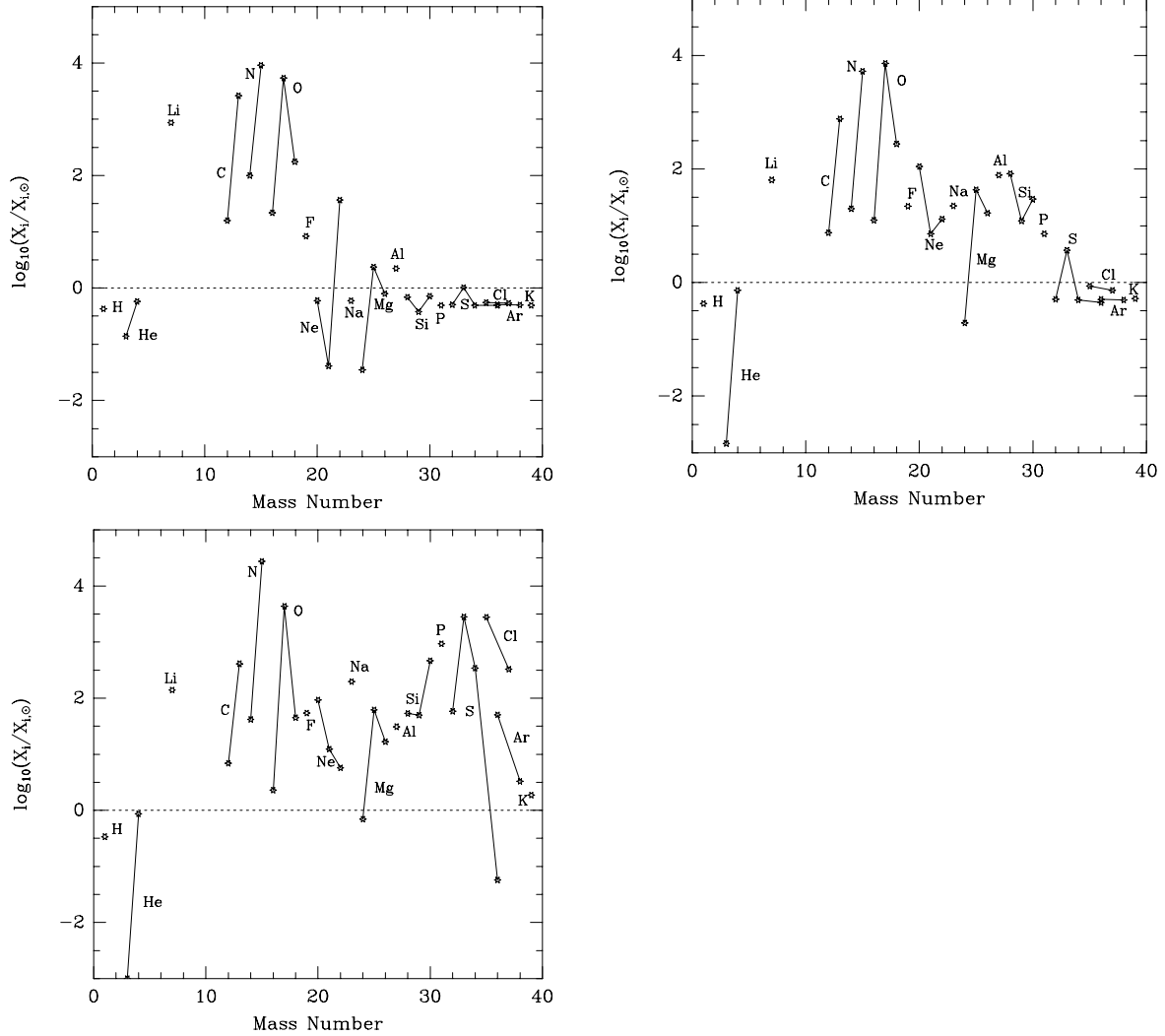


Figure 2.6: Overproduction factors relative to solar abundance as a function of mass number for various nova models, each with 50% mixing of the core material and the outer envelopes. Top left panel:  $1.15 M_\odot$  CO white dwarf. Top right panel:  $1.15 M_\odot$  ONe white dwarf. Bottom panel:  $1.35 M_\odot$  ONe white dwarf. Reproduced from Ref. [3].

anisms to trigger thermonuclear runaway. Whereas the modeling of supernovae requires several thousand nuclear reactions, novae can be fully simulated with only a few hundred. At this level, it is possible for most of the input reaction rates to be based on experimental information [6], which yields the advantage for novae to be more grounded in reality than the modeling of supernovae, where many theoretical suppositions are needed. In addition, the types of reactions available to novae typically only include proton captures (due to their lower Coulomb barrier, as compared to alpha or heavy-ion captures) and beta decays, the lifetimes of which are generally quite well known. This fairly simple nucleosynthetic system and the availability of experimentally determined reaction rates indicates that there is a much higher probability of being able to understand novae through various models.

As for the models themselves, a variety currently exist in an attempt to explain nova nucleosynthesis [6]. Most break up the nucleosynthesis into shells or zones. The most simple version includes parametrized one-zone models, wherein the modeling occurs in a single point of fluctuating temperature and density. These models may or may not also use the temperature and density outputs from hydrodynamic models, to be discussed below. This is a gross oversimplification but does allow one to predict the *relative* abundance changes when uncertainties of a large variety of reactions are varied on a short time scale. At the other end of the spectrum are full hydrodynamic models that simulate many zones and include convective mixing from the white dwarf core to the outer envelope. These models are also coupled to large reaction networks. At this time, mostly radially dependent models are employed, but 2D and 3D models are also being explored, although the necessary computing time precludes simulating a large range of white dwarf compositions and masses [6]. The 1D hydrodynamic models reproduce nucleosynthesis fairly well; however, the mixing between the core and outer envelopes is not well understood. More details on various models are discussed in Sec 7.2.

One question that has been addressed through modeling is the composition of the underlying white dwarf. The overproduction of nuclei up to  $A = 40$  for white dwarf cores composed of CO and ONe was shown in Fig. 2.6. For a CO core (left panel), the overproduced ejecta remain roughly below oxygen, due to lower peak temperatures and absence of ‘seed’ NeNa-MgAl nuclei. In order to boost the abundance much beyond oxygen, a more massive ONe core is needed (middle and right panels). Therefore, if elements in this higher mass region are observed, the composition of the white

dwarf core will be disclosed. It is this type which allows the synthesis of  $^{22}\text{Na}$  nuclei.

Although the most common explosive events are X-ray bursts (which eject negligible amounts of matter due to the extremely high escape velocities around their progenitor neutron star), classical novae are the second most common with 15 to 60 events/yr in our Galaxy [6]. Supernovae are much more rare, with roughly two a century in a typical galaxy [30]. Novae increase in brightness by factors of  $10^4 - 10^6$  (supernovae can reach up to factors of  $10^{10}$ ) and radiate energy with luminosity rates of  $10^{37} - 10^{38}$  ergs/s. Roughly 10,000 years are necessary to trigger an explosion with an accretion rate of  $\sim 10^{-10} - 10^{-9} M_{\odot}/\text{yr}$ , and approximately  $10^{-5} - 10^{-4} M_{\odot}$  of mass is ejected [6], with velocities ranging from 300 to 3000 km/s [27]. The time scale for the increase in light output can vary from a few days to up to 250 days; however, the peak temperatures of  $(1 - 4) \times 10^8$  K are reached only for several hundred seconds [6]. Unlike supernovae, novae can be recurrent, as only outer layers are ejected and the star is not entirely destroyed by the explosion. Although 15 to 60 novae are thought to occur per year, only 3 to 5 are detected [6], usually by nonprofessional astronomers who notice the large change in optical light output. Fig. 2.7 shows an actual nova explosion as viewed with the Hubble Space Telescope three years after detonation.

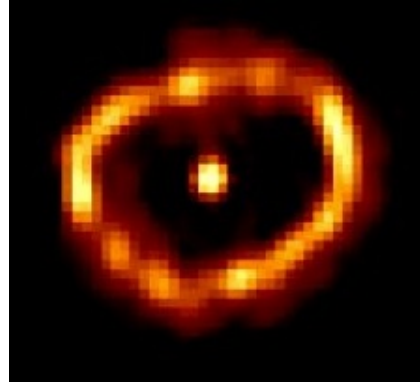


Figure 2.7: Nova Cygni 1992 with Hubble Space Telescope, photographed three years after eruption on December 27, 1995. The ring represents the ejected material moving away from the white dwarf star.

### 2.3 Nova Nucleosynthesis

A schematic of a nova is shown in Fig. 2.8. In this system, there is an asymmetric figure eight (a dashed line in the figure) called a Roche surface, which defines a gravitational equipotential: matter along this surface has an equal probability to fall to either star. During the course of its life cycle, the main sequence companion star will expand into its red giant phase. Once the matter broaches the Roche surface, it will begin to transfer through the inner Lagrange point (the point between the stars where net force of gravity equals the centripetal force) and accrete on the surface of the white dwarf star.

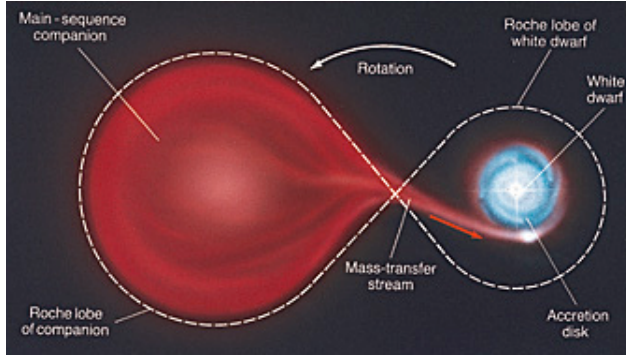


Figure 2.8: Scheme of nova explosion [37].

Due to the high density and small radius of the white dwarf (compared to its companion), the gravitational field is very strong at the surface, thereby imparting an extremely high velocity to the accreted gas. A classical star would simply expand to counteract this increase in temperature; however, white dwarfs are degenerate quantum objects. Because their densities are so high (on the order of  $\sim 10^5 - 10^6$  g/cc, versus the sun which has  $\sim 1$  g/cc), the spacing between atoms is around 0.01 Å, and the nuclei are completely ionized with the electrons forming a Fermi gas [38]. Due to Fermi-Dirac statistics, two fermions cannot occupy the same quantum state. In a degenerate electron gas at 0 K, this means that the electrons start to fill the energy levels from the ground state and are forced to move upward in energy. This filling occurs until all energy levels are completely filled up to the Fermi energy,  $E_F$ . All levels above this energy are perfectly vacant. This incompressibility provides the pressure to resist additional gravitational contraction. As the temperature increases from abso-

lute zero, the sharp step function describing the occupancy as a function of energy becomes slightly curved around  $E_F$ . However, even at peak nova temperatures around  $(1 - 4) \times 10^8$  K, this is much less than the corresponding Fermi temperature  $E_F/k_B$  of  $\sim 3 \times 10^9$  K [38]. Because the star cannot expand, the surface of the white dwarf is heated by the accreted gas. Once the temperature is high enough ( $\sim 20 \times 10^6$  K), nuclear reactions are ignited, and thermonuclear runaway ensues producing elements much higher up the chart of nuclides, ending with  $^{40}\text{Ca}$  (Fig. 2.4) [6]. Although novae are not hot enough to produce elements up to the iron peak, they are an essential system to understand before venturing into the more complicated explosive nucleosynthesis of supernovae.

To determine at what point the thermonuclear runaway is triggered, one can define an accretion timescale,  $\tau_{\text{acc}} \sim M_{\text{acc}}/\dot{M}$ , where  $M_{\text{acc}}$  is the accreted mass and  $\dot{M}$  is the accretion rate [6].  $\tau_{\text{acc}}$  is typically  $\sim 10^4 - 10^5$  yr. This can be compared to the nuclear timescale,  $\tau_{\text{nuc}}$ , given by  $C_p T/\epsilon_{\text{nuc}}$ , where  $C_p$  is the specific heat, and  $\epsilon_{\text{nuc}}$  is the nuclear energy generation rate. Accretion will continue quiescently while  $\tau_{\text{acc}} \leq \tau_{\text{nuc}}$ . However, at peak nova temperatures ( $\sim 10^8$  K), the thermonuclear reaction rates increase dramatically, and  $\tau_{\text{nuc}}$  can be on the order of seconds. When the threshold between the two phases has passed, the thermonuclear runaway ensues. As previously mentioned, the most important nuclear reactions in nova explosions are beta decays (timescale  $\tau_{\beta^+}$ ) and proton captures (timescale  $\tau_{(p,\gamma)}$ ). When ramping up to the runaway, nuclear reactions that occur will be from the equilibrium CNO cycle, with  $\tau_{\beta^+} < \tau_{(p,\gamma)}$ . Once  $^{12}\text{C}$  is produced by the triple alpha process, the CNO cycle is used during nova outbursts to produce  $^{13}\text{C}$ ,  $^{15}\text{N}$ , and  $^{17}\text{O}$ . The various processes are shown in Fig. 2.9.

These are the main processes for nova nucleosynthesis in lower mass CO white dwarfs.  $^{15}\text{N}$  and  $^{17}\text{O}$  are overproduced with respect to solar abundances by factors of  $\sim 1000$  [6]. When the peak nova temperature is reached,  $\tau_{\beta^+} \gtrsim \tau_{(p,\gamma)}$ , and proton captures proceed much more quickly, circumventing beta decay, and further movement up the chart of nuclides (Fig. 2.4) is possible. Convection also plays a critical role in carrying some fraction of nuclei to the outer envelopes before allowing them to beta decay. The energy received by the cooler envelope from the decays raises the temperature which removes the degeneracy. Then the envelope is allowed to expand as a normal gas, triggering the ejection process. Convection also works in the opposite way, by supplying unburned fuel to the inner core. It is the degree of mixing of the core with the envelopes that is the least understood in nova modeling.

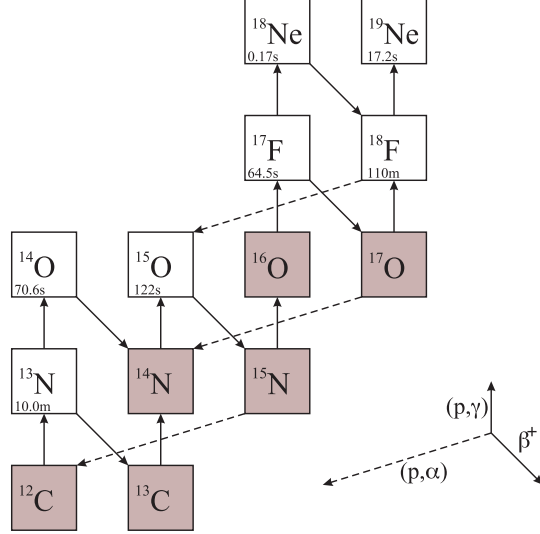


Figure 2.9: Nova nucleosynthesis in the mass region of CNO. Shaded nuclei are stable. For decays, the lifetime is given. Information and style from Ref. [6].

The cosmic gamma-ray emitters synthesized in these types of white dwarfs include  $^{13}\text{N}$ ,  $^{18}\text{F}$ , and  $^{7}\text{Be}$ .  $^{13}\text{N}$  and  $^{18}\text{F}$  each produce a very strong emission line at 511 keV (and a continuum below) from the annihilation of the positron from their beta decays with neighboring electrons. It was previously thought that  $^{14,15}\text{O}$  and  $^{17}\text{F}$  also contributed [39], but it turns out this is not the case, as these nuclei decay before the gamma rays can escape. Unfortunately, because the prompt emission occurs only for several hours after the explosion, observational identification of the progenitor star is unlikely.  $^{7}\text{Be}$  is associated with a 478-keV line, but like the aforementioned nuclei, it most likely will decay away ( $\tau = 77$  d) before detection.

To move further up the chart and to synthesize nuclei higher than  $^{19}\text{F}$ , a ONe white dwarf composition is needed, where the core is thought to mainly be composed of  $^{16}\text{O}$  and  $^{20}\text{Ne}$  [7] providing the seed nuclei for the next nucleosynthetic cycle: the NeNa–MgAl cycle. Two of the most interesting cosmic gamma-ray emitters are  $^{26}\text{Al}$  and  $^{22}\text{Na}$ . Indeed,  $^{26}\text{Al}$  has been observed in the Galaxy [40], yielding proof of active nucleosynthesis, but its long half life precludes the identification of its progenitor, and novae are only expected to make a secondary contribution to its Galactic abundance [7, 41]. Other gamma-ray emitters can provide more direct constraints on nova models [39]. An example is  $^{22}\text{Na}$  ( $t_{1/2} = 2.603$  years,  $E_\gamma = 1.275$  MeV), which has not yet been observed in the

Galaxy. Unlike  $^{26}\text{Al}$ , the relatively short half life of  $^{22}\text{Na}$  restricts it to be localized near its production site. Novae also could be the principal Galactic sites for the production of  $^{22}\text{Na}$ , making  $^{22}\text{Na}$  an excellent nova tracer. An observational upper limit of  $3.7 \times 10^{-8} M_{\odot}$  was set on the  $^{22}\text{Na}$  mass in ONe nova ejecta with the COMPTEL telescope onboard the CGRO [42]. Currently, the maximum  $^{22}\text{Na}$  mass ejected using ONe nova models is an order of magnitude below this limit [7, 43] and corresponds to a maximum detection distance of 500 parsecs using an observation time of  $10^6$  s with the spectrometer SPI onboard the currently-deployed INTEGRAL mission [44]. This suggests we are now on the verge of being able to detect this signal. In addition, there could also be a contribution from Type II supernovae where  $^{22}\text{Na}$  is thought to be produced by neutrino spallation of  $^{23}\text{Na}$  in the Ne shell [45].

A sketch of the path of the nucleosynthesis cycle to produce and destroy  $^{22}\text{Na}$  is shown in Fig. 2.10.

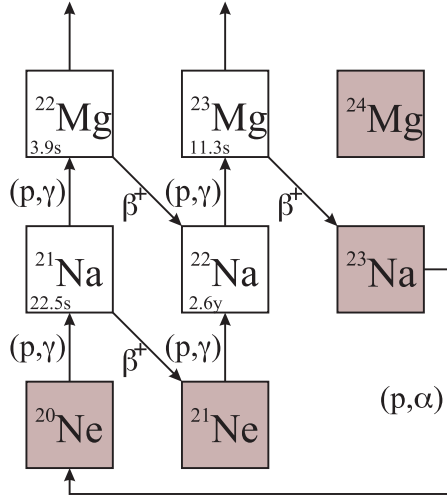
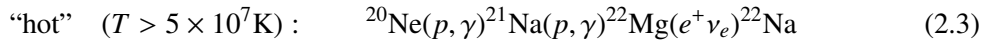
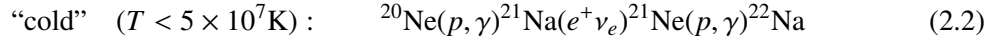


Figure 2.10: NeNa reaction cycle. Shaded nuclei are stable. For decays, the lifetime is given. Information and style from Ref. [43].

The cycle begins with the seed nucleus, stable  $^{20}\text{Ne}$ , possibly donated from the white dwarf core. Production can proceed in two ways: “cold” or “hot”, depending on the stellar temperature:



Each cycle first captures a proton to produce  $^{21}\text{Na}$ . In the “cold” cycle,  $^{21}\text{Na}$  then beta decays to  $^{21}\text{Ne}$  before capturing a proton to produce  $^{22}\text{Na}$ . If the temperature in the burning shell is above  $5 \times 10^7$  K [7], the hot cycle continues from  $^{21}\text{Na}$  to  $^{22}\text{Mg}$  with another proton capture, before allowing time for the  $^{21}\text{Na}$  nucleus to beta decay.  $^{22}\text{Mg}$  then beta decays to  $^{22}\text{Na}$ . This dissertation, however, focuses on the main destructive reaction for  $^{22}\text{Na}$ : the proton capture to the  $^{23}\text{Mg}$  nucleus. An energy level diagram for this nucleus is shown in Fig. 2.11.

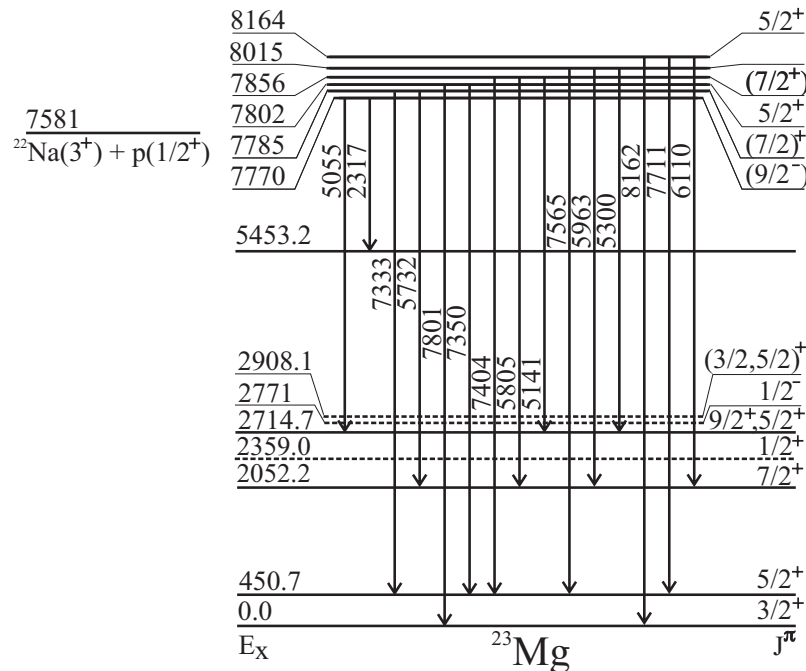


Figure 2.11: The relevant part of the decay scheme of  $^{23}\text{Mg}$ . Energies are in keV. Not all  $^{23}\text{Mg}$  levels are shown.

When a proton with an energy corresponding to a level in the  $^{23}\text{Mg}$  nucleus encounters a  $^{22}\text{Na}$  nucleus, the cross section for the reaction increases drastically, and a resonance is formed. Shown are resonances for laboratory proton energies of 198 to 610 keV, which are far below the Coulomb barrier of  $\sim 5$  MeV. Therefore, tunneling is required to form these states, hence their strengths are weak and on the order of meV.

### 2.3.1 White Dwarf Mechanics

It is instructive to investigate the relation between the white dwarf density,  $\rho(r)$ , and the mass (independent of radius) and to explore the difference for non-relativistical and relativistic electrons. One starts with the simple hydrostatic equilibrium of a non-relativistic star, where the change in pressure as a function of radius is balanced by gravity [46, 47]:

$$\frac{dP(r)}{dr} = -\rho(r) \frac{GM(r)}{r^2}, \quad (2.4)$$

where  $P(r)$  is the pressure inside the star,  $r$  is the radius,  $M(r)$  is the mass up to radius  $r$ , and  $G$  is the gravitational constant. Assuming the gross approximation that the density is equal to  $M/R^3$ , Eq. 2.4 integrates to,

$$P \sim \frac{GM^2}{R^4}. \quad (2.5)$$

This central pressure is supplied by the degenerate electrons (with mass  $m$ ). If one considers a non-relativistic particle in a 1D box with a side length  $R$  and volume  $V$  (equal to  $R^3$ ), then the wave function that solves the time-independent Schrödinger equation,  $\nabla_x^2\Psi = -k^2\Psi$ , is  $\Psi = A \sin(kx) + B \cos(kx)$ , where  $k = 2mE/\hbar^2$ , and  $A, B$  are constants. Applying the boundary condition that the wave function must vanish at the edges of the box results in  $B = 0$  and  $kR = n\pi$ , for integers  $n = 0, 1, 2, \dots$ . Rearranging the relation for  $k$  and substituting this boundary condition yields a quantized energy  $E = \hbar^2 n^2 \pi^2 / (2mR^2)$ . Expanding this idea to three dimensions, the system would then be characterized by three quantum numbers,  $n_x, n_y, n_z$ . In a 3D coordinate system comprised of these quantum numbers, one can define a radius that characterizes the density of the electrons,  $n_F^2 = n_x^2 + n_y^2 + n_z^2$  [38], and the Fermi energy is then equal to

$$E_F = \frac{\hbar^2}{2m} \left( \frac{\pi n_F}{R} \right)^2 = \frac{\hbar^2}{2m} \left( \frac{3\pi^2 N}{V} \right)^{2/3}, \quad (2.6)$$

where  $n_F$  has been redefined in terms of  $N$ , equivalent to the total number of available states and to the total number of electrons, as this is a Fermi gas. In the coordinate system of  $n_x, n_y, n_z$ , the volume encompassed in a sphere of radius  $n_F$  is equal to the total number of quantum states in the quadrant where all  $n_i$  are positive (including a factor of 2 for the possible spin states):  $N = 2 \times \frac{1}{8} \times 4\pi n_F^3 / 3$ . This relation has been used to eliminate  $n_F$  in Eq. 2.6. The total energy is equal to the individual Fermi energy integrated over all possible states multiplied by a factor of 2 to account for spin states

and is equal to  $E = 3NE_F/5$ . The pressure is then the derivative of the total energy with respect to volume:

$$P = -\left(\frac{dE}{dV}\right)_S = \frac{3}{5}N\frac{\hbar^2}{2m}\frac{2(3\pi^2N)^{2/3}}{V^{5/3}} = \frac{\hbar^2}{5m}(3\pi^2)^{2/3}\left(\frac{N}{V}\right)^{5/3} \propto (M/R^3)^{5/3} \propto \rho^{5/3}, \quad (2.7)$$

where  $N = M/m$  was used, and constants such as  $m$  have been ignored for the proportionality.

Equating the pressures from Eqs. 2.5 and 2.7, one extracts,

$$R \propto 1/M^{1/3}. \quad (2.8)$$

Using this relation to eliminate the radial dependence from  $M/R^3$ , one obtains,

$$\rho \propto M^2, \quad (2.9)$$

for the central density. This only holds for non-relativistic electrons where  $E_F = p^2/(2m)$ . In the ultra relativistic limit, this relation becomes  $E_F = pFc$ , and the pressure is then proportional to  $\rho^{4/3}$ , and not  $\rho^{5/3}$ , as was shown above for non-relativistic electrons. Equating the hydrostatic pressure from Eq. 2.5 to this function of density yields

$$\frac{GM^2}{R^4} \propto \left(\frac{M}{R^3}\right)^{4/3}, \quad (2.10)$$

where the dependence on radius cancels out. Therefore, as mass increases, the density is no longer constrained. A more careful analysis derives from this a mass limit [47], denoted  $M_{\text{Ch}}$  such that,

$$M_{\text{Ch}} = 1.43M_{\odot}. \quad (2.11)$$

As the velocity of the electrons approaches the speed of light, there exists a maximum mass for which a white dwarf is stable. Above this mass, the Chandrasekhar mass, electron pressure can no longer support the star's collapse [47]. Fig. 2.12 shows a rough estimate of the radius of the white dwarf as a function of mass, illustrating this limit.

## 2.4 Nuclear Reactions

In order to discuss the details of a rate for a typical nuclear reaction, one must first introduce the concept of a cross section,  $\sigma$ , which gives the probability that a specific reaction will occur [30]. For

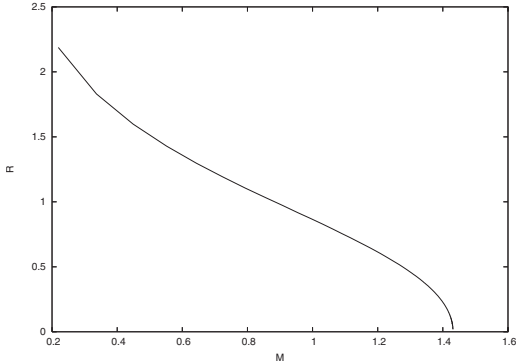


Figure 2.12: White dwarf radius as a function of mass for a simplified calculation with relativistic electrons [47]. The radius is in units of  $R_{\oplus}$ , and the mass is in units of  $M_{\odot}$ .

a simple nuclear reaction, if one were to assume a number of beam particles,  $N_b$ , spread out over an area,  $A$ , are incident on a target with  $N_T$  number of nuclei inside the area,  $A$ , then the number of interactions or reactions,  $N_R$ , would be directly proportional to  $\sigma$ , such that:

$$N_R = \sigma \frac{N_b N_T}{A}. \quad (2.12)$$

An increase in either the number of beam particles or target nuclei will increase the number of reactions. The areal density also plays a role because if the colliding particles are too far apart, this will decrease the number of reactions. This is a simple version of what was discussed in Sec. 1.2.1.

#### 2.4.1 Structure of the Nucleus and Selection Rules

The energy levels of interest to this dissertation for the  $^{23}\text{Mg}$  nucleus are shown in Fig. 2.11. Models such as the liquid drop and Fermi gas model qualitatively describe overall nuclear properties but do not capture the features of the excited states. The shell model more realistically quantifies the existence of nuclear shells, analogous to the shells of atomic electrons. However, because of the complexity of combining 12 protons with 11 neutrons, all of which are interacting via the strong force, theoretical models have difficulty accurately describing the energy levels of interest to  $^{22}\text{Na}(p, \gamma)$  where the density of states is high, leaving knowledge to be driven by experiment.

Before any composite nuclear state can be formed in a standard reaction, it must follow the rules of angular momentum and parity conservation (although parity non-conservation has been observed

in select cases). Simply put, a final state,  $| JM \rangle$ , with total angular momentum,  $J$ , with projection,  $M$ , can be written as

$$| JM \rangle = \sum_{m_1, m_2} | j_1 j_2; m_1 m_2 \rangle \langle j_1 j_2; m_1 m_2 | JM \rangle, \quad (2.13)$$

where  $j_1$  and  $j_2$  are the total angular momenta of the initial two nuclei, each with projections,  $m_1$  and  $m_2$ , respectively [48]. For this relation to hold non-trivially, the Clebsch-Gordon coefficient,  $\langle j_1 j_2; m_1 m_2 | JM \rangle$ , must not be equal to zero. From the rules of addition of angular momentum, this means that  $J$  may span  $|j_1 - j_2| \leq J \leq j_1 + j_2$ , but  $M = m_1 + m_2$ , where  $|m_i| \leq j_i$ . It should be noted that total angular momentum is equal to  $l \odot s_1 \odot s_2$ , where  $l$  is orbital angular momentum of the interaction, and  $s_1$  and  $s_2$  are the spin of each nucleus. Although angular momentum is an additive property, parity is multiplicative: the final parity,  $\Pi$ , is equal to  $(-1)^l \pi_1 \pi_2$ , where  $\pi_1$  and  $\pi_2$  are the intrinsic parities of the initial nuclei.

As seen in Fig. 2.11, the spin/parity of  $^{22}\text{Na}$  and  $p$  are  $3^+$  and  $1/2^+$ , respectively. This means that the excited state in  $^{23}\text{Mg}$  can be  $5/2^+$  or  $7/2^+$  (s-wave,  $l = 0$ ),  $3/2^-$ ,  $5/2^-$ ,  $7/2^-$ , or  $9/2^-$  (p-wave,  $l = 1$ ), and  $1/2^+$  through  $11/2^+$  in steps of 1 (d-wave,  $l = 2$ ). Because probability of forming a state decreases with increasing  $l$ , the value of  $l$  is likely not higher than 1, although higher values cannot be completely ruled out. Fig. 2.11 shows the tentative assignments from Refs. [1, 49], estimating that some levels are most likely  $7/2^+$ , with two definite assignments of  $5/2^+$ . The potential  $9/2^-$  level corresponding to the 198-keV resonance can be reached with  $l = 1$ , although that spin/parity assignment is not firm [50].

Once the excited state in  $^{23}\text{Mg}$  has been formed, it then de-excites through the emission of a gamma ray. The electric and magnetic fields involved in this interaction can be expanded as a linear combination of fields whose coefficients are multipole moments with well-defined values for  $l$  and  $m$  [51]. Table 2.2 shows some properties of these multipole moments. Each gamma-ray transition can be through either an electric ( $El$ , parity =  $(-1)^l$ ) or magnetic ( $Ml$ , parity =  $(-1)^{l+1}$ ) channel, although the minimum value for  $l$  in a nuclear de-excitation is 1 because of the photon spin. Qualitatively, electric transitions generally have a higher probability to occur than magnetic ones for the same value of  $l$ , and the probability decreases by  $\sim 10^{-5}$  when  $l$  is increased by one unit. The probability for each is proportional to the gamma-ray energy to a power  $2l + 1$ , so de-excitation through a higher energy gamma ray is favorable. The general rule is a de-excitation will occur

Table 2.2: Table of multipole moments up to  $l = 2$  [31, 51].

Designation	$l$	$m$	Angular dependence
Monopole	0	0	isotropic
Dipole	1	0	$\sin^2 \theta$
		$\pm 1$	$1 + \cos^2 \theta$
Quadrupole	2	0	$\sin^2 \theta \cos^2 \theta$
		$\pm 1$	$1 - 3 \cos^2 \theta + 4 \cos^4 \theta$
		$\pm 2$	$1 - \cos^4 \theta$

through the channel with the lowest value of allowed  $l$  and will proceed through an  $E1$  transition if possible. These are the so-called *Weisskopf estimates* [31]. According to Ref. [52], the transition rates (in natural units),  $w_{E1}$  and  $w_{M1}$ , are equal to:

$$w_{E1} = \frac{4\pi}{137} k(kR)^{2l}; \quad w_{M1} = \frac{4\pi}{137} k(kR)^{2l+2}, \quad (2.14)$$

where  $R$  is the nuclear radius,  $k$  is the wave number, which is proportional to the energy, and  $kR \ll 1$ .

Although as illustrated above, some of the spins and parities of the initial excited states in  $^{23}\text{Mg}$  have a high degree of uncertainty, these quantities are well known for the first few excited states [49]. As an example for a transition where both initial and final spins and parities are known is the level at  $E_x = 8164$  keV with  $5/2^+$ , most likely formed by s-wave capture. This level de-excites through the emission of gamma rays to the ground, first, and second excited states, which are designated as  $3/2^+, 5/2^+$ , and  $7/2^+$ , respectively. The transition to the ground state is likely a mixed  $M1$  and  $E2$  transition because the total angular momentum changes by 1 unit but parity remains positive.  $M3$  and  $E4$  are also possible with a lower probability. The transition to the first excited state involve no change in spin or parity, indicating  $M1$  or  $E2$  as well. Higher multipoles are possible ( $M3, E4, M5$ ) but would be greatly suppressed. One unit of angular momentum is added for the transition to the second excited state, again with no change in parity. The same multipoles for the transition to the first excited state also apply here, with the addition of the possibility for  $E6$ . A similar methodology can be applied to the other de-excitations, although their spins and parities are less

well-known. For the potential resonance at 198 keV, according to Ref. [1], the strongest branch (58%) in the de-excitation has a final level with a spin/parity equal to either  $9/2^+$  or  $5/2^+$ . The transition from  $9/2^-$  to  $9/2^+$  would most likely be of the  $E1$  type (other possible transitions are  $M2, E3, M4, E5, M6, E7, M8, E9$ ), and the transition from  $9/2^-$  to  $5/2^+$  could proceed through the  $M2$  type (possible:  $E3, M4, E5, M6, E7$ ). The final level for the other branch in this de-excitation (42%) has a completely unknown spin and parity. However, because this branch is comparatively strong and its energy is almost *half* the value of the primary transition energy, it is most likely an  $E1$ . The final state could then be  $7/2^+, 9/2^+$  or  $11/2^+$ .

#### 2.4.2 Decays

Any decay can be characterized by the formula,  $dN/dt = -\lambda N$ , which integrates to yield  $N(t) = N(0)e^{-\lambda t}$ , where  $N$  is the number of atoms at a time  $t$ , and  $\lambda$  is the decay constant (also equal to  $1/\tau$ , the lifetime of the state) [53, 31]. Solving the time-dependent Schrödinger equation separately in space and time for a time-independent potential produces a wave function,  $\psi(t) = \psi(0)e^{-iEt/\hbar}$ . To ensure a decaying state, one can specify  $E = E_o - i\Gamma/2$ , which yields a probability  $|\psi(t)|^2 = |\psi(0)|^2 e^{-\Gamma t/\hbar}$  from the wave function,

$$\psi(t) = \psi(0)e^{-iE_o t/\hbar} e^{-\Gamma t/2\hbar}. \quad (2.15)$$

Consistency with the laws governing decay indicate that  $\Gamma$  must be equal to  $\lambda\hbar$  and is commonly called the full width of the state.  $E_o$  is simply the real part of the complex energy that solves the time-independent Schrödinger equation. Although squaring Eq. 2.15 (i.e.  $\psi\psi^*$ ) produces the probability of finding a state as a function of time, it is sometimes more convenient to have the probability as a function of energy,  $P(E)$ . This is accomplished simply by taking the Fourier transform of Eq. 2.15 and squaring it as well. This yields,

$$P(E) \propto \frac{\Gamma}{(E - E_o) + (\Gamma/2)^2}. \quad (2.16)$$

This is the basis for the Breit-Wigner formula for the energy dependence of narrow resonance cross sections and is applicable to any non-steady state.

### 2.4.3 $A(x, \gamma)B$ Reactions

Two types of reactions producing only a gamma ray in the final state, in addition to the product nucleus, will be discussed in this subsection: non-resonant (Fig. 2.13) and resonant (Fig. 2.14) reactions, the latter of which is the focus of this dissertation.  $A$  is the target nucleus,  $B$  is the final nucleus, and  $x$  is the projectile.

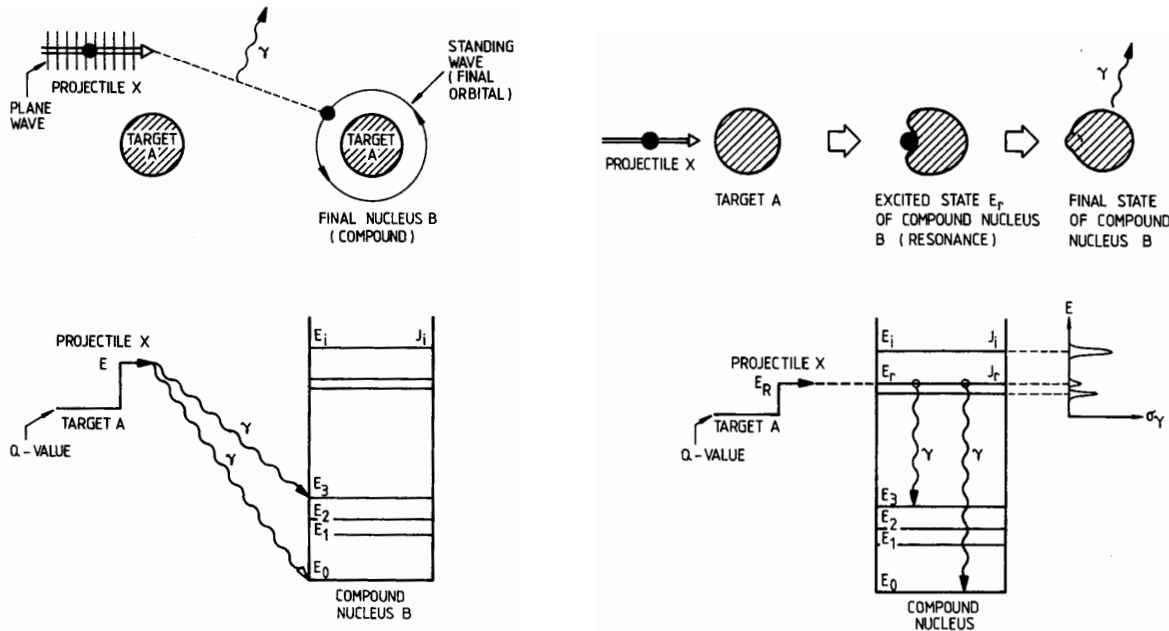


Figure 2.13: Direct capture reaction: physical sketch (top) and energy diagrams (bottom). Reproduced from Ref. [27].

Figure 2.14: Resonant reaction: physical sketch (top) and energy diagrams (bottom). Reproduced from Ref. [27].

### Non-resonant Reactions

Before discussing resonant reactions, it is instructive to understand an alternative: non-resonant direct capture. As illustrated in Ref. [27], direct capture is a one-step process characterized by a solitary matrix element:

$$\sigma_\gamma \propto |\langle B | H_\gamma | A + x \rangle|^2, \quad (2.17)$$

where  $H_\gamma$  is the Hamiltonian for an electromagnetic interaction. A sketch of this type of reaction is shown in Fig. 2.13

This reaction's projectile interacts with the target nucleus and *directly* enters the final state, after emitting a gamma ray with an energy corresponding to that particular level in the final nucleus. This can occur at *any* projectile energy; therefore, the energy dependence of the cross section has no significant, quickly-fluctuating features. Resonant reactions cross sections have nearly the opposite energy dependence.

### *Resonant Reactions*

Resonant reactions, in contrast to direct capture, occur in a two-step process where the projectile's energy,  $E_r$ , is within  $\Gamma$  of the energy of an excited state in the compound nucleus,  $E_x$  (minus the  $Q$  value for the reaction). The first step is the capture of the projectile in an excited state,  $E_i$ , of a so-called compound nucleus. Then the compound nucleus de-excites with the emission of a gamma ray to a final state of energy  $E_f$ . This reaction is described by [27]:

$$\sigma_\gamma \propto |\langle E_f | H_\gamma | E_i \rangle|^2 |\langle E_i | H_f | A + x \rangle|^2, \quad (2.18)$$

where  $H_f$  is the Hamiltonian for the formation of the compound nucleus. A sketch for this type of reaction is shown in Fig. 2.14. Because of the energy restriction  $E_r = E_x - Q$ , the cross section is essentially zero when the projectile's energy is far from the resonance energy and can be extremely high when  $E_p$  is within  $\Gamma$  of  $E_r$  (i.e. when the phase shift,  $\delta_l$ , passes through  $\pi/2$ , as will be seen below). Resonances are considered *narrow* when  $\Gamma/E_r \leq 10\%$  [27] and *isolated* from other resonances when  $\Gamma_i + \Gamma_{i+1} \lesssim E_{r_i} - E_{r_{i+1}}$ . The cross section for narrow, isolated resonances can then be visualized as a forest of separately resolved delta functions, with each tree representing a different resonance.

Next, one must determine the exact form of the cross section. Although the incoming particle (with momentum  $p = \hbar k$ ) can be approximated by a plane wave  $\Psi_i = e^{ikz}$ , it is more convenient to characterize the plane wave as a linear combination of spherical waves, called the partial wave expansion [31]:

$$\Psi_i = A \sum_{l=0}^{\infty} i^l (2l+1) j_l(kr) P_l(\cos \theta), \quad (2.19)$$

where  $j_l(kr)$  are spherical Bessel functions (radial solutions to the Schrödinger equation),  $P_l(\cos \theta)$  are Legendre polynomials, and  $A$  is a normalization constant. This deconvolution of a mathematical

concept such as a wave function or electromagnetic field into separate elements, each denoted by an angular momentum  $l$ , was also seen in Sec. 2.4.1. Because angular momentum is conserved,  $l$  is a good quantum number (for spinless particles). To better visualize this expansion as the sum of incoming and outgoing spherical waves, it is illustrative to see the explicit expression for  $l = 0$ :

$$\Psi = \frac{A}{2ik} \left( \frac{e^{ikr}}{r} - \frac{e^{-ikr}}{r} \right), \quad (2.20)$$

where  $e^{ikr}/r$  and  $e^{-ikr}/r$  are the incoming and outgoing spherical waves, respectively.

To estimate a maximum value for the cross section, in an approximation the angular momentum  $l\hbar$  will be equal to  $pb$ , where  $b$  is the impact parameter, representing the perpendicular distance from the projectile to the target. Reordering these quantities yields,

$$b = l \frac{\hbar}{p} = l\lambda. \quad (2.21)$$

$l$  is quantized, and  $\pi\lambda^2$  is the maximum effective area of interaction for  $l$  between 0 and 1. Thus, the area between subsequent “shells” of angular momentum is equal to  $\pi((l+1)\lambda)^2 - \pi(l\lambda)^2 = (2l+1)\pi\lambda^2$ .

The total maximum area, or cross section, would then be the sum of all shells:

$$\sigma = \sum_{l=0}^{l=R/\lambda} (2l+1)\pi\lambda^2, \quad (2.22)$$

where  $R$  is the sum of the radii of the projectile and target nucleus. This equation hints at what the overall magnitude of the cross section will be.

A more rigorous approach to calculate the actual value for the cross section manipulates the form of the wave function in Eq. 2.19 and then calculates the quantum mechanical current,  $j$ , defined as:

$$j = \frac{\hbar}{2im} \left( \Psi^* \frac{\partial \Psi}{\partial r} - \Psi \frac{\partial \Psi^*}{\partial r} \right). \quad (2.23)$$

The differential cross section,  $d\sigma/d\Omega$ , is then equal to:

$$\frac{d\sigma}{d\Omega} = \frac{r^2 j_{\text{scattered}}}{j_{\text{incident}}}. \quad (2.24)$$

Integrating over all angles produces the total cross section. Following this procedure, first for purely elastic scattering and then generalized for multiple reaction channels, the incident wave function can be rewritten by approximating the Bessel function by its form far away from the scattering center (i.e. the position of the detector). Eq. 2.19 then becomes:

$$\Psi_i = \frac{A}{2kr} \sum_{l=0}^{\infty} i^{l+1} (2l+1) \{ e^{-i(kr-l\pi/2)} - e^{i(kr-l\pi/2)} \} P_l(\cos \theta). \quad (2.25)$$

The structure of this equation can be compared to Eq. 2.20, which is a simple sum of incoming and outgoing spherical waves. Scattering can take the form of a phase shift or change in amplitude for the outgoing wave. This would modulate the second term in the curly brackets in Eq. 2.25 by a complex factor,  $\eta_l$  such that the wave function of the system is:

$$\Psi = \frac{A}{2kr} \sum_{l=0}^{\infty} i^{l+1} (2l+1) \{ e^{-i(kr-l\pi/2)} - \eta_l e^{i(kr-l\pi/2)} \} P_l(\cos \theta). \quad (2.26)$$

Because Eq. 2.26 is the sum of an incident spherical wave and a scattered outgoing spherical wave, subtracting Eq. 2.25 yields the scattered outgoing wave only,  $\Psi_s$ :

$$\Psi_s = \frac{Ae^{ikr}}{2kr} \sum_{l=0}^{\infty} i(2l+1)(1-\eta_l) P_l(\cos \theta). \quad (2.27)$$

Using the wave functions in Eqs. 2.25 and 2.27 to calculate the respective currents in Eq. 2.23 and then substituting those forms into Eq. 2.24 to calculate the differential cross section yields:

$$\frac{d\sigma}{d\Omega} = \frac{1}{4k^2} \left| \sum_{l=0}^{\infty} i(2l+1)(1-\eta_l) P_l(\cos \theta) \right|^2 \quad (2.28)$$

Integrating then results in a cross section equal to:

$$\sigma_s = \sum_{l=0}^{\infty} \pi \lambda^2 (2l+1) |1-\eta_l|^2, \quad (2.29)$$

where  $\lambda^2$  has been substituted for  $1/k^2$ . For purely elastic scattering  $|\eta_l| = 1$ , therefore, convention dictates redefining  $\eta_l = e^{2i\delta_l}$ , where  $\delta_l$  is the phase shift. Algebra then leads to:

$$\sigma_s = \sum_{l=0}^{\infty} 4\pi \lambda^2 (2l+1) \sin^2 \delta_l, \quad (2.30)$$

This cross section increases rapidly when  $\delta_l = \pi/2$ , and thus, is the quantitative definition of a resonance. For resonant capture, we assume only one partial wave,  $l$ , contributes. Therefore, a more relevant form of the cross section for purely elastic scattering through a resonance may be obtained by expanding  $\cot \delta_l$  in energy around this phase shift (because the energy is approximately constant across the cross section):

$$\cot \delta_l(E) = \cot \delta_l(E) \Big|_{E=E_r} + (E - E_r) \frac{\partial \cot \delta_l}{\partial E} \Big|_{E=E_r} + O((E - E_r)^2). \quad (2.31)$$

The first term is zero and terms with higher powers of  $E - E_r$  are neglected. Simple calculus yields,

$$\frac{\partial \cot \delta_l}{\partial E} = -\frac{\partial \delta_l}{\partial E}, \quad (2.32)$$

and if one identifies the total width,  $\Gamma$ , with  $2(\partial \delta_l / \partial E)^{-1}|_{E=E_r}$ , then, Eq. 2.31 reduces to,

$$\cot \delta_l = -\frac{E - E_r}{\Gamma/2} \rightarrow \sin \delta_l = \frac{\Gamma/2}{((E - E_r)^2 + \Gamma^2/4)^{1/2}}, \quad (2.33)$$

where the second term is determined from simply geometry. Substituting this relation into Eq. 2.30 (and reminding ourselves we are only using one partial wave) produces,

$$\sigma_s = \pi \lambda^2 (2l + 1) \frac{\Gamma^2}{(E - E_r)^2 + \Gamma^2/4} \quad (2.34)$$

This reduces to Eq. 2.30 when on resonance (i.e. where  $E = E_r$  and  $\delta_l = \pi/2$ ).

For the reaction relevant to this dissertation, there is not only one channel, as was described above for purely elastic scattering. Taking into account spins of projectile, target, and compound nucleus modifies the statistical factor  $(2l + 1)$  and also considering different entrance (proton,  $\Gamma_a$ ) and exit ( $\gamma$  ray,  $\Gamma_b$ ) channels yields the final form of the cross section:

$$\sigma_{\text{BW}} = \pi \lambda^2 \frac{(2J + 1)}{(2j_1 + 1)(2j_2 + 1)} \frac{\Gamma_a \Gamma_b}{(E - E_r)^2 + \Gamma^2/4}. \quad (2.35)$$

This is the Breit-Wigner form of the cross section for narrow resonances, and it displays the energy dependence illustrated by simple decay in the previous section. The total width is equal to the sum of all partial widths for each possible channel:  $\Gamma = \Gamma_a + \Gamma_b$ , for this reaction. It can be noted that on resonance, the cross section is directly proportional to the product of  $\Gamma_a/\Gamma$  and  $\Gamma_b/\Gamma$ , which can be interpreted as the relative branchings for each channel. A sketch of a relative cross section is shown in Fig. 2.15.

For convenience, the statistical factor can be defined as,

$$\omega \equiv \frac{(2J + 1)}{(2j_1 + 1)(2j_2 + 1)}. \quad (2.36)$$

By defining a parameter,  $\gamma = \Gamma_a \Gamma_b / \Gamma$ , and substituting Eq. 2.36 into Eq. 2.35, the cross section can be condensed into the form:

$$\sigma_{\text{BW}}(E) = \pi \lambda^2 \omega \gamma \frac{\Gamma}{(E - E_r)^2 + \Gamma^2/4}, \quad (2.37)$$

where the quantity  $\omega \gamma$  is the *resonance strength*.  $\omega \gamma$  and the resonance energy,  $E_r$ , are the experimentally determined quantities in this dissertation. Both are needed to compute the thermonuclear reaction rate described in the following subsection.

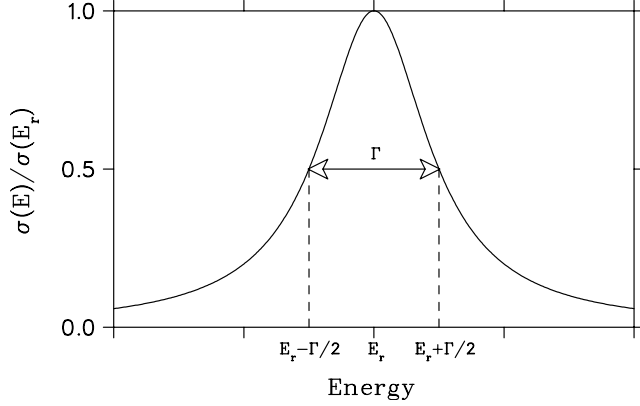


Figure 2.15: Sketch of a renormalized Breit-Wigner cross section as a function of energy, reproduced from Ref. [27].

## 2.5 Thermonuclear Reaction Rates

The basic nuclear relation of Eq. 2.12 can also be translated into a stellar context where sets of nuclei collide with some relative velocity. However, in a stellar environment such as a nova, although the quantity that is the most significant is the total nuclear energy released in the plasma per unit volume per unit time, the quantity we are interested in is the number of nuclei produced. One can transform Eq. 2.12 by dividing both sides by  $Vt$ ,

$$R \equiv \frac{N_R}{Vt} = \sigma \frac{N_b}{At} \frac{N_T}{V}, \quad (2.38)$$

where  $R$  is the reaction rate in reactions per unit volume,  $V$ , per unit time,  $t$ . This can be further simplified by substituting  $V/v$  for  $At$ , where  $v$  is the relative velocity of the particles in the plasma, and defining the beam and target densities,  $\rho_B$  and  $\rho_T$ , as the number of respective nuclei per unit volume,  $V$ :

$$R = \sigma v \rho_B \rho_T. \quad (2.39)$$

One should keep in mind that  $\sigma$  is often highly dependent on the velocity of the particles. Inside the stellar plasma, particles move with a distribution of relative velocities that are generally characterized by a probability function,  $P(v)$ . Therefore, Eq. 2.39 can be expanded to take into account a distribution of velocities, as:

$$R = \rho_B \rho_T \int_0^\infty v \sigma(v) P(v) dv = \rho_b \rho_T \langle \sigma v \rangle, \quad (2.40)$$

where the quantity  $P(v) dv$  is equal to the probability that the relative velocity is between  $v$  and  $v + dv$  for the interacting nuclei, and  $\langle \sigma v \rangle$  is the reaction rate per particle pair. This is the quantity calculated in Sec. 7.1 and contains all the nuclear physics of the reaction, which will be elucidated in subsequent sections of this chapter.

For interactions in a stellar environment, reactions are referred to as “thermonuclear” reactions because thermal motion supplies the kinetic energy to the nuclei, and their velocity distributions can be characterized by a non-relativistic Maxwell-Boltzmann distribution. Because the interacting nuclei’s absolute velocity distributions can be described by this distribution, the relative velocity distributions can be represented by it as well, with the mass replaced by the reduced mass,  $\mu$  [30]:

$$P(v) dv = \left( \frac{\mu}{2\pi kT} \right)^{3/2} e^{-\mu v^2/(2kT)} 4\pi v^2 dv, \quad (2.41)$$

where  $k$  is Boltzmann’s constant, and  $T$  is the stellar temperature. A change of variables from relative velocity to center-of-mass energy (with  $E = (1/2)\mu v^2$ ) transforms Eq. 2.41 into:

$$P(E) dE = \frac{2 \sqrt{E}}{\sqrt{\pi}(kT)^{3/2}} e^{-E/kT} dE. \quad (2.42)$$

Using the definition of  $\langle \sigma v \rangle$  from Eq. 2.40 and substituting the probability distribution in terms of energy, the reaction rate per particle pair becomes:

$$\langle \sigma v \rangle = \left( \frac{8}{\pi\mu} \right)^{1/2} \frac{1}{(kT)^{3/2}} \int_0^\infty E \sigma(E) e^{-E/kT} dE. \quad (2.43)$$

At this point, the only assumptions that have been made are that there are particles interacting in a plasma, such as a nova or other stellar objects, and that their velocity profile is non-relativistic, purely thermal, and described by a Maxwell-Boltzmann distribution. In order to simplify this expression, further assumptions must be made about the cross section for the interaction, for example, whether the reaction is non-resonant or resonant.

### 2.5.1 Narrow Resonance Reaction Rates

Due to the isolation of single resonances, the cross section can simply be defined by the Breit-Wigner formula (for non-identical particles), given by Eq. 2.35. Using this for the cross section in Eq. 2.43, the reaction rate per particle becomes:

$$\langle \sigma v \rangle = \frac{\sqrt{2\pi}\hbar^2}{(\mu kT)^{3/2}} \omega \int_0^\infty \frac{\Gamma_a \Gamma_b}{(E_r - E)^2 + \Gamma^2/4} e^{-E/kT} dE \quad (2.44)$$

If the resonances are narrow, the factor  $e^{-E/kT}$  and the partial widths may be moved through the integral with  $E$  replaced with its value at the resonance,  $E_r$ . This leaves an integral,  $\int_0^\infty dE/((E_r - E)^2 + \Gamma^2/4)$ , that can be analytically calculated and has a value of  $2\pi/\Gamma$ . Performing the integral then yields:

$$\langle\sigma v\rangle = \left(\frac{2\pi}{\mu kT}\right)^{3/2} \hbar^2 e^{-E_r/kT} \omega\gamma. \quad (2.45)$$

For multiple resonances, the total reaction rate per particle pair is simply the sum of the individual resonance contributions:

$$N_A \langle\sigma v\rangle = N_A \left(\frac{2\pi}{\mu kT}\right)^{3/2} \hbar^2 \sum_i \omega\gamma_i e^{-E_i/kT}, \quad (2.46)$$

where  $E_i$  is the resonance energy in the center-of-mass frame,  $i$  labels each resonance, and Avogadro's number,  $N_A$ , has been multiplied on both sides for convention. This is the quantity calculated, tabulated, and plotted in Sec. 7.1 for the thermonuclear reaction  $^{22}\text{Na}(p, \gamma)^{23}\text{Mg}$  for temperatures relevant to nova explosions. A reminder:  $\omega\gamma_i$  and  $E_i$  are the experimentally determined quantities in this dissertation.

## 2.6 Reaction Yield in the Laboratory

In order to calculate the reaction rate as a function of temperature in Eq. 2.46 for narrow resonances in a laboratory, the quantities that need to be determined are the resonance strength,  $\omega\gamma$ , and the resonance energy,  $E_r$ . First, one must return to Eq. 2.12. This is the simplest version of this equation, where there are  $N_b$  number of incident beam particles onto  $N_T$  number of target atoms in an infinitely thin target of area,  $A$ .

The reaction yield,  $Y$ , is defined as the number of reactions per incident particle [27], as discussed in Sec. 1.2.1. By rearranging Eq. 2.12 for a target with a volume density,  $\rho_T$ , and a thickness  $\Delta x$ , one obtains:

$$Y \equiv \frac{N_R}{N_b} = \sigma \rho_T \Delta x. \quad (2.47)$$

This thickness  $\Delta x$  can be written as,

$$\Delta x = \frac{\Delta}{dE/dx}, \quad (2.48)$$

where  $\Delta$  the energy loss of the incident beam particles in the target, and  $dE/dx$  is the energy loss per unit length as a particle traverses a nuclear medium. Substituting this relation into Eq. 2.47 results

in:

$$Y = \sigma \rho_T \frac{\Delta}{dE/dx} = \sigma \frac{\Delta}{\epsilon} \quad (2.49)$$

where  $\epsilon$  is the stopping power equal to  $\frac{dE/dx}{\rho_T}$ . This is the thin-target yield, which must be integrated over energy for thick targets and assumes a constant cross section over  $\Delta$ . The following methods outline how to calculate the yield for a thick target for each limit of Eq. 1.1, discussed in Sec. 1.2.1. The first outlined below is the conventional method, assuming a uniform target density and small-diameter beam; the second is the method used in this dissertation for a uniform beam density swept over the entire target area, where only the total number of target atoms needs to be known.

### 2.6.1 Thick-Target Yield: Peak Method

This is the conventional method of calculating the resonance yield, which assumes a uniform density target. Integrating Eq. 2.47 or 2.49 produces:

$$Y = \int \sigma(E) \rho_T dx = \int \frac{\sigma(E)}{\epsilon(E)} dE. \quad (2.50)$$

Substituting a cross section of the Breit-Wigner form in Eq. 2.35, and integrating from the energy of the beam at a position  $x$  in the target,  $E_o - \Delta E$ , to the initial beam energy,  $E_o$ , produces:

$$Y = \frac{\lambda_r^2}{2\pi} \frac{M+m}{M} \omega \gamma \frac{\Gamma}{2\epsilon_r} \int_{E_o-\Delta E}^{E_o} \frac{dE}{(E_r - E)^2 + \Gamma^2/4} \quad (2.51)$$

$$= \frac{\lambda_r^2}{2\pi} \frac{M+m}{M} \frac{\omega \gamma}{\epsilon_r} \left[ \tan^{-1} \left( \frac{E_o - E_r}{\Gamma/2} \right) - \tan^{-1} \left( \frac{E_o - E_r - \Delta}{\Gamma/2} \right) \right], \quad (2.52)$$

where  $\epsilon_r$  (usually tabulated in the laboratory frame) and  $\lambda_r$  are evaluated at the resonance energy and are assumed to be fairly constant over the resonance. With an infinitely thick target ( $\Delta \rightarrow \infty$ ) at a beam energy higher than the resonance energy ( $E_o > E_r + \Gamma$ ), the terms in the square brackets each approach  $\pi/2$  with opposite signs, and thus, the maximum yield is,

$$Y_{\max}(\infty) = \frac{\lambda_r^2}{2} \omega \gamma \frac{M+m}{M} \frac{1}{\epsilon_r}. \quad (2.53)$$

### 2.6.2 Thick-Target Yield: Integrated Method

However, if one has a thick target wherein one cares about the axial structure of the target, the longitudinal target density,  $\rho_t(z)$ , must be taken into account. Eq. 2.12 can be rewritten as,

$$Y(E_p) \equiv \frac{N_R}{N_b} = \sigma \rho_b N_T = \int_0^\infty \sigma(E(z)) \rho_t(z) \rho_b dz, \quad (2.54)$$

where  $\rho_b = \frac{dN_b}{dA}/(Q/e)$  is a beam density normalized to the accumulated charge,  $Q$ , defined in Sec. 1.2.1,  $E(z)$  is the laboratory energy of the beam as a function of depth in the target, and  $\rho_t(z) = dN_T(z)/dz$ . We can assume that the energy of the beam as it traverses the target is equal to its original energy but adjusted for the energy loss. If we also assume that the energy loss per unit length,  $dE/dz$ , is constant, then

$$E(z) = E_p - \frac{dE}{dz}z. \quad (2.55)$$

A change of variables from axial depth to energy results in:

$$Y(E_p) = \rho_b \int_{E_p}^0 \sigma(E) \rho_t \left( \frac{E_p - E}{dE/dz} \right) \frac{dE}{dE/dz}. \quad (2.56)$$

Of course, this is at a single beam energy,  $E_p$ . In reality, with a thick target, a range of energies will be needed to encompass the full resonance. Therefore, one must also integrate over beam energy:

$$\int_0^\infty Y(E_p) dE_p = \rho_b \int_0^\infty dE_p \int_{E_p}^0 \sigma(E) \rho_t \left( \frac{E_p - E}{dE/dz} \right) \frac{dE}{dE/dz}, \quad (2.57)$$

where the beam density,  $\rho_b$ , is assumed to be constant. The cross section is of the Breit-Wigner type in Eq. 2.35, but for convenience, it can be replaced by a delta function that produces the same area after integration:

$$\sigma = 2\pi^2 \lambda^2 \omega \gamma \delta(E_{cm} - \frac{M}{M+m} E_r) = 2\pi^2 \lambda^2 \omega \gamma \frac{M+m}{M} \delta(E - E_r), \quad (2.58)$$

where  $M$  and  $m$  are the mass of the target nucleus and projectile, respectively, and  $\lambda$  is defined in Eq. 1.5. The delta function ensures the cross section is equal to zero everywhere, except when the energy is equal to the resonance energy, and the factor  $\frac{M}{M+m}$  is to transform the resonance energy into the center-of-mass frame. In translating between the two forms of the cross section, the delta function identity,  $\delta(g(x)) = \delta(x - x_o)/|g'(x)|$  with  $g(x_o) = 0$ , was used. Combining the latter expression for the cross section with Eq. 2.57, one obtains:

$$\int_0^\infty Y(E_p) dE_p = \frac{2\pi^2 \rho_b \omega \gamma}{dE/dz} \frac{M+m}{M} \int_0^\infty dE_p \int_0^{E_p} dE \rho_t \left( \frac{E_p - E}{dE/dz} \right) \lambda^2 \delta(E - E_r) \quad (2.59)$$

$$= \frac{\pi^2 \hbar^2 \rho_b \omega \gamma}{m dE/dz} \left( \frac{M+m}{M} \right)^3 \int_0^\infty dE_p \int_0^{E_p} \frac{dE}{E} \rho_t \left( \frac{E_p - E}{dE/dz} \right) \delta(E - E_r) \quad (2.60)$$

where the explicit expression for  $\lambda$  has been used in the second step. Performing the integral over  $E$  results in:

$$= \frac{\pi^2 \hbar^2 \rho_b \omega \gamma}{m dE/dz} \left( \frac{M+m}{M} \right)^3 \int_0^\infty \frac{dE_p}{E_r} \rho_t \left( \frac{E_p - E_r}{dE/dz} \right) \quad (2.61)$$

Rearranging terms yields:

$$= 2\pi^2 \left[ \left( \frac{M+m}{M} \right)^2 \frac{\hbar^2}{2mE_r} \right] \frac{M+m}{M} \rho_b \omega \gamma \int_0^\infty \frac{dE_p}{dE/dz} \rho_t \left( \frac{E_p - E_r}{dE/dz} \right) \quad (2.62)$$

Changing variables from energy to back to the original variable of axial position,  $z$ , results in:

$$= 2\pi^2 \lambda^2 \frac{M+m}{M} \rho_b \omega \gamma \int_0^\infty dz \rho_t(z) \quad (2.63)$$

This integral is simply the total number of target atoms,  $N_T$ :

$$\int_0^\infty Y(E_p) dE_p = 2\pi^2 \lambda^2 \frac{M+m}{M} \rho_b \omega \gamma N_T, \quad (2.64)$$

which is Eq. 1.4 for one branch.

## Chapter 3

### EXPERIMENTAL SETUP

We measured  $^{22}\text{Na}(p, \gamma)$  resonances directly by bombarding implanted  $^{22}\text{Na}$  targets with protons from the University of Washington's 9-MV tandem Van de Graaff accelerator, which is described in detail in Ref. [54]. High currents ( $\sim 45 \mu\text{A}$ ) at lab energies ranging from 150 to 1000 keV were achieved with a terminal ion source. Of the six beamlines in the facility on which to run experiments, ours was stationed at the  $0^\circ$  position and was completely rebuilt and refurbished for this experiment. Fig. 3.1 is a panoramic photo of the  $0^\circ$  beamline, with the protons entering from the right hand side.



Figure 3.1: Panorama of  $0^\circ$  beamline. Only one Ge detector is shown on the detector platform.

Before beginning the experiment, the entire beamline was dismantled, and all reusable beam pipes were thoroughly cleaned with soap, water, and finally alcohol. The previous support for the beam pipe was removed and replaced with two 5 inch x 5 inch steel box beams, into which all support components were affixed. The beamline's two previous quadrupole magnets were reused but repositioned for the new optics. The beamline itself had one cryopump, a liquid-nitrogen cold trap, two sets of horizontal and vertical steerers, a beam scanner, and rastering coils. The chamber had its own cryopump and cold trap, and details will be discussed in Sec. 3.1. All components were aligned with a telescope.

### 3.1 Chamber

A cross-sectional view of the chamber is shown in Fig. 3.2. It was housed in a stainless steel box of 8 inch x 8 inch x 12 inch, with each face welded except one side panel which had handles bolted on for ease of handling. It was mounted on the beamline supports with adjustable feet bolted to the box.

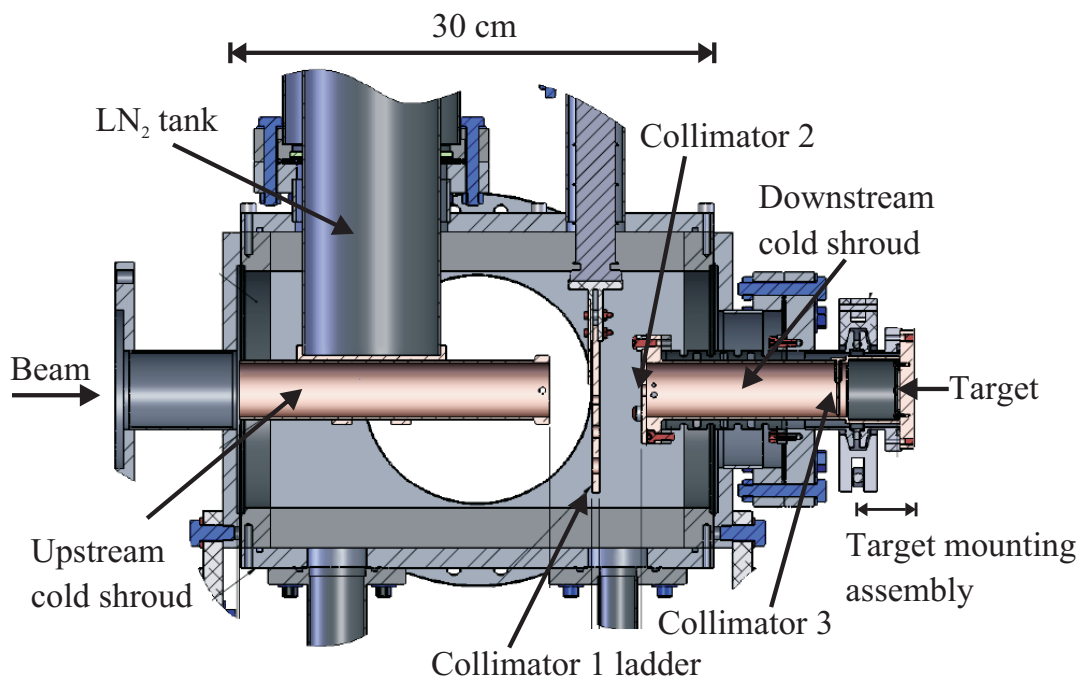


Figure 3.2: Side view of chamber cross section. Copper braids connecting the upstream and downstream cold shrouds have been omitted for clarity.

The main features of the chamber included its dual cold shroud system, three sets of collimators, and water cooled target mount.

#### 3.1.1 Cold Shroud

The cold shroud isolated the radioactive target to prevent the contamination of the upstream beamline and also helped maintain a clean environment near the target, suppressing carbon buildup.

During data collection, the pressure in the chamber was in the range of  $(1\text{-}2)\times 10^{-7}$  torr.

The cold shroud was separated into a downstream and an upstream section, connected via four copper braids (braids not shown in Fig. 3.2 for clarity). The upstream section was directly coupled to a  $2630 \text{ cm}^3$  liquid nitrogen tank, and all elements were OFHC copper to guarantee good thermal conductivity. The end of the downstream cold shroud surrounded the 1/8 inch target substrate; however, because it was the farthest away from the tank, it only reached a temperature of 125 K, whereas the upstream shroud reached 88 K, as shown in Fig. 3.3.

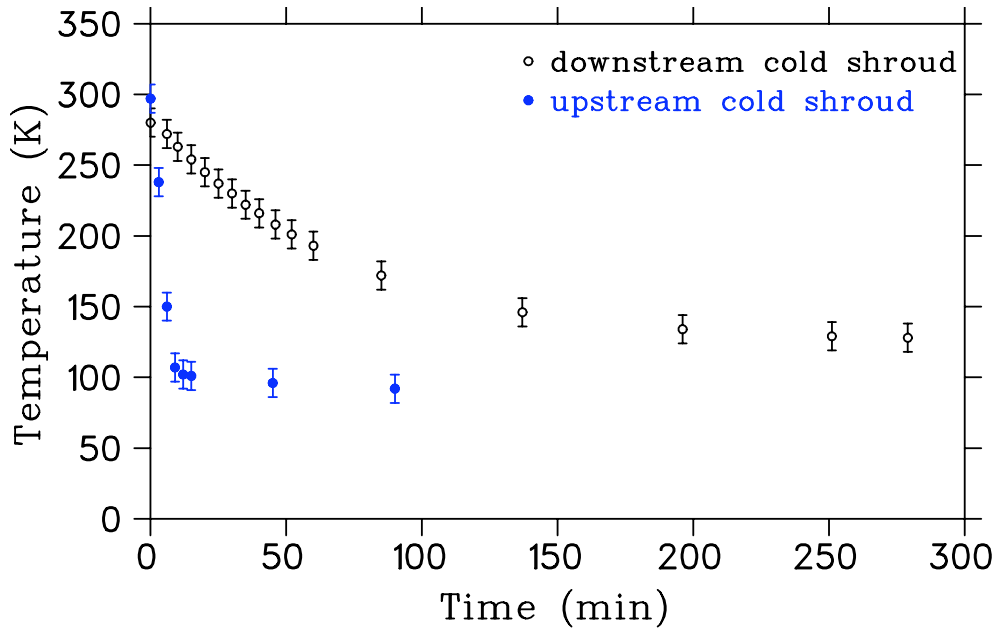


Figure 3.3: Cooling of the cold shroud as a function of time.

### 3.1.2 Apertures

The chamber had three sets of collimators. The first, collimator 1, was a water-cooled, sliding ladder between the cold shrouds with 4-, 7-, and 8-mm diameter collimators. The 8-mm collimator was used during  $^{22}\text{Na}(p, \gamma)$  data acquisition. Also on this ladder were electron-suppressed 1-mm and 3-mm diameter collimators with downstream beam stops for tuning. An 8-mm collimator, collimator 2, was 33 mm downstream of the ladder and was attached to the end of the downstream cold shroud. It was followed by a 10-mm diameter cleanup collimator, collimator 3, located 122 mm

farther downstream. Each collimator was electrically isolated from the chamber to permit current monitoring.

### 3.1.3 Target Mount

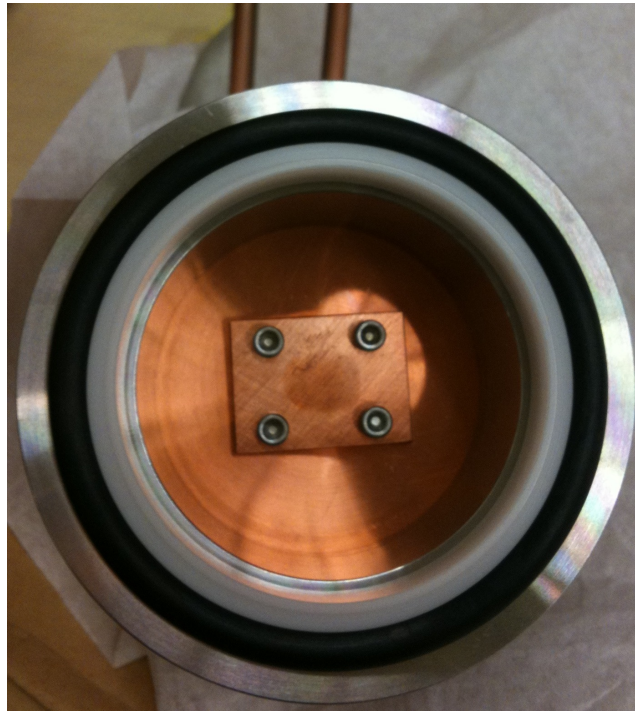


Figure 3.4: Photo of target and target mount, beamside view.

A photo of our target mount is shown in Fig. 3.4. The 1/8 inch target substrate was bolted to a copper backing flange and was directly cooled with deionized-water via a thin pipe coupled to the flange. This pipe was welded to an aluminum disc, which bolted to the backing plate, along with a return line. Air cooling was found to be insufficient. To minimize contact with the radioactive targets, this assembly was then bolted to a stainless steel coupler with a Kwik-Flange connector on the chamber side. Once mounted, the only target handling necessary involved snapping this Kwik-Flange on and off the chamber. Directly upstream of this assembly was a 30-mm long electron suppressor biased between  $-150$  and  $-300$  V. During data collection, the current on target was monitored, and the charge was integrated and recorded.

### 3.2 Detectors

Two sets of detector systems were positioned  $\pm 55^\circ$  to the beam axis. A top view of the setup, including chamber, shielding, and detectors with Dewars, is shown in Fig. 3.5. Photos are shown in Fig. 3.6 and 3.7.

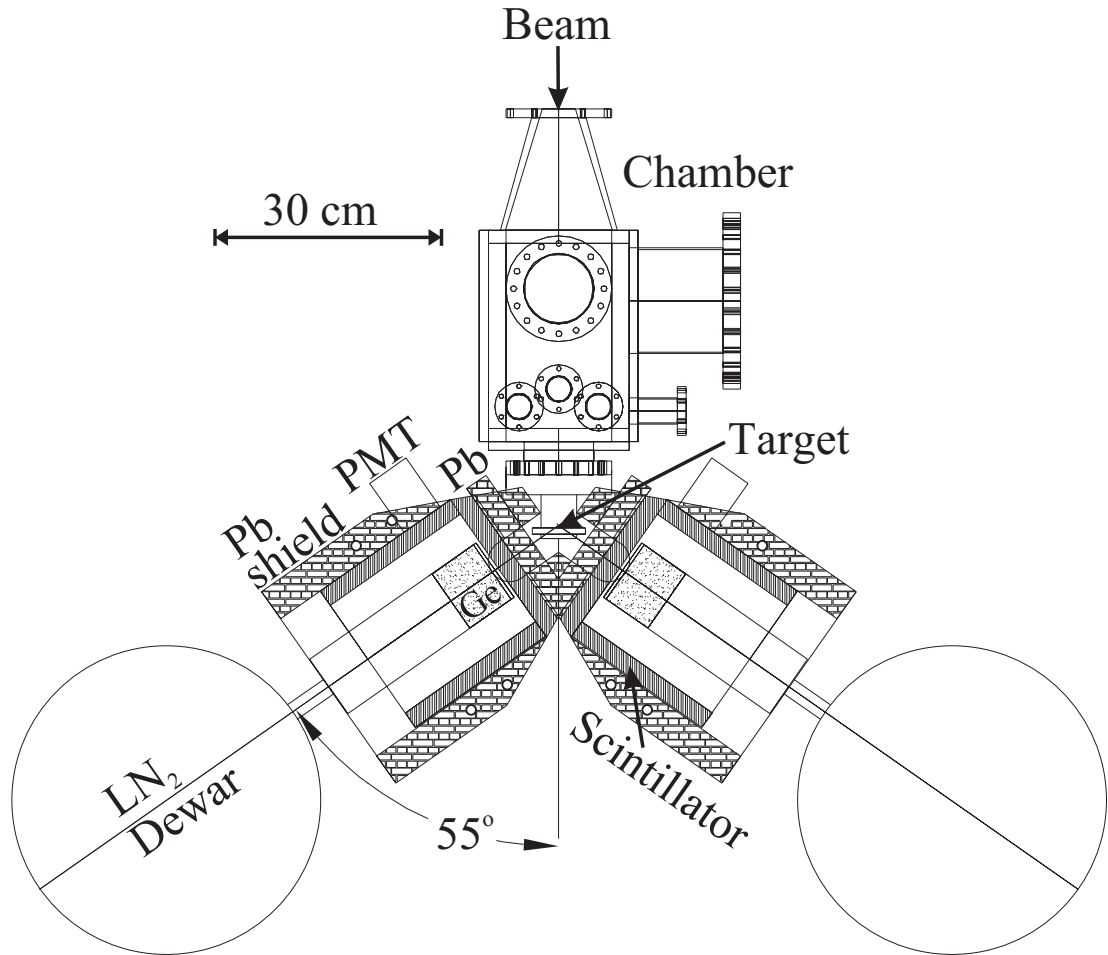


Figure 3.5: Top view of detector setup. The PMT shown is for the annular scintillator only; the planar scintillator PMT has been omitted for clarity.

This angle was chosen to minimize effects due to possible angular anisotropies, as the Legendre polynomial  $P_2(\cos 55^\circ) = 0$ . Each system consisted of one high-purity germanium detector encased in cosmic-ray anticoincidence shielding and was separated from the target mount by 26 mm of

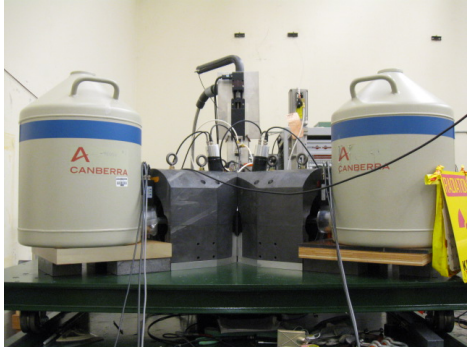


Figure 3.6: Photo of detector setup.

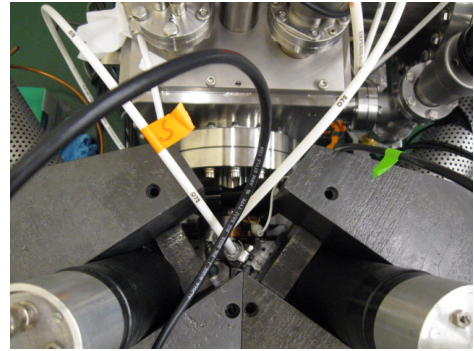


Figure 3.7: Photo of detector setup, close-up.

lead along the beam axis.

### 3.2.1 High-Purity Germanium Detectors

The high-purity germanium (HPGe) detectors were Canberra GR10024 with a relative efficiency of 100%, as compared with 3 in  $\times$  3 in NaI. A cross sectional view of the detector is shown in Fig. 3.8. The resolutions for each detector at 1.275 MeV were 4.4 keV and 7.4 keV (FWHM) at high rates ( $^{22}\text{Na}$  target present), and 2.2 keV and 3.0 keV (FWHM) at low rates (using residual  $^{22}\text{Na}$  activity with  $^{22}\text{Na}$  target removed).

A sample spectrum from one of these detectors is shown in Fig. 3.9. The strongest signal is the 1275-keV line from the radioactive source, and its double and triple signal pile-up can also be seen at 2550 and 3825 keV, respectively. Also clear is a signal from the 511-keV gamma rays and its pile-up with the 1275-keV gamma rays at 1786 keV. The two thresholds at low energies are discussed in Sec. 3.3. Even with the strong  $^{22}\text{Na}$  source in place, the spectrum above  $\sim 4$  MeV was very clean, which was the energy regime where this experiment focused. Here, the dominant contribution to the background was not from the radioactive source but from cosmic rays, as discussed in Sec. 3.2.2.

### *Shielding*

As was discussed in Sec. 1.2.2, the main challenge of this experiment was the highly radioactive target, which produced signals that would have overloaded the detectors without taking preventative steps. A simple way to reduce the event rate in the detectors to a few tens of kHz was to place some

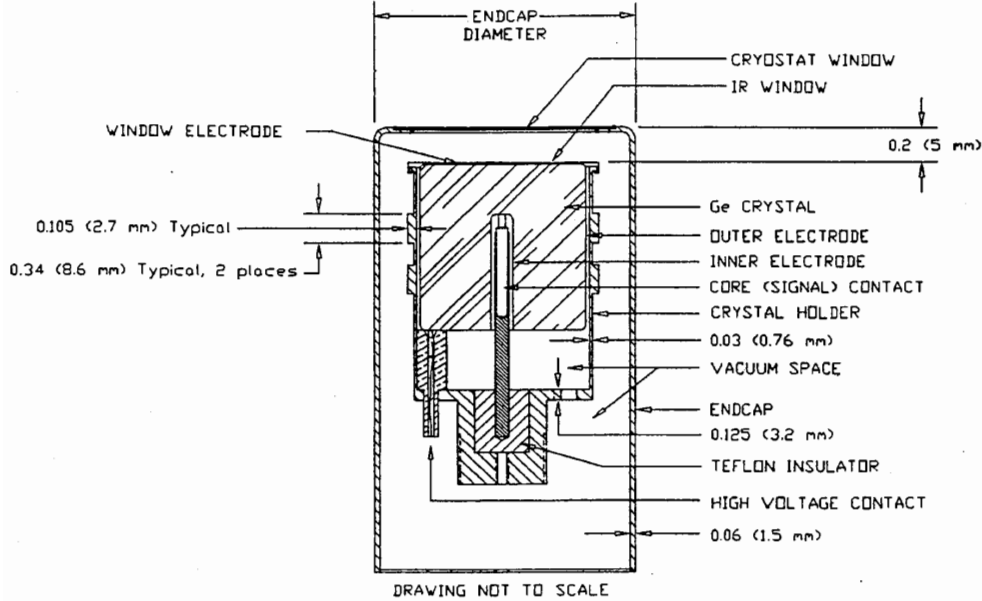


Figure 3.8: Cross section of germanium detector.

high-Z material between the radioactivity and the detectors. In order to determine what material to choose as shielding, simulations were performed with PENELOPE, a Monte Carlo code which simulates electron-photon transport in arbitrary materials [55, 56]. More simulation detail is discussed in Sec. 4.1.2. The figure of merit used to compare materials was the ratio of the photopeak efficiency for 5-MeV gamma rays to the total efficiency for 1275-keV gamma rays. Several configurations of varying thickness of copper and lead (used together or separately) were considered; however, the ratio remained relatively constant. For ease of fabrication, 26 mm of lead was chosen. According to the simulations, the lead reduced the counting rate for the 511-keV gamma ray by a factor of 70, whereas the photopeak from 1275-keV gamma rays was reduced by a factor of 5. The suppression ranged from factors of  $\sim 3.5$  to 4.5 for gamma rays with energies above  $\sim 5$  MeV.

### 3.2.2 Cosmic-Ray Anticoincidence Shields

The bulk of the background at gamma-ray energies higher than  $\sim 4$  MeV was from cosmic rays. In order to remove these unwanted signals, annular and planar plastic scintillators encased in lead were used in anticoincidence with the germanium detectors. The reduction of the  $^{22}\text{Na}(p, \gamma)$  signal

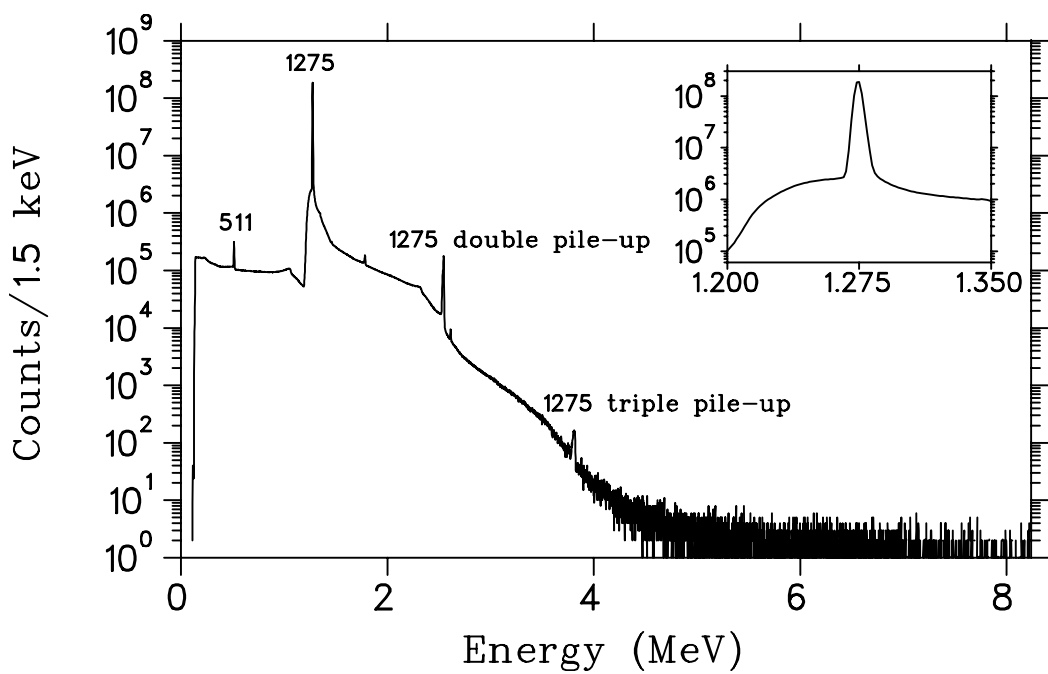


Figure 3.9: Sample background spectrum from one Ge detector, measured for  $\sim 160$  hours. Inset shows the spectrum expanded around the 1275-keV gamma ray. Gamma rays from  $^{22}\text{Na}(p, \gamma)$  are between  $\sim 5$  and 8 MeV, where the dominant background is from cosmic rays. A discriminator was used to suppress the rate directly below the 1275-keV line, as discussed in Sec 3.3.

by this veto was negligible. A photo of these shields separated from the germanium detectors is shown in Fig. 3.10, and a sketch is shown in Fig. 3.11.



Figure 3.10: Photo of cosmic ray shields. The scintillator in the foreground has had its top lead casing removed.

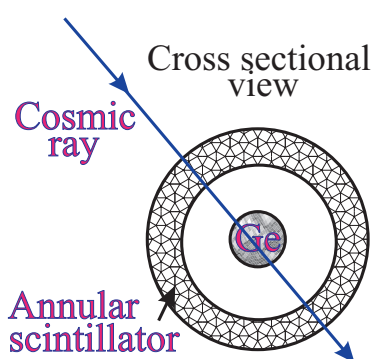


Figure 3.11: Sketch of cosmic ray entering both the annular scintillator and Ge detector.

When cosmic rays enter scintillators, they excite the material, which, upon de-excitation, produce photons, or scintillation light. The scintillators were wrapped first with reflective aluminum foil and then with black plastic, and finally light leaks were halted with black tape along any seams. It is this signal that was used in anticoincidence with the germanium signals in order to filter out the cosmic-ray background. The details of the electronics and integration into the data acquisition is discussed in Sec. 3.3.

Because funding for new scintillators could not be procured, an existing setup was modified to fit the needs of this experiment; therefore, their geometry was not optimal, as each annulus had a diameter 2.3x that of the germanium crystal. However, they still greatly aided in cosmic-ray rejection. The setup included an annular plastic scintillator as well as a front planar scintillator, both of which fit inside a large lead covering. Previously, the photomultiplier tubes on each annulus had been directly coupled to the flat surface on the back, which was unacceptable for this experiment as they collided with the large liquid-nitrogen Dewars for the germanium detectors. Thus, the PMTs on each annulus had to be moved to the cylindrical side where they would no longer interfere. The planar scintillators posed no problem.

In contrast to their previous construction, the PMTs now required light guides to couple their flat faces to the curved cylindrical surface. Small cylinders of polished lucite were machined to facilitate this coupling and were glued with optical cement directly onto scintillator. The PMTs were then glued onto the light guides, which were then covered in black tape to prevent light leaks. In order to accommodate the new PMT positions, the lead covering also had to be modified, and to protect the PMTs, cylindrical cages were machined and affixed to the lead. To test their ability to reject cosmic rays, an experiment was performed with 50% germanium detectors, and the results are shown in Fig. 3.12 as a function of energy and PMT threshold settings.

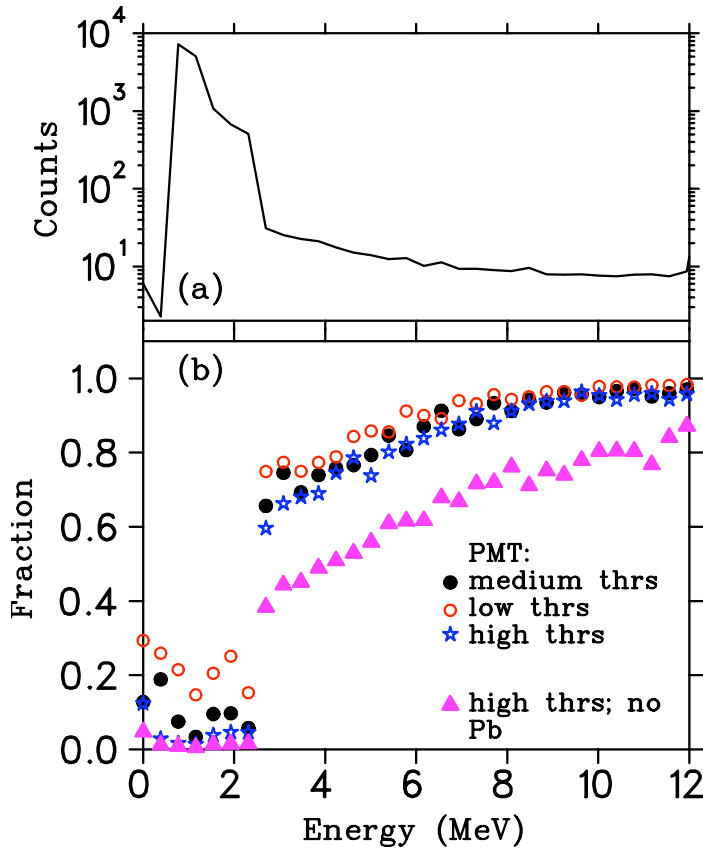


Figure 3.12: Panel (a) shows the raw amplitude spectrum from one of the 50% Ge detectors, and panel (b) shows the fraction vetoed with the anticoincidence system. Each is a function of gamma-ray energy. The sharp rise at  $\sim 2.6$  MeV illustrates the dominant background shifting from room background at low energies to cosmic-ray background at higher energies.

As shown in Fig. 3.12 (a), the dominant background at low energies originates from the room

(mostly  $^{40}\text{K}$  at 1460.8 keV and  $^{208}\text{Th}$  at 2614.5 keV) and not from cosmic rays; therefore, there is a large jump in rejected fraction above the room background gamma-ray energies. Even with a non-optimal geometry, the rejection at 5 MeV was 80%. Also, the lead encasing was kept because, as the figure illustrates, the lead helps to convert a fraction of cosmic rays into particles detectable by the plastic scintillators. Rejection data from the  $^{22}\text{Na}(\text{p},\gamma)$  experiment will be discussed in the next section.

### 3.3 Data Acquisition

In addition to the signals from the high-purity Ge detectors, the electronics also processed PMT signals from the scintillators. In order to reduce the rate seen by the detectors due to target radioactivity, two techniques were used: 1) lead shielding was installed as described above, 2) a high threshold on the Ge detectors was set just below the strong 1275-keV  $^{22}\text{Na}$  line, so that the target activity could be monitored *in-situ*.

The Ge-signal amplifiers (ORTEC 672) were operated in a pile-up-rejection mode (causing a dead time of  $\sim 40\%$ ) to minimize signal distortion. After being triggered by an initial pulse, this mode allowed the rejection of subsequent pulses (and the initial pulse) if they occurred within a fixed time window of  $27\ \mu\text{s}$  (equal to fixed factor of 9 times the shaping time). If this condition was met, a logic signal was triggered and used in anticoincidence with the main gate for the ADCs. When performing high-rate experiments, one must also balance the desire for fast processing to minimize pile-up with longer amplifier shaping times to maximize charge collection and resolution. Therefore, a  $3\text{-}\mu\text{s}$  shaping time was chosen. To note, two discriminators were used on the timing signal from each Ge preamplifier. The Constant-Fraction-Discriminator (CFD) enabled a high timing resolution to use as a start for the TAC (the first threshold slightly above 0 MeV in Fig. 3.9), whereas the Timing-Signal-Channel-Analyzer (TSCA) allowed for a sharp energy cut directly below the 1275-keV gamma ray (the second threshold around 1.2 MeV in Fig. 3.9).

Signals from the two sets of detectors were fed into analog NIM-standard modules and converted into digital signals by two ORTEC AD413A CAMAC Quad 8k ADCs with fast FERAbus readout. These multiplexed ADCs had four inputs each, a  $6\text{-}\mu\text{s}$  conversion time per active input, and a 100 ns/word FERAbus readout, which helped to reduce dead time. A buffer module was used

to minimize the communication with the computer via a CAMAC interface. JAM, a JAVA-based data acquisition and analysis package for nuclear physics [57], was used to process the data. All the NIM and CAMAC electronics modules were located in a temperature-controlled rack to minimize instabilities. The raw rate in each detector was below 30 kHz, and the ADC rate was  $\sim 4$  kHz.

The anticoincidence shields were an important feature of the data acquisition system. Signals from the active anticoincidence shields and from the Ge detectors were used as a stop and start, respectively, in a Time-to-Amplitude-Converter (TAC). If these two signals occurred within a set timing window, the resulting Ge signal was discarded. The exact details of this are discussed in the following subsection.

In order to determine the live-time fraction for our detectors, a signal from a pulser unit was fed into the “test” port of each Ge preamplifier, creating an additional signal in the corresponding amplitude spectra. This signal was sorted into its own spectrum by a logic signal to the data acquisition. A window of comparable width to the energy window for the yield was placed on the prompt pulser signal and compared to the scaled number of pulser pulses. This ratio gave the live time, which ranged from 35 to 45% for the radioactive targets and was above  $\sim 90\%$  for all other targets. The live-time correction was substantial, but it was not beam related; instead it resulted from a constant rate due to the radioactivity. To test the accuracy of the live-time correction, a thick  $^{27}\text{Al}$  target was irradiated with protons with and without a  $^{22}\text{Na}$  source nearby. Although the presence of the radioactivity decreased the live time from 97% to 50%, the ratio of the live-time corrected yields was  $0.99 \pm 0.02$ .

### 3.3.1 *Signals: Amplitude, TAC/Veto, Scalers*

A diagram of the electronics for one detector is shown in Fig. 3.13. Notes have been made where the second detector system is folded into the acquisition; otherwise, its electronics are exactly the same. For each of the two detector systems, there were two copies of the amplitude signals from the germanium, one used strictly for the energy analysis and the other used for timing and for cosmic-ray rejection. There were also two PMT signals, one from the annular scintillator and one from the planar scintillator. Along with these, there was one pulser signal and one signal from the TAC used for the anticoincidences.

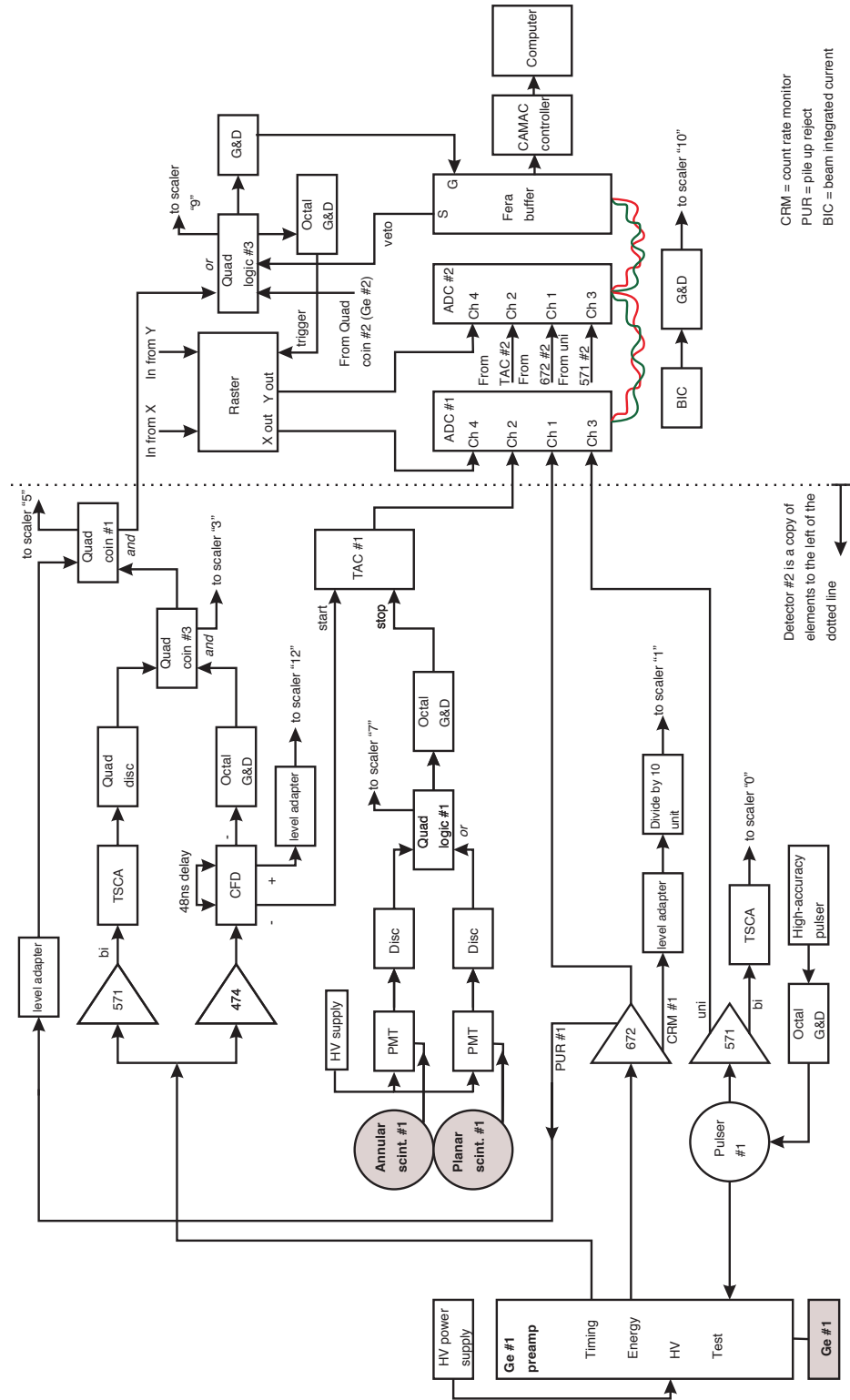


Figure 3.13: Electronics diagram. Detectors (germanium and scintillator) are shaded. Shown is detector #1 only; detector #2 is a copy of all elements to the left of the dotted line. Notes have been made where the second detector system is folded into the acquisition; otherwise, its electronics are exactly the same.

Each ADC had four inputs: energy amplitude from the Ge detector, TAC signal, pulser signal, and either horizontal or vertical raster signal. In the data acquisition program JAM, nine main histograms were produced from the above signals for each detector system: raw energy spectrum, vetoed energy spectrum, pulser spectrum (sorted from the energy spectrum), pulser spectrum (directly from its generator), TAC spectrum, 2D energy verses TAC spectrum, raw raster spectrum, and gated raster spectrum. Counts were sorted into the vetoed energy spectrum if they were in anticoincidence with the TAC signal, explained in detail in the next subsection. A pulser signal was routed directly into the ADC and also into the “test” port as described above. The latter causes its signal to appear in the energy spectra; thus, if its ADC channel fired, it was routed it to its own histogram. The signals from the rastering device are explicitly discussed below in Sec. 3.3.2, but it was possible to set a gate on an energy region of interest in the vetoed energy spectrum and sort out the corresponding raster signal to its own histogram (“gated raster spectrum”). In addition to ADC signals, there were a number of scaler signals that were used to monitor count rates at various stages of signal processing, to record the total number of incident protons, and to aid in calculating the live time with the direct pulser signal.

Two modes of data acquisition were possible and have different advantages. When a signal triggered the ADC, all signals in each input channel were read as an “event”. In “event mode,” these signals were recorded exactly and relationships among signals are retained, which allows a subsequent full offline analysis, enabling the complete re-sorting of any event into any histogram. Clearly, this is the most flexible for analysis; however, this mode requires a large amount of hard drive space and should be used only when the necessity of re-sorting of data is likely. On the other end of the spectrum, “singles” mode simply records the values of each ADC conversion into histograms according to gates set up in JAM, previously fixed by a java sort code. These events cannot be correlated with one another and cannot be resorted, but required computing space is greatly reduced. Most of our  $^{22}\text{Na}(p, \gamma)$  data was taken in this mode.

### TAC

In order to determine the bounds of the TAC spectrum for data processing, the TAC signal corresponding to gamma rays only with energies between 4 and 6 MeV was extracted, a sample of which

is shown in Fig. 3.14.

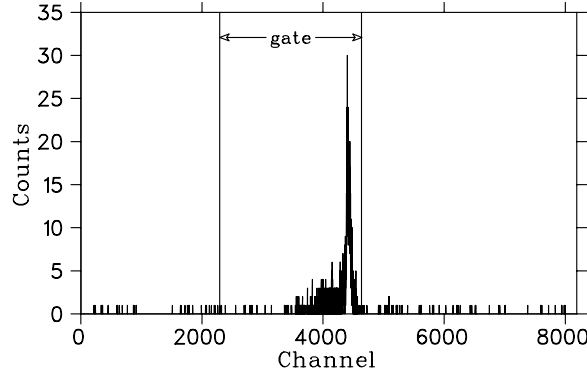


Figure 3.14: Sample TAC spectrum. Ge and scintillator signals were used as a start and stop, respectively, and shown is the signal from cosmic rays with energies between 4 and 6 MeV with 82 ch/ns. The gate for the veto is indicated and is asymmetric to include the tail on the time spectrum.

The timing gate was set on the prompt peak, which had a long tail to its left. This occurs because the Ge crystal is coaxial with a large radius (3.875 mm), and signals that occurred closer to the outer radius have a longer collection time. Because the TAC was *started* with the Ge signals, this corresponds to shorter time differences in the TAC spectrum. A 2D amplitude verses non-gated TAC signal spectrum is shown in Fig. 3.15, and the intensity of the signals are indicated by color.

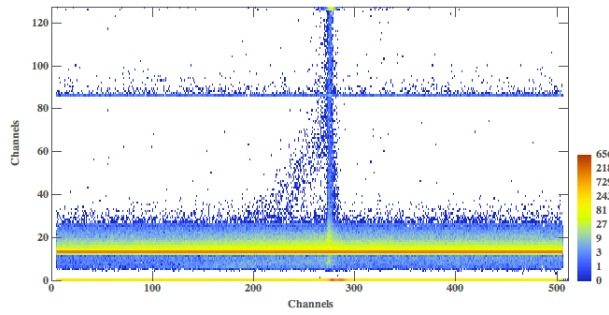


Figure 3.15: Sample energy verses TAC spectrum.

Most signals occurred at low energies with a random sampling of times (the bright yellow band). The prompt TAC peak at  $\sim 280$  ch is clear and distinguishable from the tail which drops down to

the left. The horizontal signals around an amplitude of  $\sim 85$  ch (corresponding to 8.3 MeV) are accidentals from the pulser.

The TAC signal for most high-energy cosmic rays from  $\sim 6$  to 11 MeV also falls within the set window shown in Fig. 3.14. The scintillators' PMT thresholds were set well above 511 keV to avoid vetoes by annihilation radiation and to decrease detector rate. One also would like to avoid vetoing the 1275-keV gamma rays, as those are coincident with the 511-keV gamma rays. Because the veto rate was a maximum of  $\sim 50$  Hz, accidental veto was quite low. Self veto was possible with cascade gamma decays if one gamma ray was registered in the Ge and the other in the anticoincidence shield; this was examined by comparing the yields from raw singles spectra with the those from the vetoed spectra, which agreed to better than 99%. The effect of the anticoincidence shielding for the  $^{22}\text{Na}(p, \gamma)$  setup is shown in Fig. 3.16. In the energy region above  $\sim 5$  MeV, the anticoincidence system rejected  $\sim 80\%$  of the cosmic-ray background signal.

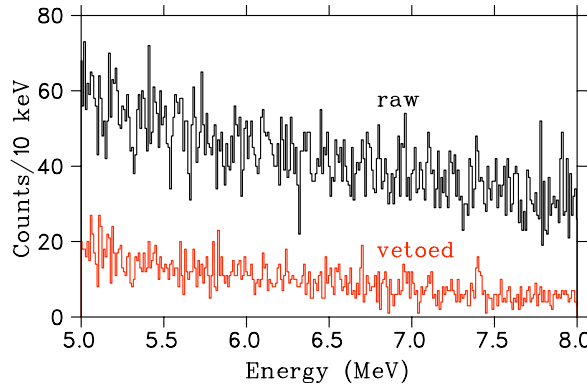


Figure 3.16: Sample background gamma-ray energy spectrum, illustrating the effects of the veto.

### 3.3.2 Rastering

The beam was rastered using a magnetic steerer located 1 m upstream of the target. A rectangular pattern with 19- and 43-Hz horizontal and vertical frequencies was used, and signals proportional to the magnetic field were produced by integrating the voltage signals from a pickup coil located in the raster magnet. These readout values represent the center of the beam spot, if the beam is steered through the center of the beam pipe. For each data set collected, a 2D histogram of this

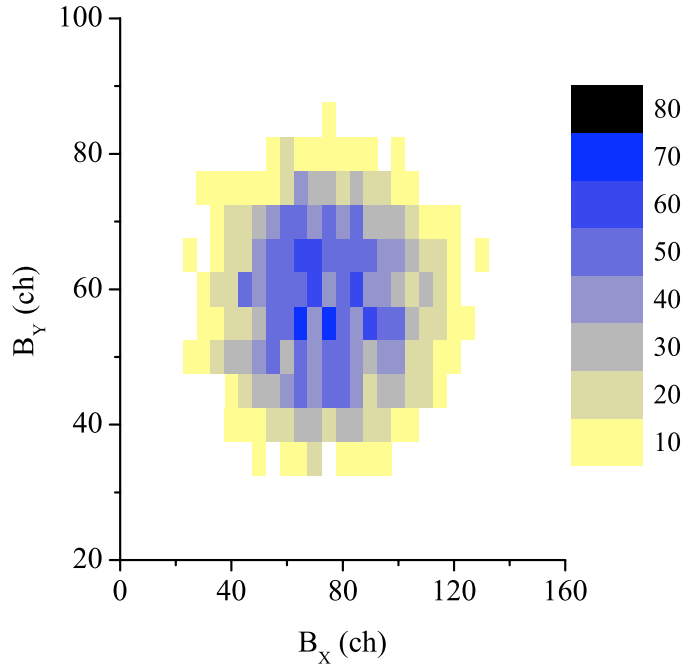


Figure 3.17: 2D raster plot on the “coin” target: a 5-mm diameter  $^{27}\text{Al}$  disc embedded in copper.  $B_x$  and  $B_y$  are proportional to the magnetic field of the raster. Shown is a histogram of the raster signal during a measurement of the 406-keV  $^{27}\text{Al}(p, \gamma)$  resonance, with a wide gate ranging from above the 7358-keV gamma ray to below its first-escape peak.

signal in both horizontal and vertical directions was recorded. It was also possible to set a gate on the energy spectrum of each detector and sort out the corresponding raster positions. For each measured resonance, the amplitude for the raster was scaled as the square root of the proton energy, so the rastered area of the beam on target would be constant.

Fig. 3.17 shows this 2D raster plot, obtained with a 5-mm diameter, 1.5-mm thick  $^{27}\text{Al}$  disc embedded in the center of a copper backing. This “coin” target had the same OFHC copper substrate and diameter as our  $^{22}\text{Na}$  targets. Shown are the counts detected for each value of the rastering field in the two dimensions. During all data-taking, the raster signals were monitored in order to diagnose problems with the target or other issues that may have arisen.

### 3.4 Targets

Isotopic purity and stability are essential characteristics of targets involved in nuclear astrophysics measurements. Ion-implantation into a substrate allows for both, while avoiding complications with chemical fabrication. However, as was discussed in Sec. 1.2.2, target degradation after prolonged bombardment remains a formidable challenge. Beam effects such as sputtering and heating must be monitored and quantitatively known, and diffusion could also play a role. Two types of sodium targets were fabricated for this experiment: radioactive  $^{22}\text{Na}$  and its stable isotope  $^{23}\text{Na}$ .

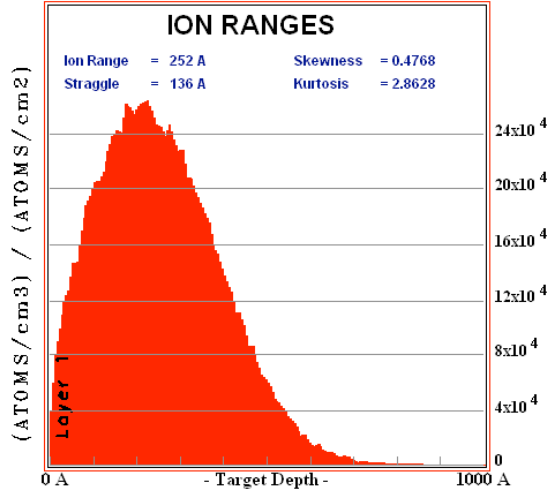


Figure 3.18: TRIM simulation of a 30-keV  $^{22}\text{Na}$  beam implanted into a copper substrate.

Two sets of radioactive targets were produced at TRIUMF-ISAC, and, in between sets, a multitude of  $^{23}\text{Na}$  target tests were performed in order to further understand the behavior of the radioactive targets and to discover if a better substrate and/or implantation energy for  $^{22}\text{Na}$  production existed [18]. A sample implantation profile simulated with TRIM [58] is shown in Fig. 3.18. Because the widths of the resonances discussed in this dissertation are on the order of eV, the implantation profile dominated the shape of the excitation functions.

As outlined in Sec. 1.2.1, the parameter needed from the targets in order to extract the resonance strength is the total number of atoms. From all types of implanted targets, this quantity can be inferred from the integrated charge, which can have non-negligible systematic errors if the electron

suppression is not handled properly (see Sec. 3.4.2). In addition to integrated charge, for radioactive targets the activity can also be used to extract the total number of atoms, if the efficiency of the characteristic gamma ray is well known. For our experiment, only this method is used for  $^{22}\text{Na}(p, \gamma)$ .

### 3.4.1 $^{22}\text{Na}$ Targets

Two sets of  $^{22}\text{Na}$  targets were implanted at TRIUMF using the Isotope Separator and Accelerator facility (ISAC). Each target was made by implanting a 10-nA, 30-keV  $^{22}\text{Na}^+$  ion beam into a rectangular OFHC copper substrate with dimensions  $3\text{ mm} \times 19\text{ mm} \times 25\text{ mm}$ . The beam was rastered over a 5-mm diameter collimator such that at the raster extreme only 5% of the beam remained on target, thereby creating a nearly uniform density. The setup included electron suppression with  $-300\text{ V}$  and a liquid-nitrogen cooled cold trap with a vacuum pressure in the range of  $6 \times 10^{-8}$  to  $2 \times 10^{-7}$  torr. Charge integration was monitored throughout the implantation process, which took roughly 24 hours per target with a  $^{22}\text{Na}$  current of  $\sim 15\text{ nA}$ .

In 2005, 185 and  $300\text{ }\mu\text{Ci}$  targets were fabricated and left in air to wait until  $^{22}\text{Na}(p, \gamma)$  data taking began in summer of 2008. As target degradation can be quite problematic, we carried out a program [18] to determine the ideal combination of implantation energy, substrate, and possible protective layer by bombarding  $^{23}\text{Na}$  targets implanted under similar conditions. Using the conclusions of Ref. [18], in December 2008, two additional  $\sim 300\text{ }\mu\text{Ci}$   $^{22}\text{Na}$  targets, #3 and #4 ( $\sim 1.3 \times 10^{15}$  atoms), were implanted with the same parameters but included a 20-nm protective layer of chromium, deposited by vacuum evaporation after implantation. A small rise in temperature of the target was observed during the evaporation; however, a survey of the apparatus showed no residual activity from diffusion of  $^{22}\text{Na}$  out of the target. All  $^{22}\text{Na}$  data presented were taken on the chromium-covered targets, with the exception of the 232-keV resonance measurement which employed bare target #1.

To explore the transverse location of the implanted  $^{22}\text{Na}$ , the beta activity was scanned with a Geiger counter behind a 6-mm thick brass shield. A 3-mm diameter hole in the center allowed transmission of the beta particles, and the gamma rays presented a nearly constant background. The results for target #3 are shown in Fig. 3.19 (a), along with a corresponding geometric model, panel (b). The beta count rate in the model is proportional to the areal overlap of the hole and the

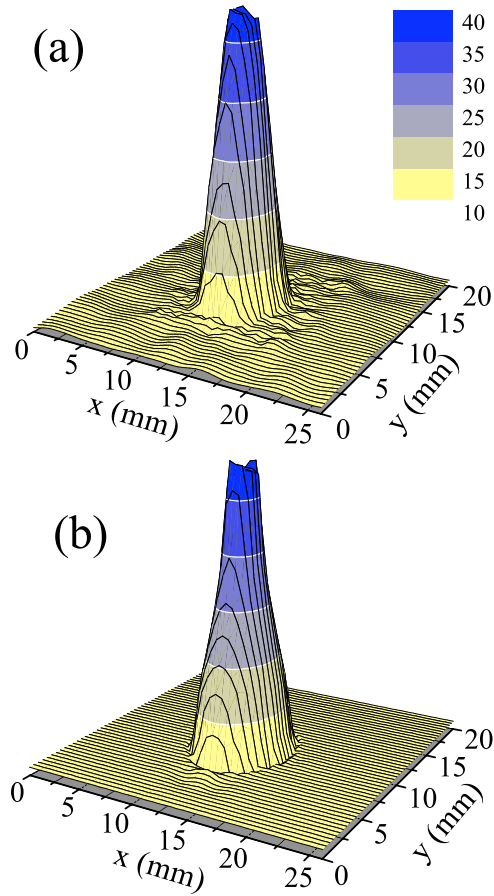


Figure 3.19: Plots representing the count rate recorded in a Geiger counter per data point from a scan of target #3 with a 3-mm diameter collimator. The distance between the target and counter was  $\sim 10$  cm, and the baseline is greater than zero because the Geiger counter detected events caused by gamma rays and beta particles. (a) shows the dead-time corrected ( $\sim 30\%$ ) experimental data. (b) shows the results of a simple geometrical model normalized to, and centered on, the experimental data, where the relative beta count rate is assumed to be proportional to the areal overlap of a uniform 5-mm diameter source of activity and the collimator.

activity, under the assumption the activity is evenly distributed over a 5-mm diameter circle. This measurement confirmed that the  $^{22}\text{Na}$  was confined within a 5-mm diameter circle and determined the position of the activity relative to the center of the substrate. Although this method was not very sensitive to radially-dependent non-uniformity, it did verify axial symmetry. Thanks to this information and the extreme rastering of the  $^{22}\text{Na}$  beam, we believe the targets were quite uniform, although our method does not require this.

### 3.4.2 $^{23}\text{Na}$ Targets

In order to fabricate the most ideal, durable targets, a multitude of tests were performed with  $^{23}\text{Na}$ , the stable isotope of sodium [18]. Parameters that were varied included the implanting beam energy (ranging from 10 to 30 keV), the substrate (copper, nickel, and tantalum), the covering material (none, chromium, and gold), and cooling mechanism (air and water). We found targets implanted at 30 keV into OFHC copper, water cooled, and covered with 200 Å of chromium to be the most robust of our sample set, losing an amount consistent with zero loss after  $\sim 20$  C of proton beam bombardment.

The  $^{23}\text{Na}$  targets were implanted using the low energy end of the tandem Van de Graaff accelerator at CENPA from a sputter ion source. In order to produce a source of  $^{23}\text{Na}$ , NaCl was mixed with silver (used as a conductive material) and compressed into pellet form. This pellet was then installed into the sputter ion source, which produced a beam of  $^{23}\text{Na}^-$  ions. In order to ensure the beam had a high purity of only the isotope desired, the beam exiting the ion source was bent through a 90° dipole magnet ( $M/\Delta M = 100$ ). The beam was then rastered in a square pattern with horizontal and vertical frequencies of  $\sim 0.1 - 0.3$  Hz using a window-box steering magnet with discretely changing currents. The beam then traveled through a cold trap 14 cm upstream of the target before encountering the implantation setup. A sketch of a top view of the setup is shown in Fig. 3.20.

The setup consisted of a collimator (either 0.5 or 1 cm in diameter, biased to +300 V), a grounded electron suppressor, and a target plate (also biased to +300 V). This configuration of biases prevented electrons knocked out by  $^{22}\text{Na}$  ions from leaving the target or collimator and is supposed to ensure a correct current reading off both the collimator and target. This is necessary to infer total number of implanted atoms from integrated charge. This setup, however, does not suppress

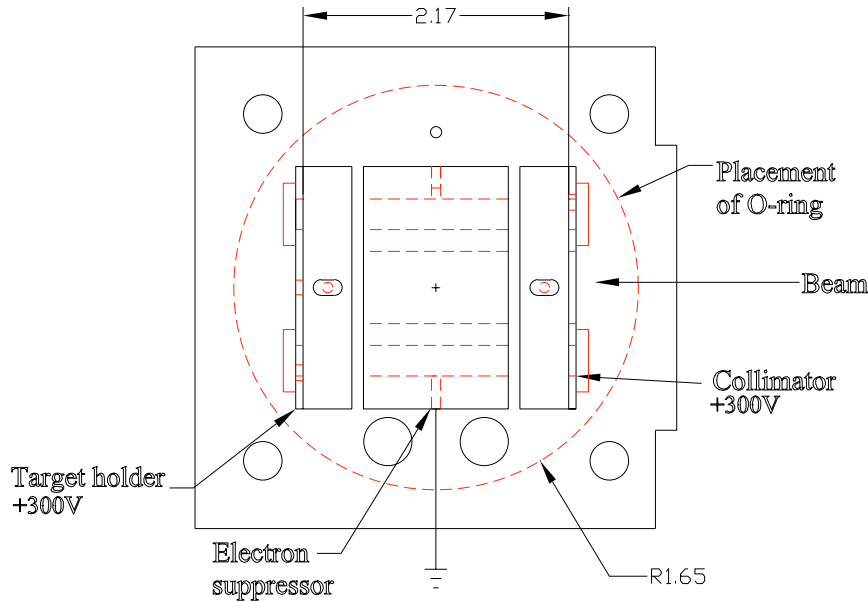


Figure 3.20: Sketch of  $^{23}\text{Na}$  implantation setup. Top view. All dimensions are in inches.

sputtering of positive ions, which can lead to an incorrect value for the ion current hitting the target.

During implantations relevant to this dissertation, the current on the suppressor was not monitored. However, in subsequent implantations for other experiments, it was revealed that there was a non-zero current on the suppressor, leading to an incorrect integration of the ion current incident on the target. Therefore, an investigation of this current was necessary in order to ascertain from where the current was originating and if the ratio of suppressor current to target current was constant, so that a simple correction could be applied to the total number of atoms.

A battery of current measurements with a beam of  $^{23}\text{Na}^-$  several months after the original implantations were performed on the target, suppressor, and collimator. The bias on the collimator was decreased to 0 V, which had significant effect on the collimator current but no effect on either the target or the suppressor current. This means when electrons were knocked off, they traveled upstream away from the target and suppressor, and thus, were not the source of the current on the suppressor.

Then the ratio of currents on the suppressor to the target was measured with different raster positions. While keeping the field on the horizontal raster fixed and varying the vertical field (and vice

versa), this ratio of currents remained approximately constant, and the sum of the target, suppressor, and collimator current was roughly equal to the total current measured upstream in the off-deck Faraday cup. This indicated the ratio was independent of the beam position and could be used to correct the number of implanted atoms.

We concluded that the atoms were positively charged and drawn to the grounded electron suppressor; therefore, the integrated charge on the target was not equal to the total number of implanted  $^{23}\text{Na}$  atoms. Measurements of the ratio of current on the suppressor to current on the target indicated that the total number of atoms deduced from integrated charge was  $13.5 \pm 2.0\%$  higher than the true number of implanted atoms. This correction was also applied to the  $^{23}\text{Na}(p, \gamma)$  resonance strength, discussed in Sec. 5.7.

## Chapter 4

### **CHARACTERIZATION OF EXPERIMENTAL PROPERTIES**

In order to extract the resonance strength using Eq. 1.4, knowledge of the absolute detector efficiency, total number of  $^{22}\text{Na}$  atoms, and various beam properties including the beam density was required and is discussed in this chapter. However, although this includes the determination of the *initial* number of target atoms, our treatment of potential target degradation is explored in Sec. 5.4.

#### **4.1 Detector Efficiency**

Detector photopeak efficiencies were obtained by combining PENELOPE [55, 56] simulations, described in detail below, with direct measurements of gamma rays from  $^{60}\text{Co}$  and  $^{24}\text{Na}$  sources and from  $^{27}\text{Al}(p, \gamma)$  resonance measurements. This process hinged on one absolute measurement (from the  $^{60}\text{Co}$  source) at a low gamma-ray energy (1332 keV) and then extended upward in energy with the use of relative measurements, relying on *branching ratios* only (i.e. the method was independent of source strength). Each relative measurement included a branch that was close in energy to a branch where the simulation had been previously verified, starting with the  $^{60}\text{Co}$  measurement at 1332 keV. Because the simulation geometry described below was slightly tuned to produce a detector efficiency that matched the results from the absolute  $^{60}\text{Co}$  measurement, these low-energy branches were set to the value given by PENELOPE in order to extract an efficiency at the higher energy branches.

##### *4.1.1 Direct measurements: $^{60}\text{Co}$ , $^{24}\text{Na}$ , $^{27}\text{Al}$*

The efficiency at 1332 keV was measured using the gamma ray from a 31.51-nCi  $^{60}\text{Co}$  source fabricated and calibrated in 2005 by Isotope Products [59] and corrected for decay. This calibration has a precision of 1.7% (99% C.L.), and the PENELOPE simulations were adjusted to match the efficiency of this source, as described in the following subsection. The ratio of efficiencies from 1369 to 2754 keV was measured using a  $^{24}\text{Na}$  source ( $t_{1/2} = 15$  hrs) fabricated at the University of Washington.

Since the simulated efficiency at 1332 keV equaled the measured  $^{60}\text{Co}$  efficiency and since 1369 keV is very close to 1332 keV, we equated the efficiency at 1369 keV to the PENELOPE value. Then from this ratio we obtained the efficiency at 2754 keV.

To extend the efficiency determination to higher energies, we measured  $^{27}\text{Al}(p, \gamma)$  resonances using a thick, full aluminum target and used the relative intensities of well-known gamma ray branches at  $E_p = 633$  and 992 [60, 61]. For the latter resonance, our coin target was also used. We subtracted the below-resonance yield from the above-resonance yield to extract the net yield. At  $E_p = 992$  keV, the gamma rays of interest are at 1779, 4742, and 10762 keV. Using the simulation to determine the efficiency at 1779 keV, our measurements, combined with the known branches, gave the efficiencies at the two higher energies. At  $E_p = 633$  keV, we measured the gamma rays at 7575 and 10451 keV. As the simulation matched the value we had obtained at 10762 keV, we used the simulation for the 10451 keV value and the known branch to determine the efficiency at 7575 keV. The agreement between measurement and simulation is discussed in the following subsection.

#### 4.1.2 PENELOPE Simulations

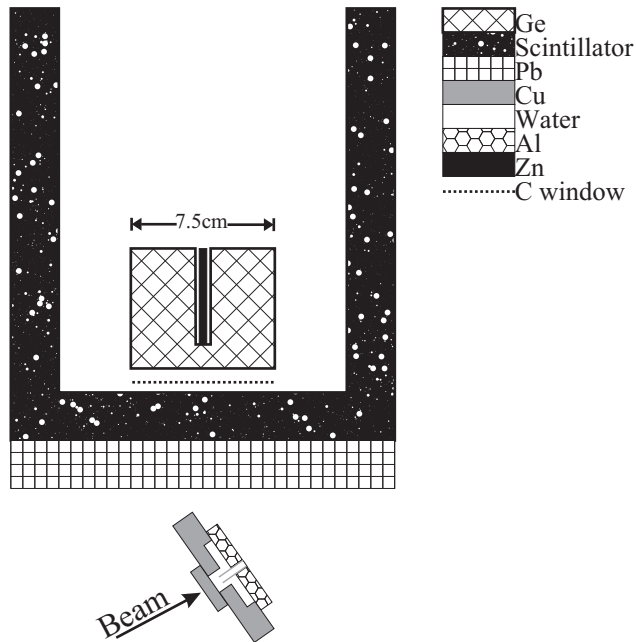


Figure 4.1: Cross section of simulated detector geometry. Zinc was used as a substitute for brass.

The geometry of our apparatus as modeled in PENELOPE is shown in Fig 4.1. The simulated detector included the germanium crystal, cold finger, and carbon window. All germanium detector dimensions were initially taken from the nominal specifications provided by Canberra [62]. In addition, we included the 26-mm lead and 25-mm planar plastic scintillator in front of the detector. Although the annular plastic scintillator was modeled, the annular lead was not, as it was not in the line of sight of the target. The sodium source was a uniform, 5-mm diameter disk centered on the copper substrate. The copper backing mount was included, as was the aluminum plate supporting the water cooling system. The water and its copper pipes inside the target mount were modeled, but the pipes that extended up and out from the mount were not, as they were thin and mostly out of the line of sight. All components of the target mount were aligned with the beam, whereas the detector was at an angle of 55°.

The gamma rays were projected from their source uniformly in a 80° opening angle, which covered all modeled components. Absolute efficiencies were corrected for the solid angle. Each simulated energy included an initial number of gamma rays such that the photopeak precision was less than 0.1%, and a sample spectrum is shown in Fig. 4.2.

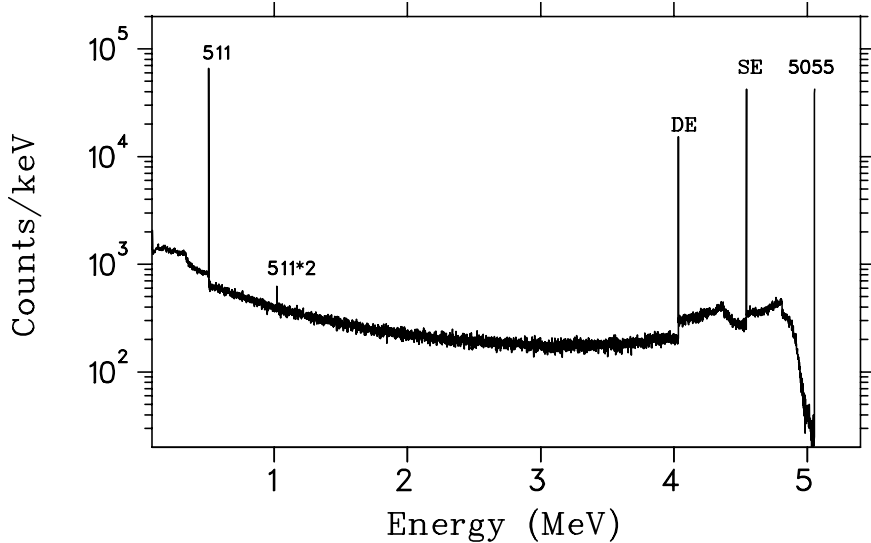


Figure 4.2: Sample PENELOPE spectrum for  $E_\gamma = 5055$  keV. Labels are in keV. SE and DE indicate single- and double-escape peaks, respectively.

At  $E_\gamma = 1332$  keV, with the source spread out over an area equal to that of the 1-mm diameter

$^{60}\text{Co}$  source, the simulation initially gave results 2.5% higher than the measurement. Therefore, the front face of the crystal was moved back from the target by 1.7 mm, in order to make the simulation reproduce the measurement exactly (back face location was unchanged). Results for the simulated detector efficiency are shown in the upper panel of Fig. 4.3. For sources other than the  $^{22}\text{Na}$ , source distribution and substrate material were changed in the simulation to match those used in the measurement. The bottom panel of Fig. 4.3 shows the ratio of the measured efficiencies to the simulations, and all values are shown in Table 4.1.2.

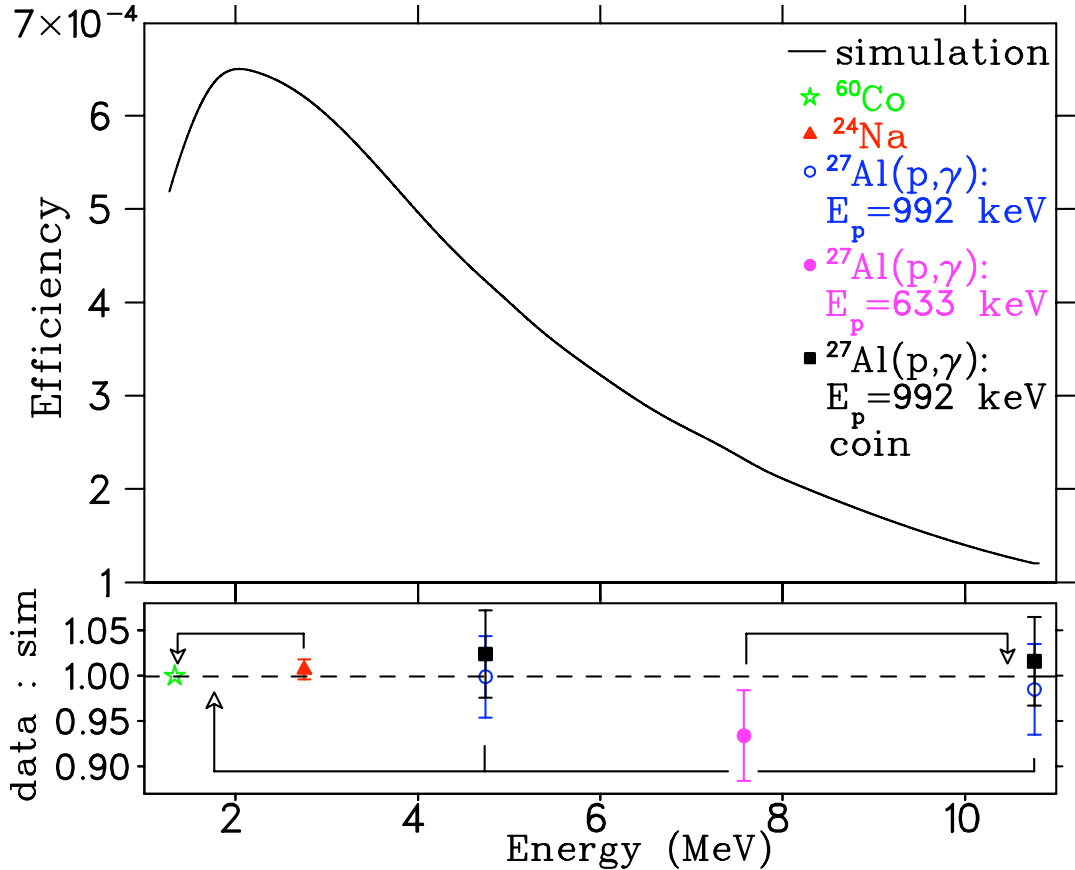


Figure 4.3: Photopeak efficiency. Top panel is the efficiency from Monte Carlo simulations. Bottom panel shows the ratio of efficiencies from measurement to simulation, and arrows indicate the gamma-ray energy used in the relative efficiency analysis. Values are shown in Table 4.1.2.

For the 213- and 610-keV resonances in  $^{22}\text{Na}(p, \gamma)$ , yields from first-escape peaks were added to the photopeak yield in order to improve statistics for branches with  $E_\gamma = 7333$  and 8162 keV,

Table 4.1: Numerical efficiency comparison. All values should be multiplied by  $\times 10^{-4}$ . Only statistical errors are shown, and an overall systematic error of 1.7% applies to the measured values. Statistical uncertainties from the simulation (“sim”) are less than 0.5%.

$E_\gamma$ (keV)	Substrate	sim <sup>a</sup>	$^{60}\text{Co}$	$^{24}\text{Na}$ <sup>b</sup>	$^{27}\text{Al}(p, \gamma): E_p =$	
					992 keV <sup>c</sup>	633 keV <sup>d</sup>
1332	Cu	5.36	5.36±0.03			
1369	Cu	5.49		—		
1779	Al	7.44			—	
1779	Cu	6.37			—	
2754	Cu	6.20		6.24±0.06		
4742	Al	4.77			4.78±0.21	
4742	Cu	4.23			4.34±0.20	
7575	Al	2.62				2.45±0.13
10451	Al	1.47				—
10762	Al	1.37			1.36±0.07	
10762	Cu	1.20			1.23±0.06	

<sup>a</sup> Geometry adjusted to match  $^{60}\text{Co}$  measurement as described in text.

<sup>b</sup> 1369-keV value obtained from simulation in order to obtain 2754-keV value from measured ratio.

<sup>c</sup> 1779-keV value obtained from simulation in order to obtain 4742- and 10762-keV values from measured ratios.

<sup>d</sup> 10451-keV value obtained from simulation in order to obtain 7575-keV value from measured ratio.

respectively. Comparison of  $^{27}\text{Al}(p, \gamma)$  data to simulation at 7.5 MeV indicates agreement to within 2% and is covered by the systematic error detailed in the next section.

#### 4.1.3 Systematic Errors for the Efficiency

In order to extract systematic errors for our efficiencies, we compared the quality of the fit of our data from the  $^{24}\text{Na}$  source and the 992- and 633-keV resonances of  $^{27}\text{Al}(p, \gamma)$  to our simulations, as shown in the bottom panel of Fig. 4.3. The precisely measured ratio for the two  $^{24}\text{Na}$  gamma rays yields a value for the efficiency at 2754 keV which is  $0.7 \pm 1.1\%$  higher than that given by the simulation. The points obtained from  $^{27}\text{Al}(p, \gamma)$  resonances have statistical uncertainties between 4.7 and 5.2%, and they agree well with the simulation. Therefore, we ascribe a 5% systematic uncertainty to the efficiency determination for isotropic emission of  $\gamma$  rays.

Because the detectors are centered at  $\pm 55^\circ$  in the laboratory, zeros of  $P_2(\cos \theta)$ , the effect of a  $P_2(\cos \theta)$  term in the angular distribution can only arise from the angular dependence of the efficiency across the detector and from center of mass to laboratory transformation. A  $P_4(\cos \theta)$  term has no such restriction. Assuming the angular distribution to be of the form  $\Omega(\theta) = 1 + a_2 P_2(\cos \theta) + a_4 P_4(\cos \theta)$ , we used the PENELOPE simulation to determine the effect of non-zero values of  $a_2$  and  $a_4$ . A value of  $a_2$  as large as 1 only caused a  $2.6 \pm 0.4\%$  change in the efficiency. Published data for  $^{23}\text{Na}(p, \gamma)$  resonances [63] show typical  $a_4$  values of about 0.005 and a maximum value of 0.05. An  $a_4$  of 0.05 would cause a  $2.0 \pm 0.4\%$  change in the efficiency. Therefore, we assigned an additional systematic error of 3%, to include the possible effects of the angular distribution. Our overall systematic error in the efficiency is  $\pm 6\%$ .

## 4.2 Initial Total Number of Target Atoms

We determined the initial number of target atoms from the 1275-keV gamma rays emitted in the decay of  $^{22}\text{Na}$  ( $t_{1/2} = 2.6027(10)$  yrs [49]) using the simulated detector efficiency and assigned a 2.6% uncertainty. This uncertainty combines the 1.7% uncertainty in the  $^{60}\text{Co}$  calibration source at  $E_\gamma = 1332$  keV with an additional 2% due to the accuracy of the  $\sim 7\%$  background subtraction in this region of high detector rate. Potential degradation of the total number of atoms due to proton bombardment is discussed in Sec. 5.4.

### 4.3 Beam Properties

#### 4.3.1 Normalized Beam Density

We conducted measurements on  $^{27}\text{Al}$  targets in order to extract the normalized beam density,  $\rho_b = \frac{dN_p}{dA}/(Q/e)$ , averaged over the 5-mm diameter area. Systematic errors were then explored with simulation and visual inspection of beam-related target coloration. Beam non-uniformity was then taken into account, and its effect combined with the possibility of a non-uniform target was investigated.

We determined the normalized beam density,  $\rho_b$ , averaged over the target by comparing the thick-target yield from our “coin” target,  $Y_c$ , which had the same areal extent as the  $^{22}\text{Na}$  targets, to the yield from a solid  $^{27}\text{Al}$  target,  $Y_s$ . From the ratio of these yields, one can extract  $\rho_b$  via:

$$\frac{Y_c}{Y_s} = \rho_b A_c, \quad (4.1)$$

where  $A_c$  is the area of the coin. The yields were measured at different times with different beam tunes using the resonances at  $E_p = 406$  and  $992$  keV, which yielded results for  $\rho_b$  of  $2.60 \pm 0.09 \text{ cm}^{-2}$  and  $2.55 \pm 0.10 \text{ cm}^{-2}$ , respectively, with statistical errors only. The weighted average of these two measurements,  $2.58 \text{ cm}^{-2}$ , was chosen for  $\rho_b$ .

To study the distribution of beam across the target in order to quantify systematic errors, we carried out a number of measurements using a large raster with  $1.8 \times$  the standard amplitude, in addition to the standard amplitude of  $\sim 6 \text{ mm} \times \sim 7 \text{ mm}$ , on the main  $^{22}\text{Na}$  targets and the solid  $^{27}\text{Al}$  and coin targets. With the raster on and off, transmission measurements through various collimators, shown in Fig. 3.2, were performed as well. We determined the ratio of normalized beam densities with the two raster settings to be  $0.70 \pm 0.02$  (statistical error only). Because of the restrictions of the collimators on beam transmission, this ratio should be larger than the squared ratio of raster amplitudes, and if both raster conditions swept the beam far across the collimators, the ratio would be 1.0. As shown in Fig. 3.2, our collimator arrangement consisted of a sliding collimator (in position #1) upstream of 8- and 10-mm fixed collimators. We monitored the transmission through the fixed collimators while running with the standard 8-mm collimator in position #1, and made a number of measurements through a 7-mm collimator in position #1 with the raster on, as well as measuring the transmission of the non-rastered beam through the 1-mm and 3-mm tuning collimators in position #1. These measurements, along with the relative yields of large to standard raster, were used to con-

strain a Monte Carlo simulation that was used to investigate potential beam densities on the target. It also was used to test the effects of possible beam drift, misalignment of the beam and target, and target non-uniformities.

The simulation modeled transport of the beam through the final components of the beamline and chamber, including the final quadrupole, the rastering unit, and the three sets of collimators. Variable parameters included beam width and offset, possible collimator offset, raster amplitude, and beam distribution at the quadrupole. A normalized beam density could not be uniquely determined by this method alone, but the densities within an acceptable phase space, defined by reasonable agreement for transmissions and large/standard rastering yield ratios, ranged from  $2.33$  to  $2.83 \text{ cm}^{-2}$ . We adopted  $\pm 0.25 \text{ cm}^{-2}$  as the systematic uncertainty in the normalized beam density.

For one set of parameters in this acceptable phase space that illustrates an extreme case, the beam was assumed to fill the 5-cm diameter quadrupole aperture uniformly before focusing 19 cm downstream to a  $\sim 1.5\text{-mm}$  diameter spot at collimator 1, shown in Fig. 3.2. This caused beam non-uniformity over the target. In this case, the normalized beam density averaged over a 5-mm diameter uniform target area was  $2.55 \text{ cm}^{-2}$ , whereas averaging over a 2.5-mm diameter the density was 15% higher. This is only a problem if the target also had non-uniformities. Although we believe the targets were quite uniform, as outlined in Sec. 3.4.1, we produced a calculation for an extreme case where the target distribution was conical. This hypothetical target distortion was modeled along with the beam distribution described above, and the product of the target and the beam deviated from its nominal value by 12%, only slightly larger than the adopted systematic uncertainty in the beam density. A less radical distribution is a cone added to a cylinder, where the height of the cone and the height of the cylinder are equal. The deviation in this case was less than 3%. This distribution was also shifted off-axis by 1.5 mm to test sensitivity to alignment, and the deviation was no more than 6%. In summary, we experimented with variations larger than those expected for our system and found yields well within our uncertainties.

We also visually inspected the pattern left on the target after irradiation, as a rudimentary check of the beam area. Although the target was protected by a copper shroud cooled by liquid nitrogen, a faint coloration on the target from beam exposure could be observed. Tests were also run without using the cold trap, where, instead of a coloration, a dark and clear spot due to carbon cracking could be observed. The area of the mark from the large raster was measured by superimposing a

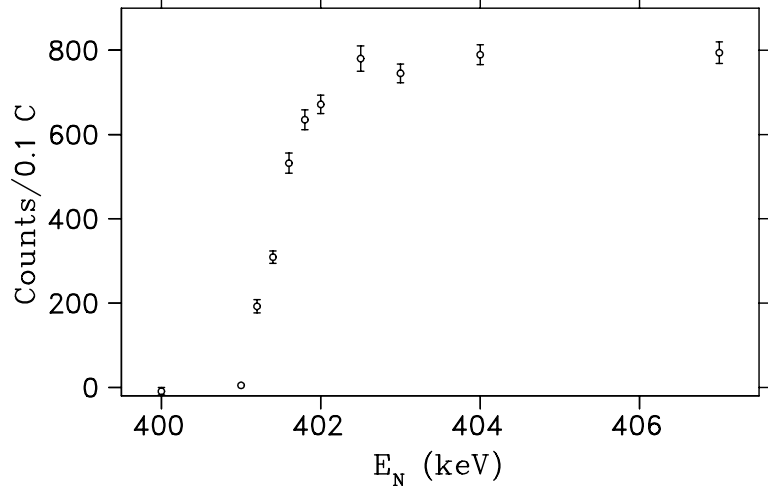


Figure 4.4:  $^{27}\text{Al}(p, \gamma)$  excitation function from a thick aluminum target.  $E_N$  is the nominal accelerator energy.

millimeter spaced, gridded transparency over the target. If we take the inverse of this area to be the normalized density for the large raster, we can obtain the normalized density for the standard raster using our measured ratio of large to small raster yield. This scheme is expected to underestimate the normalized beam density, because of probable non-uniformity at the edges of the mark. The value for the normalized beam density was found by this method to be  $2.28$  and  $2.38 \text{ cm}^{-2}$  for two targets. These values are not markedly smaller than our adopted value of  $2.58 \pm 0.25 \text{ cm}^{-2}$ .

#### 4.3.2 Beam Energy Calibration with $^{27}\text{Al}(p, \gamma)$

The beam energy was determined using a  $90^\circ$  analyzing magnet with an NMR field monitor, where the nominal accelerator energy,  $E_N$ , is proportional to the square of the NMR frequency. If the direction of an energy sweep of a resonance changed, the current of the analyzing magnet was cycled at least two times in order to erase any hysteresis effects. In order to calibrate the energy of our beam, we took multiple measurements of each  $^{27}\text{Al}(p, \gamma)$  reaction with a solid  $^{27}\text{Al}$  target at well-known resonance energies [64]. A sample thick-target excitation function is shown in Fig. 4.4.

Energy steps of 200 eV were taken, two passes were performed across each resonance, and the final curves were combined. The resonant beam energy was extracted from the excitation function

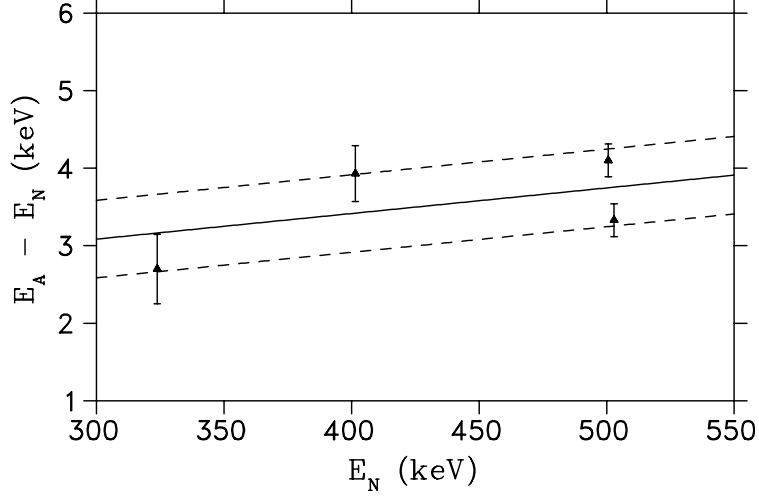


Figure 4.5: Beam-energy calibration.  $E_N$  is the nominal accelerator energy, and  $E_A$  is the accepted resonance energy. The solid line is the fit, and the dashed lines indicate the overall calibration uncertainty taken to be  $\pm 0.5$  keV.

where the yield was half of its maximum value. The results are shown in Fig. 4.5 for resonances at  $E_p = 326.6, 405.5, 504.9$ , and  $506.4$  keV. The differences between the nominal beam energy and the accepted resonance energies were fit to a linear equation with slope  $m = 3.3 \times 10^{-3}$  and offset  $b = 2.1$  keV (Fig. 4.5), and the resulting coefficients were used to adjust the beam energy for all data. Given the spread in the difference between nominal accelerator energy and accepted energy, we assign a  $\pm 0.5$  keV uncertainty to our knowledge of the beam energy.

## Chapter 5

### **$^{22}\text{Na}(\text{p},\gamma)$ MEASUREMENTS AND ANALYSIS**

Measurements were taken on previously known  $^{22}\text{Na}(p,\gamma)$  resonances, which we find at  $E_p = 213, 288, 454$ , and  $610$  keV. We also explored the proposed resonances at  $198, 209$ , and  $232$  keV. A summary of the gamma rays from each resonance is shown in Table 5.1, and the relevant energy level diagram for  $^{23}\text{Mg}$  was shown in Fig. 2.11.

Table 5.1: Summary of gamma rays for each explored resonance, labeled by  $E_p$ , and their corresponding branches. All energies are in keV.

198	209	213	232	288	454	610
5055 (58%)	5067 (66%)	7333 (89%)	7801 (66%)	5141 (67%)	5300 (52%)	8162 (61%)
2317 (42%)	5729 (33%)	5732 (11%)	7350 (30%)	5803 (26%)	5963 (44%)	7711 (19%)
			5749 (4%)	7404 (7%)	7565 (4%)	6112 (20%)

For all measurements, a scan was performed across a range of  $\sim 25$  keV around the resonance energy. To subtract background, which was comprised mostly of cosmic rays and Compton events, we assumed it to have a localized linear dependence on gamma-ray energy and fit the background to windows in the spectrum above and below the line of interest. This method took the amplitude of the spectrum on either side of the gamma ray of interest and analytically determined the parameters,  $m$  and  $b$ , for a straight line under the peak, such that:

$$\int_{c_1}^{c_2} (mx + b) dx = N_{c_{12}} \quad \text{and} \quad \int_{c_3}^{c_4} (mx + b) dx = N_{c_{34}}, \quad (5.1)$$

where  $N_{c_{12}}$  and  $N_{c_{34}}$  are the sums of the counts between windows bound by channels  $c_1$  to  $c_2$  and  $c_3$  to  $c_4$ , respectively, on either side of the peak. Thus, the number of background subtracted counts is the integral under the determined straight line with bounds equal to the main energy window. This method was especially important for resonances with characteristic gamma rays below 6 MeV. Here contributions from 6129-keV incident photons due to the contaminating  $^{19}\text{F}(p, \alpha\gamma)^{16}\text{O}$  reaction were

significant. Affected resonances included  $E_p = 454, 288$  keV, and one branch from  $E_p = 610$  keV, but the rate of the contaminating gamma ray decreased rapidly with proton energy. An example of this method applied to a gamma ray peak is shown in the inset of Fig. 5.2 (a).

In order to extract the yield at each laboratory proton energy,  $E_p$ , an energy window was set on the gamma ray of interest in the vetoed singles spectrum for each of the two germanium detectors. This window was  $\sim 25$  keV for one detector and  $\sim 40$  keV for the other. For each detector, the sum of the background subtracted counts in the window is  $N_i = N_R \eta_i L_i$ , where  $N_R$  is the total number of gamma rays produced in the  $(p, \gamma)$  reaction,  $\eta_i$  is the efficiency, and  $L_i$  is the live time fraction for detector  $i$ . The yield is

$$Y = \frac{N_R}{Q/e} = \frac{N_1/L_1 + N_2/L_2}{\eta Q/e}, \quad (5.2)$$

where  $\eta = \eta_1 + \eta_2$ . The effects of angular distributions have been addressed in Sec. 4.1.3.

In order to test the sensitivity of our results to the inputs for the gamma-ray background subtraction and its linearity, resonances at  $E_p = 610$  keV (with  $E_\gamma = 8162$  keV) and 454 keV (with  $E_\gamma = 5300$  keV) were inspected, and the choice of window for both the peak and the background on each side was varied within reasonable limits, such as widening, shortening (no window smaller than 10 keV), and shifting. The resonance strengths changed by less than 1%, indicating that systematic errors associated with background subtraction are negligible.

After the yields for each excitation function were determined, the areas under the excitation curve were obtained by using the trapezoidal method. This value for  $\int Y_i dE$  was then used in Eq. 1.4, along with values determined for all other parameters, to extract the partial resonance strength,  $\omega \gamma_i$ , for each branch  $i$ . The total strength is simply equal to the sum of the partial strengths for all branches.

### 5.1 Absolute yields: $E_p = 610, 454, 288, 213$ keV

Fig. 5.1 shows the data taken on the two strongest resonances at  $E_p = 454$  and 610 keV. These resonances were revisited after various amounts of accumulated charge to monitor possible target degradation, discussed in detail in Sec. 5.4. Fig. 5.2 shows the corresponding gamma-ray spectra summed over all runs, including an inset illustrating the background subtraction method. All data for resonances at  $E_p = 213, 288$ , and 610 keV were taken on target #4, and the 454-keV resonance

was measured on both targets #3 and #4. Fig. 5.3 illustrates the summed raster plots for target #3 with  $E_p = 454$  keV. The concentration of counts around the center of the plot come from  $^{22}\text{Na}(p, \gamma)$  while a few counts spread through the plot are consistent with yield from  $^{19}\text{F}$  contamination.

Fig. 5.4 shows the data taken for 288- and 213-keV resonances, and Fig. 5.5 illustrates the summed gamma-ray spectra for each resonance respectively. Characteristic gamma rays for each are clearly distinguishable above background. For  $E_p = 213$  keV, the integrated yield was determined with the same trapezoidal method as above, plus a small correction because the highest energy point did not reach zero yield. The details of determining this contribution are discussed in Sec. 5.3, after a prerequisite analysis method is outlined in the following subsection.

## 5.2 Upper limits for yield: $E_R = 232, 198, 209$ keV

Data in the region of the proposed resonances at  $E_p = 198$  and 232 keV are shown in Fig. 5.6. In the summed gamma-ray spectra shown in Fig. 5.7, no discernible gamma-ray yields can be detected above background. All data for  $E_p = 198$  keV were taken on the chromium-covered target #3. Data for  $E_p = 232$  keV were taken on one of the bare test targets, which had previously been exposed to an integrated charge of 13 C.

For these resonances, the shape of the excitation function used to determine the area was adopted from either the resonance at  $E_p = 454$  or 610 keV, depending on the target. Because the resonance shape was dominated by the implantation distribution, this shape was normalized, shifted, and stretched so that it could be fit to the data of the resonance in question. The stretch factor was fixed and set equal to the ratio of stopping powers in copper for the two energies, whereas the energy shift and the normalization factor were allowed to vary. The central value of the shift was given by the differences in resonance energies, and the range of the shift was given to fully span the data points. If a data point for the low-energy resonance fell between points of the normalized curve, the corresponding reference point was determined by a linear interpolation. For each pair of shift and normalization, the value of the  $\chi^2(\omega\gamma_i, E_i)$  between each low-energy resonance and the normalized reference resonance was calculated, and plots for each resonance are shown in Fig. 5.8 and 5.9 (left sides). The modified reference excitation function corresponding to the minimum value of  $\chi^2$  is shown for each resonance in Fig. 5.6 (open circles).

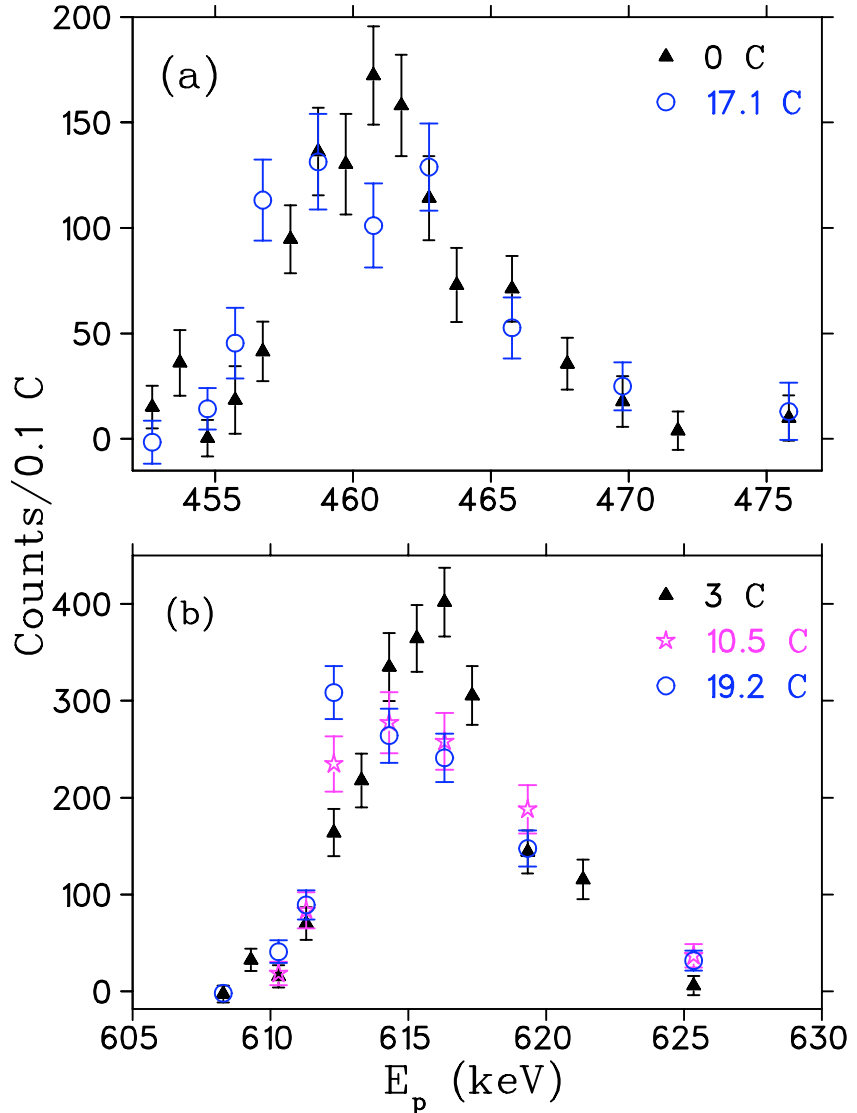


Figure 5.1: Excitation functions for (a)  $E_p = 454$  keV and (b)  $E_p = 610$  keV.  $E_p$  is the lab proton energy. Each plot shows the excitation function at the beginning of target bombardment and at the end, after  $\sim 20$  C had been deposited. An intermediate curve after 10.5 C is also shown in (b). (a) is gated on  $E_\gamma = 5300$  and 5963 keV, and (b) is gated on the photopeak and single-escape peak of  $E_\gamma = 8162$  keV.

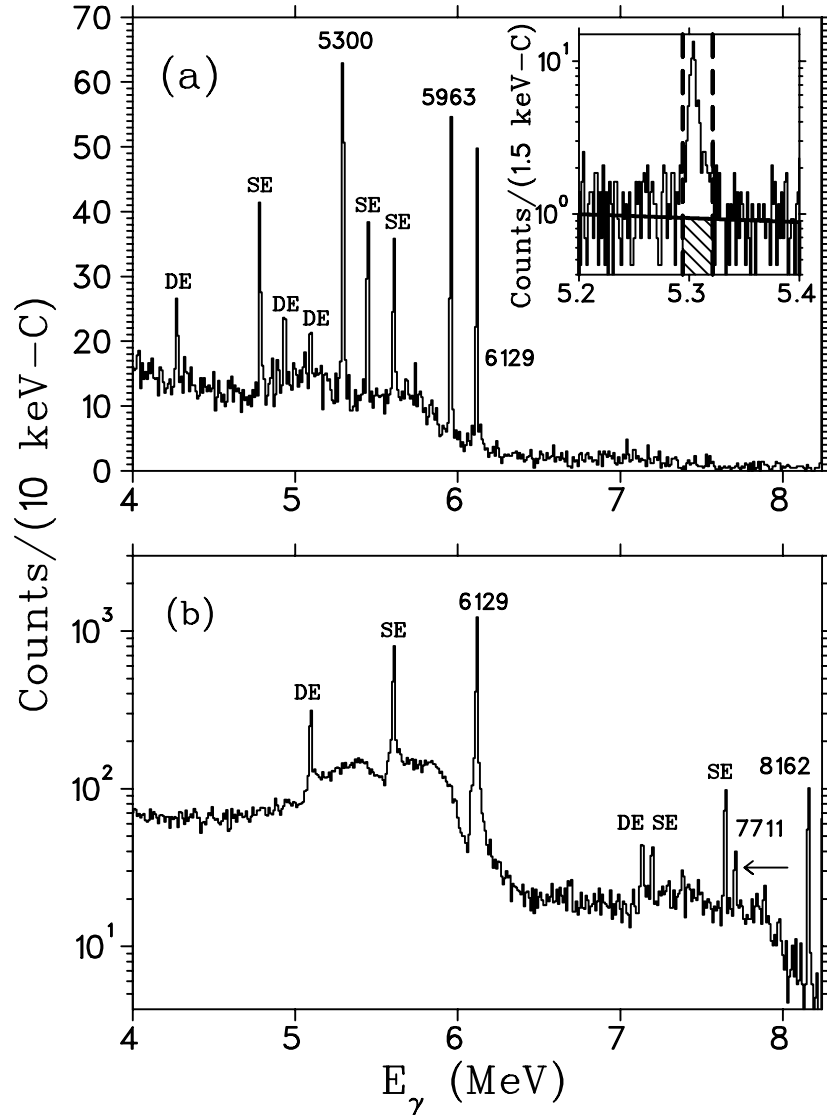


Figure 5.2: Summed gamma-ray spectra for (a)  $E_p = 454$  keV and (b)  $E_p = 610$  keV. The inset illustrates the beam-background subtraction method for  $E_\gamma = 5300$  keV, including gamma-ray gate (dashed), analytically calculated background line (solid), and subtracted region (hatched). SE and DE indicate single- and double-escape peaks, respectively.

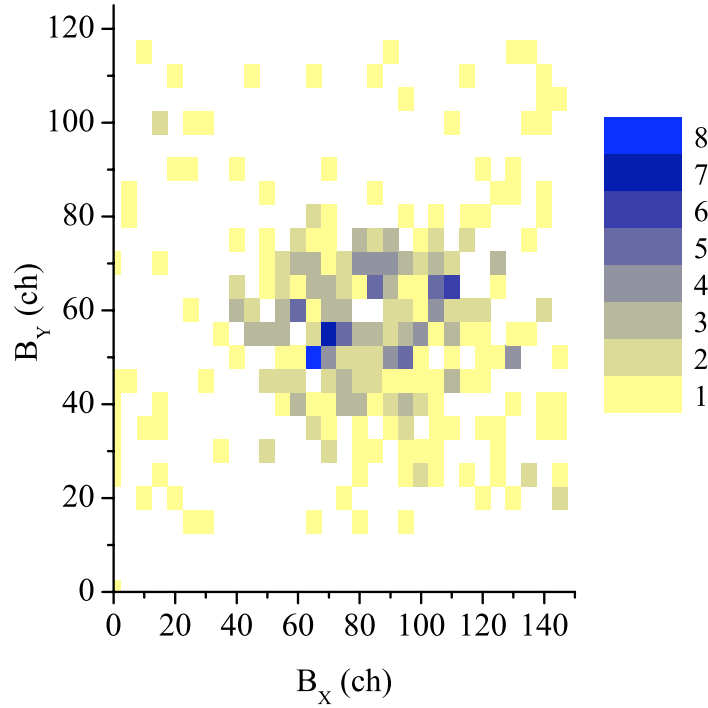


Figure 5.3: Raster plot for the sum of  $^{22}\text{Na}(p, \gamma)$  for  $E_p = 454$  keV, target #3, with raster amplitudes 1.8× larger than our standard amplitudes. The plot is gated on  $E_\gamma = 5300$  keV. Outside the target area there are a few bins with only 1 count, which is consistent with the known level of  $^{19}\text{F}$  contamination from the Compton continuum from  $E_\gamma = 6129$  keV.

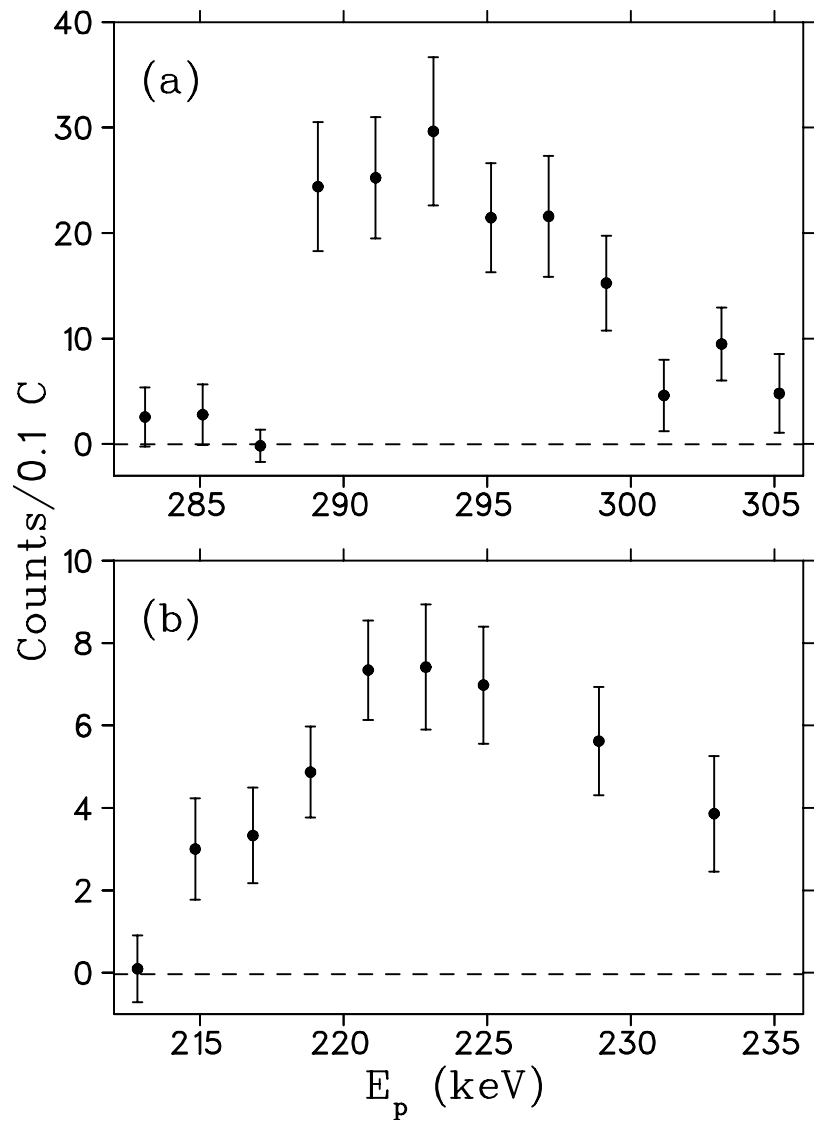


Figure 5.4: Excitation functions for (a)  $E_p = 288$  keV and (b)  $E_p = 213$  keV.  $E_p$  is the lab proton energy. (a) is gated on  $E_\gamma = 5141$  keV, and (b) is gated on the photopeak and single-escape peak of  $E_\gamma = 7333$  keV.

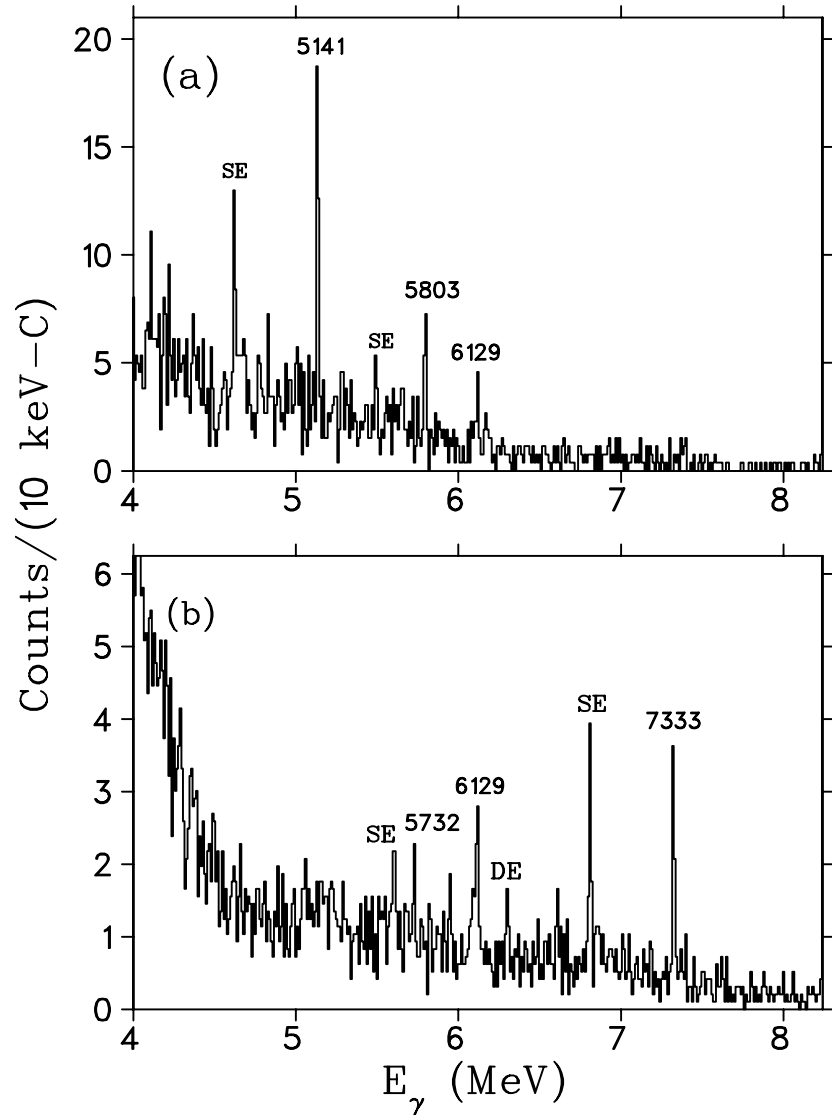


Figure 5.5: Summed gamma-ray spectra for (a)  $E_p = 288 \text{ keV}$  and (b)  $E_p = 213 \text{ keV}$ . SE and DE indicate single- and double-escape peaks, respectively.

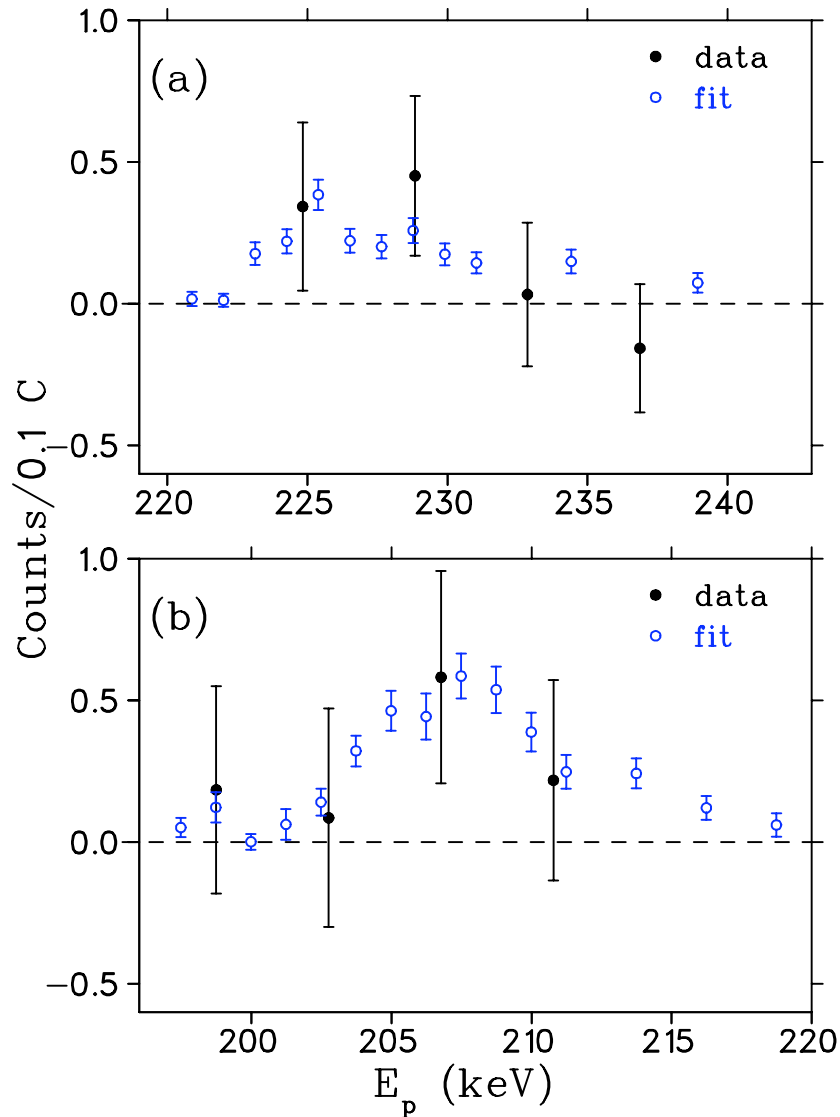


Figure 5.6: Solid circles are excitation functions for (a)  $E_p = 232$  keV and (b)  $E_p = 198$  keV (total  $\chi^2$  above zero is 3.1).  $E_p$  is the lab proton energy. (a) is gated on  $E_\gamma = 5055$  keV, and (b) is gated on the sum of  $E_\gamma = 7801$  and 7350 keV. Open circles are the normalized, stretched, and shifted  $E_p = 454$  keV excitation function fit, described in the text. This reference excitation function is not as smooth in (a) as in (b) due to degradation of the bare target.

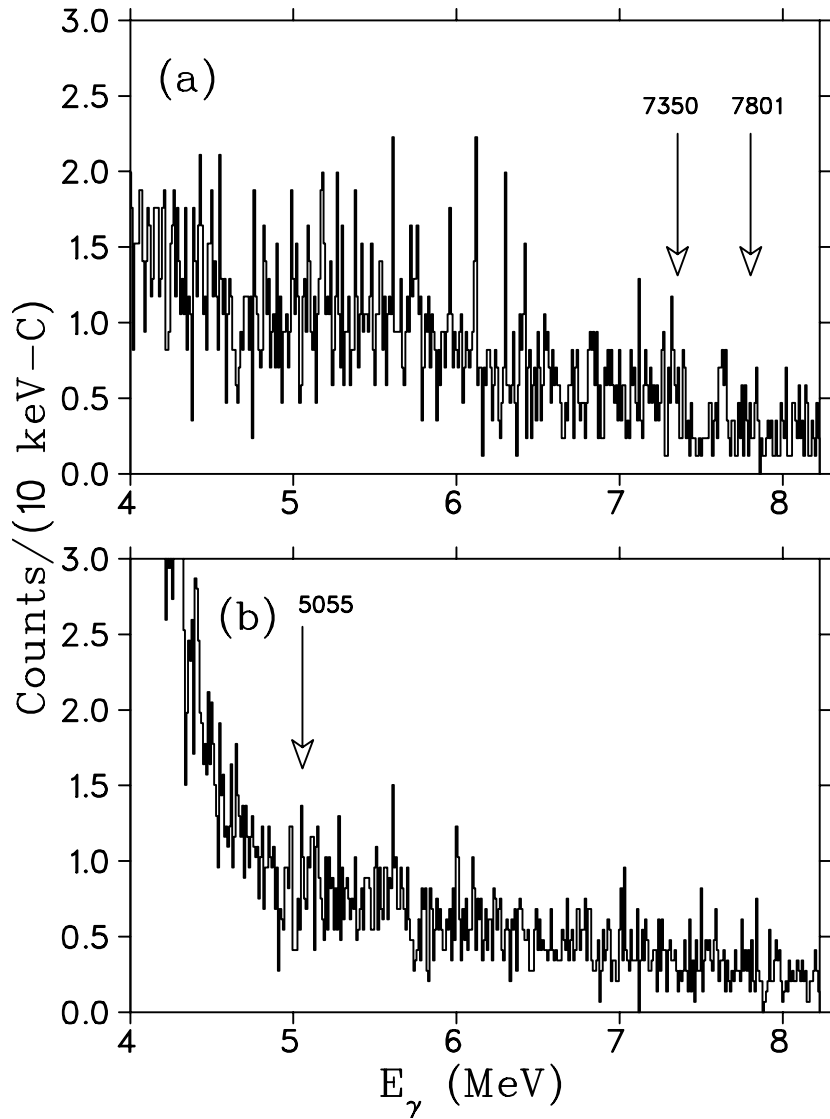


Figure 5.7: Summed gamma-ray spectra for (a)  $E_p = 232 \text{ keV}$  and (b)  $E_p = 198 \text{ keV}$ . The target activity was  $2.3\times$  higher in (b) than in (a) and is responsible for the increased background at low energies. Arrows indicate the energy where one would expect to see gamma rays from the relevant transition.

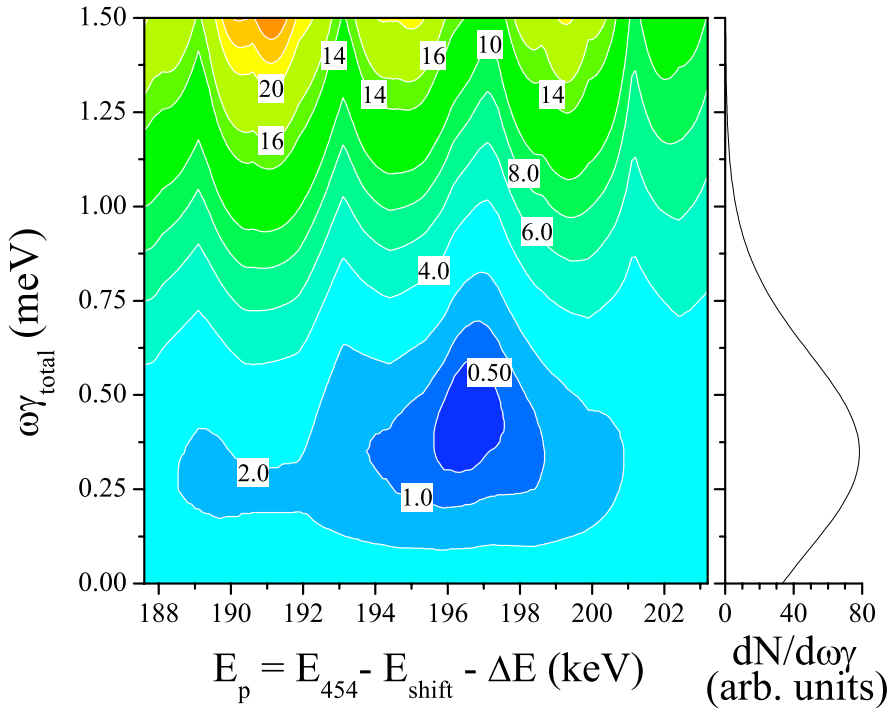


Figure 5.8: The left side is the contour plot of total  $\chi^2(\omega\gamma_i, E_i)$  for  $E_p = 198$  keV.  $E_{454}$  is the reference resonance energy,  $E_{\text{shift}}$  is the amount the reference resonance was shifted, and  $\Delta E$  is the difference in energy loss at  $E_p = 454$  and 198 keV due to the chromium layer ( $\sim 1.5$  keV). The minimum value of total  $\chi^2(\omega\gamma_i, E_i)$  is 0.2 with 2 degrees of freedom, which has a probability of 0.91. The value of  $\chi^2$  above zero for the data is 3.1 in Fig. 5.6 (b). The right side is the projection of  $\exp(-\chi^2(\omega\gamma_i, E_i)/2)$  onto the  $\omega\gamma$ -axis and represents the probability density function used in Sec. 7.1.

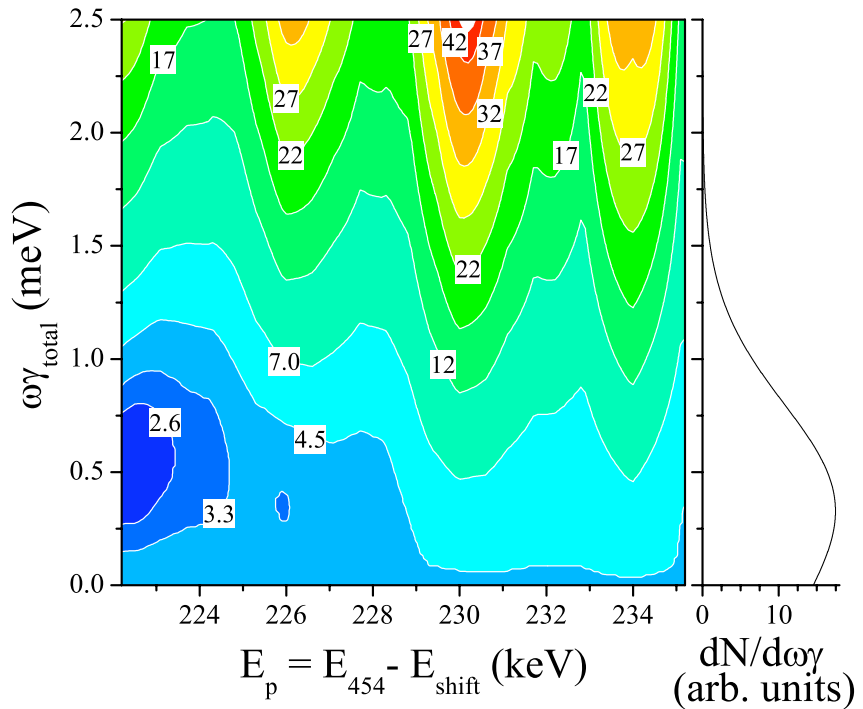


Figure 5.9: The left side is the contour plot of total  $\chi^2(\omega\gamma_i, E_i)$  for  $E_p = 232$  keV.  $E_{454}$  is the reference resonance energy,  $E_{\text{shift}}$  is the value the reference resonance was shifted, and  $\Delta E$  is zero because this target had no chromium layer. The minimum value of total  $\chi^2(\omega\gamma_i, E_i)$  is 2.1 with 2 degrees of freedom, which has a probability of 0.36. The right side is the projection of  $\exp(-\chi^2(\omega\gamma_i, E_i)/2)$  onto the  $\omega\gamma$ -axis and represents the probability density function used in Sec. 7.1.

The array of probabilities,  $P(\omega\gamma_i, E_i)$ , was taken to be proportional to  $\exp(-\chi^2(\omega\gamma_i, E_i)/2)$ , where  $\chi^2(\omega\gamma_i, E_i)$  is the  $\chi^2$  between the model, assuming particular values of  $\omega\gamma_i$  and  $E_i$ , and the data. Because we are mainly interested in constraining the value of  $\omega\gamma$ , we projected the two-dimensional arrays onto the  $\omega\gamma$ -axis (i.e.  $P(\omega\gamma_i) = \sum_{E_i} P(\omega\gamma_i, E_i)$ ), shown in Fig. 5.8 and 5.9 (right sides). The upper limits on  $\omega\gamma$  were extracted with a particular confidence level,  $C.L.$ , using the likelihoods:

$$C.L. = \frac{\sum_{\omega\gamma_i=0}^{\omega\gamma} P(\omega\gamma_i)}{\sum_{\omega\gamma_i=0}^{\infty} P(\omega\gamma_i)}. \quad (5.3)$$

The sum in the denominator was cut off at a maximum value of  $\omega\gamma$  such that the sum changed by less than 1%. Results are given in Chapter 6.

For the possible resonance at 198 keV, a finite value for the strength was also calculated. Instead of summing from zero and extending upward in the numerator of Eq. 5.3, the pair of  $\omega\gamma_i$  values with equal values of  $P(\omega\gamma_i)$  were determined such that the sum between them, properly normalized, gave the desired confidence level.

For the possible resonance at 232 keV, data for the third possible gamma-ray for  $E_p = 232$  keV at  $E_\gamma = 5749$  keV was not added to our yield because of its small branch; however, branches from the two other gamma rays (96.4%) were used to adjust the total resonance strength.

For the proposed resonance at  $E_p = 209$  keV, we also applied this method to a hybrid data set comprised of data points from  $E_p = 198$  and  $E_p = 213$  keV for the gamma ray at 5067 keV, assuming the branch given by Jenkins *et al.* [1] and using the excitation function from the dominant branch of  $E_p = 213$  keV and its first-escape peak as the reference curve, shown in Fig. 5.10. Because the data from the resonance at 198 keV was from a different target, its yields were scaled by the ratio of measured target activities. The shift in energy was allowed to vary from zero to 25 keV, and the fit yielding the minimum  $\chi^2(\omega\gamma_i, E_i)$  was found at the position of the 198-keV data points, possibly due to the fact that the gamma rays have overlapping energy windows. In other words, we did not observe a separate resonance at  $E_p = 209$  keV. An upper limit for this resonance, which is presented in Chapter 6, was extracted by restricting the energy shift to be equal to the difference in resonance

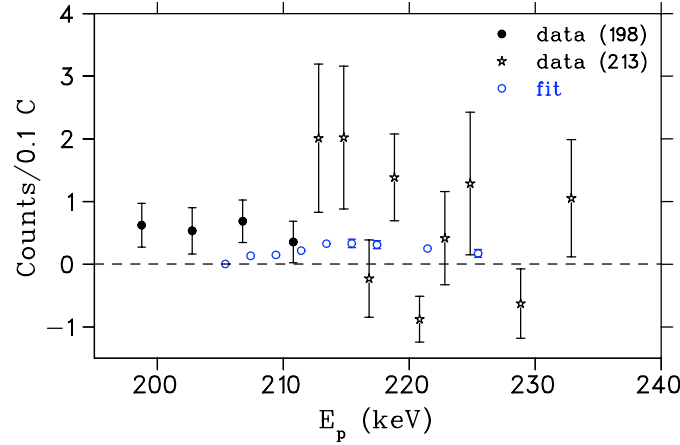


Figure 5.10: Solid circles represent the excitation function for  $E_p = 209$  keV, gated on  $E_\gamma = 5067$  keV.  $E_p$  is the lab proton energy. Open circles are the normalized, stretched, and shifted  $E_p = 213$  keV excitation function fit, described in the text. The first four data points on the left were taken from the 198-keV resonance measurement on target #3, and the rest are taken from the 213-keV resonance measurement on target #4.

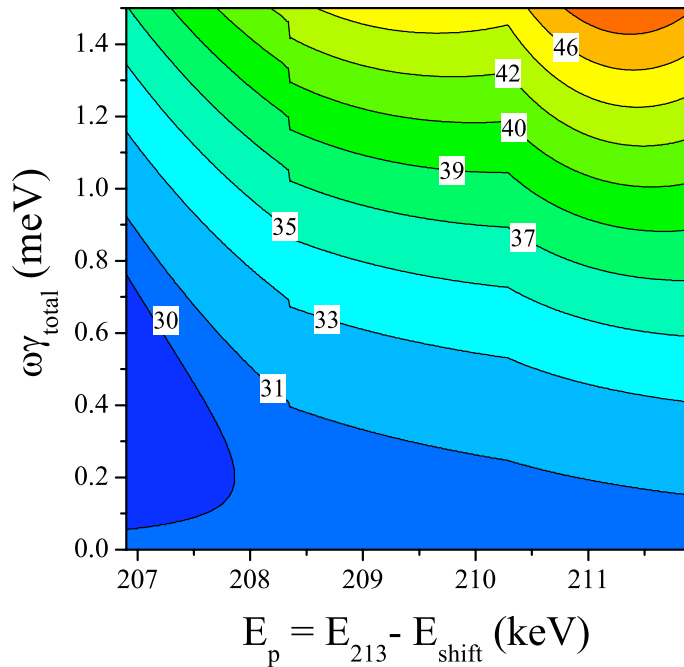


Figure 5.11: Contour plot of total  $\chi^2(\omega\gamma_i, E_i)$  for  $E_p = 209$  keV.  $E_{213}$  is the reference resonance energy, and  $E_{shift}$  is the value the reference resonance was shifted. The minimum value of total  $\chi^2(\omega\gamma_i, E_i)$  is 29 with 13 degrees of freedom, which has a probability of 0.002.

energies, spanning the range of  $\pm 2\sigma$  around the value claimed by Jenkins *et al* [1]. The  $\chi^2(\omega\gamma_i, E_i)$  contour plot is shown in Fig. 5.11.

This analysis technique of normalizing and shifting a reference resonance to obtain strengths of others was validated by applying it to the 288-keV resonance, for which the ratio of the strength calculated from this method to the direct method was  $0.95 \pm 0.12$ .

### **5.3 Corrected area for $E_R = 213$ keV**

In order to estimate the full area of the  $E_p = 213$  keV excitation function, a reference resonance at  $E_p = 454$  and three at 610 keV were utilized in the same manner outlined above. Each of the four curves were fit to the data, and each yielded a data point beyond the fixed  $E_p = 213$  keV excitation function that did reach zero. The last trapezoid area was calculated for each, and the average was added to the area from the direct data, equaling  $10 \pm 5\%$  of the total area. The uncertainty in the additional area was set to be the standard deviation among the four fits.

### **5.4 Degradation in the Total Number of Target Atoms**

Measuring the activity *in-situ* was not sufficient to determine the total number of target atoms throughout the measurement. During target bombardment, some fraction of  $^{22}\text{Na}$  was sputtered out of the illuminated area of the substrate, yet it remained nearby, maintaining an approximately constant activity throughout the duration of the resonance measurements. Thus, in addition to determining the total number of initial atoms, monitoring possible target degradation throughout bombardment was particularly important. In order to deduce the amount of degradation, two complementary methods were utilized. One method was to revisit a strong reference resonance periodically throughout the bombardment cycle. We define  $A(Q)$  as the integral of the reference excitation function,  $\int YdE$ , after an amount of charge,  $Q$  has been deposited.  $A(Q)$  is directly proportional to the number of target atoms,  $N_T(Q)$ , as shown in Eq. 1.4. The ratio of the integrals of the excitation function before and after bombardment,  $A(Q)/A(Q \sim 0)$ , is therefore equal to  $N_T(Q)/N_T(Q \sim 0)$ . The second method, which will be described in detail later in this section, was to measure the residual  $^{22}\text{Na}$  in the chamber before and after target bombardment and use this information to infer the number of sputtered target atoms. The results of each method are illustrated in Fig. 5.12, along with

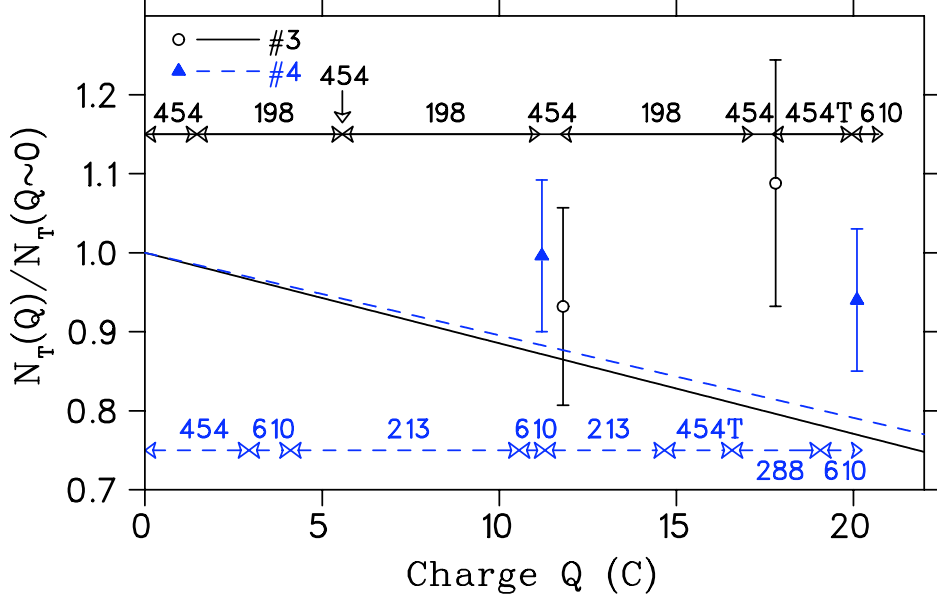


Figure 5.12: Target degradation as a function of implanted charge for main targets #3 and #4.  $N_T(Q)$  is the total number of atoms present in the substrate after an irradiation of charge,  $Q$ . The data points illustrate the ratio of the area of each reference excitation function to its initial area at the start of target bombardment. The lines represent a possible linear decrease of the number of atoms deduced from two residual activity measurements at the beginning and end of bombardment. Also shown is the timeline for each resonance measurement. The two sections marked “454T” indicate variable raster amplitude tests, and although these data are included in the branching ratio determination, they are not included in determining resonance strengths.

a timeline for each resonance measurement as a function of accumulated charge.

Target #3 accumulated 20.7 C in 186.0 hours, and target #4 accumulated 20.1 C of charge in 138.3 hours. Because we covered these targets with 20 nm of chromium, they remained fairly stable. Shown in Fig. 5.1 (a) are the first and last resonance scans at  $E_p = 454$  keV for target #3. Throughout the 20.7 C of bombardment, the resonance at  $E_p = 454$  keV was revisited four times.  $A(Q \sim 20 \text{ C})/A(Q \sim 0)$ , shown in Fig. 5.12, is  $1.07 \pm 0.12$ , consistent with no target loss. For target #4 on which all other non-zero strength resonances were measured, the monitoring resonance was  $E_p = 610$  keV, and multiple scans of its excitation function are shown in Fig. 5.1 (b). No appreciable sodium was lost up to at least 10.5 C. At the end of bombardment,  $A(Q \sim 20 \text{ C})/A(C \sim 0) = 0.94 \pm 0.09$  and is also consistent with no target loss.

To use the residual activity method, measurements of the 1275-keV rate were taken before target

installation ( $R_0^i$ ), after target installation and before bombardment ( $R_T^i$ ), after bombardment ( $R_T^f$ ), and after target removal ( $R_0^f$ ). The quantity  $(R_T^i - R_0^i) - (R_T^f - R_0^f)$  then is proportional to the amount sputtered from the target. This final value was used to estimate target degradation throughout the bombardment, assuming linear loss, and is also shown in Fig. 5.12 for each target. As we learned with our  $^{23}\text{Na}$  tests [18], this loss is in fact not linear but usually begins to occur after a significant amount of charge has been deposited, removing the protective layer and sputtering away some of the substrate. We nevertheless used a hypothesis of linear degradation of the target for one extreme and an amount consistent with no loss for the other for most uncertainties.

The 198- and 213-keV resonance measurements were taken over an extended period of time and charge, whereas all others were measured with a few Coulombs of integrated beam current and did not experience possible prolonged degradation. The 198- and 213-keV data were taken over  $\sim 15$  and 10 C, respectively, with short interruptions to measure a reference resonance excitation function. At the halfway point for each, the linear-decrease hypothesis indicated a 4-5% loss, although excitation function areas were consistent with no loss at that point. Therefore, we choose no loss with errors that span the values from each method,  $N_T(Q)/N_T(Q \sim 0) = 1.00_{-0.05}^{+0.00}$ . Combining this with the systematic uncertainty in the initial number of atoms, we have an overall systematic error of +2.6% and -5.6% in the total number of atoms for the 198- and 213-keV resonance strengths. For the 454- and 610-keV resonances, which were each measured at the beginning of target bombardment, only an overall systematic error of  $\pm 2.6\%$  was needed (see Sec. 4.2).

The 288-keV resonance was a special case, as its data were not from an extended measurement but were taken after 18 C of irradiation. Directly following the measurement of this resonance, we performed the final scan of the 610-keV reference resonance, which allowed insight into how many atoms remained. Therefore, the total number of atoms present for the 288-keV measurement was taken to be the average between linear target loss and loss indicated from the depleted area of the 610-keV resonance curve,  $N_T(Q)/N_T(Q \sim 0) = 0.88_{-0.06}^{+0.12}$ . Because target loss is not actually linear and could have happened after the 288-keV resonance measurement, the uncertainties span the range between no loss and the value given by linear loss.

The 232-keV resonance data were taken with a test target with no protective layer after 13 C had already been bombarded, and target loss was appreciable. At the end of the  $\sim 20$  C irradiation, measurements of the residual activity indicated a 68% loss. As explained above, loss is not linear

and occurs quite rapidly at the end of the cycle. Because of this fact, we have chosen to take the loss only from the difference in monitoring the resonance areas, which were taken directly before and after the measurement and gave  $A(Q)/A(Q \sim 0) = 0.59$ . This value was used to adjust the upper limit on the strength, and we assigned a systematic uncertainty of  $\pm 40\%$  to span a wide range approximately down to the value of linear loss. Regardless, the upper limit on this resonance strength is still dominated by the statistical uncertainty and contributes negligibly to the reaction rate, as will be seen in Chapter 7.

### 5.5 Resonance Energies

We were able to obtain resonance energies with two separate techniques. First, we found the resonance energy from the excitation function. The energy at which the yield reached half its maximum was determined, and the losses in the 20-nm chromium layer and 4 nm of copper were subtracted. This copper depth is the depth at which the  $^{22}\text{Na}$  distribution reached half of its maximum value. According to simulations using TRIM [58], the total subtracted losses were  $\sim 3$  to  $5$  keV, and a 20% uncertainty in the stopping power was assumed. For the 213- and 288-keV resonances, an additional adjustment to the resonance energy was added to account for the slight transformation of the excitation functions due to sputtering, as shown in Fig. 5.1 (b). From repeated scans of the 610-keV resonance, the energy at half of the maximum yield changed by  $1.2 \pm 0.9$  keV after 11 C, in the middle of the 213-keV resonance measurement, and that shift remained constant after 19 C, directly after the 288-keV measurement. Those resonance energies were adjusted by that amount.

Second, we extracted the resonance energy from the observed gamma-ray energy, along with the excitation energy of the daughter level [49] and  $Q$  value ( $7580.53 \pm 0.79$  keV, using the newly measured masses of  $^{23}\text{Mg}$  [65] and  $^{22}\text{Na}$  [66]). From a thick-target  $^{27}\text{Al}(p, \gamma)$  measurement at  $E_p = 406$  keV, the spectrum was calibrated using gamma rays that correspond to transition energies of  $E_{\text{trans}} = 5088.05$  and  $7357.84$  keV and each first-escape peak [61, 49]. The centroid,  $c$ , of each peak was determined via:

$$c = \frac{\sum_i i N_i}{\sum_i N_i}, \quad (5.4)$$

where  $i$  is the channel number,  $N_i$  is the background subtracted number of counts in channel  $i$ , and the sum is over the number of channels encompassing the peak. To minimize uncertainties

associated with gain shifts over time, the  $^{27}\text{Al}(p, \gamma)$  data used for the calibration was taken between measurements on  $^{22}\text{Na}$  targets #3 and #4.

Similarly, excitation energies,  $E_x$ , and gamma-ray energies,  $E_\gamma$ , each were found independently by using the weighted average of the respective value extracted from the excitation function and the respective value extracted from the gamma-ray spectra.

### 5.5.1 Doppler, Recoil, and Rate-Dependent Corrections

When one converts a histogram from an ADC in units of arbitrary channels to units of energy, several corrections must be applied, as the true energy of the observed gamma ray,  $E_\gamma$ , is not equal to the energy measured in the laboratory,  $E_{\gamma\text{meas}}$ , nor is it exactly equal to the nuclear transition energy,  $E_{\text{trans}}$  [31]. When a gamma ray is emitted in a nuclear transition, a recoil correction must be applied because the nucleus must recoil in order to conserve linear momentum ( $E_\gamma = E_{\text{trans}} - E_{\text{recoil}}$ ). A Doppler shift must also be applied because the nucleus emitting the gamma ray is not initially at rest (with respect to the detector), due to momentum conservation in the reaction ( $E_{\gamma\text{meas}} = E_\gamma * E_{\text{Doppler}}$ ). Calculating the energies of the gamma rays from the reaction  $^{22}\text{Na}(p, \gamma)$  is a two-step process. First, the transition energies from the  $^{27}\text{Al}(p, \gamma)$  reaction given in the previous section must have the Doppler and recoil corrections applied. Second, after the measured energy has been determined for  $^{22}\text{Na}(p, \gamma)$  gamma rays from the calibration, they must be have the corrections removed.

Starting with the reaction  $^{27}\text{Al}(p, \gamma)$  and the transition energy,  $E_{\text{trans}}$ , the gamma-ray energy after the recoil correction was applied is equal to:

$$E_\gamma = E_{\text{trans}} - \frac{E_\gamma^2}{2M} \cong E_{\text{trans}} - \frac{E_{\text{trans}}^2}{2M}, \quad (5.5)$$

where  $M$  is the mass of the compound nucleus ( $^{28}\text{Si}$  in this case), and the recoil correction has been approximated as  $E_{\text{trans}}^2/(2M)$ , which is correct to first order. Next, the gamma-ray energy is corrected for Doppler shift (non-relativistically):

$$E_{\text{meas}} = E_\gamma(1 + \beta \cos \theta), \quad (5.6)$$

where  $\theta$  is the angle of the detector with respect to the beam axis,  $55^\circ$ , and

$$\beta = \frac{v_M}{c} = \frac{p_{MC}}{Mc^2} = \frac{\sqrt{2mE_p^2}}{Mc^2}, \quad (5.7)$$

where  $m$  is the mass of the projectile, and  $v_M$  and  $p_M$  are the velocity and momentum of the emitting nucleus, respectively. The values for  $E_{\text{meas}}$  were then used to calibrate the energy spectrum, along with their first-escape energies equal to  $E_{\text{meas}} - 511 \text{ keV}$ . This calibration was then used to extract the measured gamma-ray energies from the  $^{22}\text{Na}(p, \gamma)$  reaction. Reversing the corrections for Doppler first, and then recoil, yield:

$$E_\gamma = \frac{E_{\text{meas}}}{1 + \beta \cos \theta}, \quad (5.8)$$

$$E_{\text{trans}} = E_\gamma + \frac{E_\gamma^2}{2M}, \quad (5.9)$$

where  $M$  is the  $^{23}\text{Mg}$  mass. The resonance energy (in the lab frame) can then be calculated simply as  $E_R = (E_{\text{trans}} - Q - E_f) * (m + M_t)/M_t$ , where  $E_f$  is the final energy level in the transition, and  $M_t$  is the  $^{22}\text{Na}$  mass. The corrections ranged in magnitude from  $\sim 4$  to  $7 \text{ keV}$  for Doppler shift and  $\sim 0.6$  to  $1.5 \text{ keV}$  for recoil, respectively.

Unfortunately, the detector gain depended slightly on rate, which was discovered after all  $^{22}\text{Na}(p, \gamma)$  and calibration data had been taken. However, at a later date, data was taken on an aluminum target with and without  $^{22}\text{Na}$  sources nearby on the same resonance used for calibration. Therefore, for each of the calibration gamma rays, the rate-dependent shift was measured. This shift was then used to directly adjust the measured gamma-ray energy shown in Eq. 5.6. This shifted the energy of the  $^{22}\text{Na}(p, \gamma)$  gamma rays by  $2.4 \pm 0.7$  to  $3.8 \pm 1.1 \text{ keV}$  in magnitude, where we have applied a 30% systematic uncertainty to the shift. Results for final gamma-ray energies and resonance energies are given in Sec. 6.1, whereas results for excitation energies are given in Sec. 6.2.

## 5.6 Branches

Strong branches were determined from the spectra summed over all runs within a particular resonance. For resonances at  $E_p = 454$  and  $610 \text{ keV}$ , which were used as reference resonances to monitor degradation and for other target tests, the total amount of data was significantly larger than for a single resonance scan, and thus, their uncertainties are appreciably smaller.

Due to the very low statistics for weaker possible branches, an additional restriction was placed on the analysis. Similar to our analysis for weak resonances where a reference resonance excitation function was shifted and normalized to fit the data (see Sec. 5.2), the excitation function for the strongest branch (and its first-escape peak for branches from  $E_p = 610 \text{ keV}$ ) was normalized to

match the weaker branches' excitation functions, such that the  $\chi^2$  was minimized. Then the branches were extracted using Eq. 5.3.

Only an upper limit for the branch at  $E_\gamma = 6112$  keV in the  $E_p = 610$  keV resonance could be obtained due to the obscuring peak at  $E_\gamma = 6129$  keV from  $^{19}\text{F}$  contamination. In order to estimate the contribution from the  $^{22}\text{Na}(p, \gamma)$  resonance, the spectral line shape was deconvolved into the contribution from  $^{19}\text{F}$  and from  $^{22}\text{Na}$ . This was done by comparing the on-resonance line shape with the sum of the off-resonance line shape and a shape representing the 6112-keV gamma ray. The latter shape was estimated from a normalized and shifted peak at  $E_\gamma = 8162$  keV, the largest branch in the de-excitation. The value of this normalization was equal to the ratio of the magnitude of the branches, adjusted for efficiency differences, and was extracted by minimizing the  $\chi^2$  of the hybrid curve and the on-resonance curve. Because of the changing shape of the off-resonance curve above and below the resonance, only an upper limit could be extracted.

### 5.7 Verification of Experimental Method: $^{23}\text{Na}(p, \gamma)$ Measurement

In order to verify our technique, targets of  $^{23}\text{Na}$  were implanted using the ion source on the injector deck at the low-energy end of the University of Washington accelerator, and known  $^{23}\text{Na}(p, \gamma)$  resonances were measured under the same conditions as the  $^{22}\text{Na}(p, \gamma)$  measurements. A 20-Å layer of chromium was also evaporated on the surface, similar to the main two  $^{22}\text{Na}$  targets.

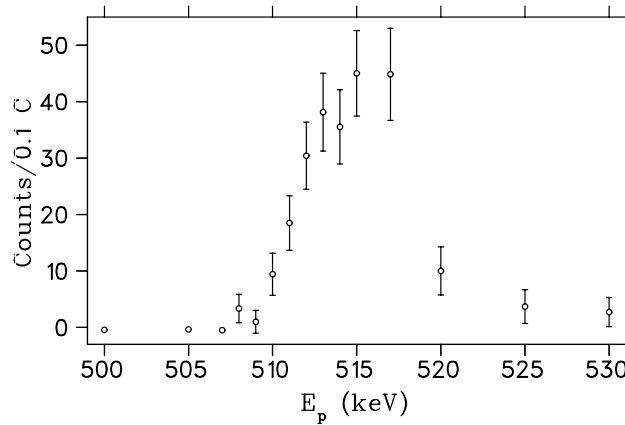


Figure 5.13: Excitation function for  $^{23}\text{Na}(p, \gamma)$  resonance at  $E_p = 512$  keV, gated on  $E_\gamma = 10810$  keV.  $E_p$  is the lab proton energy.

The  $^{23}\text{Na}(p, \gamma)$  resonance at  $E_p = 512$  keV has a reported strength of  $91.3 \pm 12.5$  meV and is the recommended reference resonance for this reaction [67]. We measured this with a target containing  $(5.8 \pm 0.9) \times 10^{15}$  atoms, which includes the integrated charge correction described in Sec. 3.4.2. The excitation function is shown in Fig. 5.13. Using the 10810-keV gamma ray with a branch of 71% [68], we determined its total resonance strength to be  $79 \pm 17$  meV, after applying the correction described in the following subsection.

### 5.7.1 Area Correction

Inspection of the raster plot indicated a small part of the target was missed when using our standard raster. To determine the missing fraction, the target was illuminated with larger raster amplitudes that fully encompassed the target atoms, shown in Fig. 5.14.

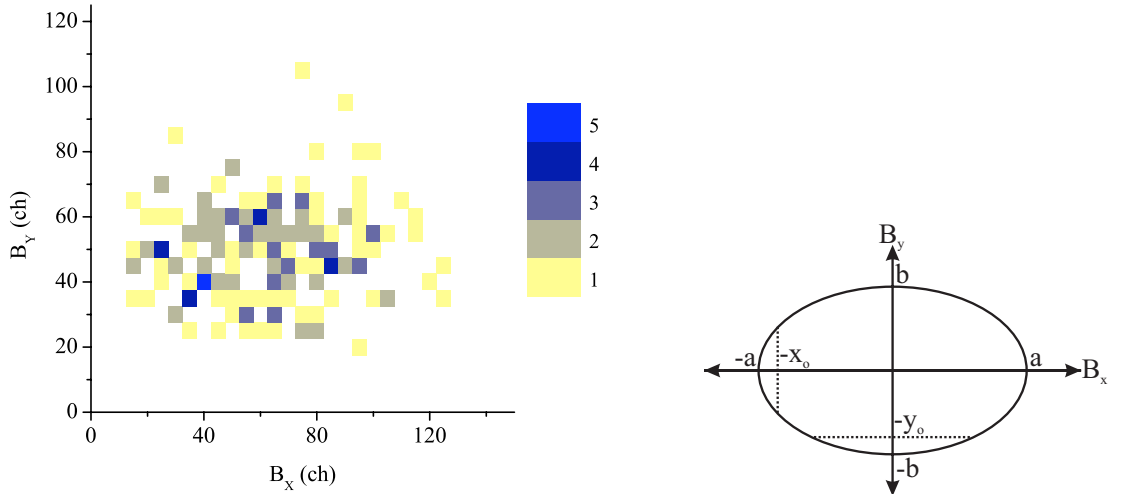


Figure 5.14: Large amplitude raster plot for the sum of  $^{23}\text{Na}(p, \gamma)$ , gated on  $E_\gamma = 10810$  keV.

Figure 5.15: Model of the target to estimate missing area.

The target shape on the raster plots was assumed to be elliptical (although the physical target area was circular,  $B_x$  and  $B_y$  have different gains). Fig. 5.15 is a sketch of this ideal target to aid the following discussion. By using the larger raster amplitude, the target was estimated to span 18 ch to 106 ch in  $B_x$  and 27 ch to 73 ch in  $B_y$  with a center at (62,50), the midpoint of each range. The total area is then simply  $ab\pi$ , where  $a$  is the semi-major axis, and  $b$  is the semi-minor axis of the ellipse.

Possibly due to one of the steering magnets drifting and a slightly non-centered target, instead of spanning from less than 18 ch in  $B_x$  and 27 ch in  $B_y$ , the standard raster started at 23 ch in  $B_x$  and 34 ch in  $B_y$ . This shears off a small section at the bottom of the ellipse and a small section at the left of the ellipse, without the missing areas overlapping (shown schematically in Fig. 5.15). Each missing area,  $A_m$ , was calculated as the integral of the equation for an ellipse from a value of  $x_1$  to value  $x_2$ , re-centered at (0,0):

$$A_m(a, b, x_1, x_2) = \int_{x_1}^{x_2} 2b \sqrt{1 - \frac{x^2}{a^2}} dx. \quad (5.10)$$

Therefore, the ratio of the area illuminated with the standard raster,  $A_s$ , to the large raster,  $A$  is:

$$\frac{A_s}{A} = 1 - \frac{A_m(a, b, -a, -x_o) + A_m(b, a, -b, -y_o)}{A_m(a, b, -a, a)}, \quad (5.11)$$

where  $x_o$  ( $y_o$ ) is the beginning edge of the standard raster in  $B_x$  ( $B_y$ ). It is possible to add the two areas missing in each direction because they do not overlap. For the case of the  $^{23}\text{Na}$  target, this ratio was equal to  $0.88 \pm 0.11$ , and the resonance strength was corrected by this value. This was not necessary with our  $^{22}\text{Na}$  targets, as their respective raster plots indicated the beam covered the entire active area.

Using raster plots to estimate the area is not exact because the beam has an extent, and the raster values are simply its supposed central value. Therefore, it is necessary to estimate a systematic uncertainty associated with this offset. The above area analysis also implicitly assumes that the target and beam are both completely uniform and that there are no effects due to convoluting the offset target area with the beam area. However, during implantation of this target, the  $^{23}\text{Na}$  beam was not rastered to the extreme extents that our  $^{22}\text{Na}$  targets were (in order to decrease fabrication time), so it is likely that the distribution was not as uniform. Simulations were performed to estimate the effect of a non-uniform target with an offset, as described in Sec. 4.3.1. The center of the raster was offset by (9.5,15) channels. In order to convert this into a length, a thick-target measurement of the  $^{27}\text{Al}(p, \gamma)$  resonance with the “coin” target, which had well-defined extents, was performed at the same proton energy as the  $^{23}\text{Na}(p, \gamma)$  resonance,  $E_p = 512$  keV. Using this conversion, the offset was estimated to be equal to 1.8 mm. The simulated target distribution was assumed to be the half cone, half cylinder described in Sec. 4.3.1, and the target offset range was set to be 1.5 to 2.0 mm. The uncertainties associated with these calculations dominate the overall uncertainty quoted above.

## Chapter 6

### RESULTS AND DISCUSSION

Results are shown in Tables 6.1, 6.2, and 6.4. The resonance and gamma-ray energies are summarized in Table 6.1, the excitation energies, gamma-ray branches, and partial strengths for each resonance are summarized in Table 6.2, and the final resonance strengths are summarized in Table 6.4. Systematic errors for the resonance strengths are shown in Table 6.3.

#### **6.1 Resonance Energies**

The resonance energies determined from each method are shown in Table 6.1, and agreement between both methods is quite good. The adopted energy is the weighted average of the two results. We find energies that agree with previously reported values [16, 17, 1], and we have improved the uncertainties on the energies.

#### **6.2 Branches**

Table 6.2 shows our excitation energies, gamma-ray energies, branches, and partial strengths. Also included is a comparison with previous branches. Our branches are in agreement with the previous direct measurements [16, 17] for  $E_p = 288$  and  $610$  keV. For the 6112-keV branch of the 610-keV resonance that could not be resolved from the  $^{19}\text{F}$  contamination, we found the upper limit to be 28%, which is consistent with the value of  $20.0 \pm 1.8\%$  measured directly by Stegmuller *et al.* [17]. We have adopted the branch of Ref [17] to extract its partial strength because it is consistent with ours and is more precise. For the previously established branches of the 454-keV resonance, our branches agree with Jenkins *et al.* [1], and we have improved upon their uncertainties. A new branch has also been identified with  $E_\gamma = 7566$  keV. Although branches for the 213-keV resonance are in agreement with the earlier measurement [17] at the  $2\sigma$  level, an additional branch of  $\sim 11\%$  has since been identified, and we agree with its currently established value [14].

For the observed resonances at  $E_p = 213, 288, 454$ , and  $610$  keV, contributions to the total

Table 6.1: Resonance energies. Values are extracted from the lab proton energy,  $E_p$ , via the excitation function (excitation function), correcting for energy loss  $E_{\text{loss}}$ , and from the gamma-ray energy,  $E_\gamma$ . Statistical uncertainties are given for each individual branch, and combined branches include systematic uncertainties. The adopted value is the weighted average of both methods. All values are in keV.

Previous	Present						
	$E_p$ <sup>a</sup>	$E_\gamma$	$E_p$ (from excitation function): branch	$E_p$ (from $E_\gamma$ ): combined branches	$E_p$ (from $E_\gamma$ ): branch	$E_p$ (from $E_\gamma$ ): combined branches	Adopted $E_p$
213.3 ± 2.7	7332.7 ± 1.2	5.1 ± 1.0	213.1 ± 3.0	213.1 ± 3.4	213.6 ± 1.6	213.6 ± 1.6	213.5 ± 1.4
287.9 ± 2.1	5140.6 ± 1.0	4.6 ± 0.9	286.5 ± 2.1	286.3 ± 2.3	288.4 ± 1.7	288.7 ± 1.3	288.1 ± 1.1
	5803.2 ± 1.3		285.6 ± 4.2		289.1 ± 2.0		
457 ± 2 <sup>b</sup>	5300.1 ± 0.8	3.7 ± 0.8	452.8 ± 0.8	452.8 ± 1.1	455.6 ± 1.7	455.7 ± 1.1	454.2 ± 0.8
	5962.7 ± 0.8		452.8 ± 1.1		455.9 ± 1.6		
611.3 ± 1.8	8162.3 ± 0.9	3.2 ± 0.7	609.6 ± 0.9	609.0 ± 1.1	611.0 ± 1.5	610.8 ± 1.2	609.8 ± 0.8
	7711.2 ± 1.1		608.1 ± 1.1		610.3 ± 2.0		

<sup>a</sup> From Ref. [17], unless otherwise noted.

<sup>b</sup> From Ref. [16].

strength have been investigated for primary transitions to all levels up to the 6th excited state, also shown in Table 6.2. For unobserved branches, limits were obtained via the method described in Sec. 5.6. The branches with a final spin of 1/2 are highly unlikely to be detectable based on angular momentum considerations, so we attribute our non-zero result for  $E_\gamma = 5497$  keV from the 288-keV resonance to statistical fluctuations. Upper limits on partial strengths from spin 1/2 levels have not been included in the strength uncertainties or in the branches. Other branches where only an upper limit could be determined were used to directly increase the upper uncertainty on the total strength but do not affect the central value of the total resonance strength.

### 6.3 Resonance Strengths

The systematic error budget for resonance strengths is shown in Table 6.3. In summary, we find an overall systematic error of  $-11.7\%$  and  $+12.7\%$  for the extended measurements at  $E_p = 198$  and  $213$  keV, resulting from combining uncertainties of  $\pm 6\%$  in the efficiency,  $\pm 10\%$  in the normalized beam density, and  $-2.6\%$  and  $+5.6\%$  from the number of target atoms. For the resonances at  $E_p = 454$  and  $610$  keV, the overall systematic uncertainty is  $\pm 11.7\%$ , and for the resonance at  $E_p = 288$  keV it is  $-18.1\%$  and  $+13.4\%$ . The differences in the uncertainties in the strength all result from the opposite sign error in the number of target atoms. The 232-keV resonance has the largest overall uncertainty,  $\pm 42\%$ .

All finite total strengths are significantly larger than those previously reported [16, 17], as shown in Table 6.4. The 213-keV resonance is stronger by a factor of 3.2, which includes a factor of 2.8 that we observe with respect to the same decay channel observed in Ref. [17].

Iacob *et al.* [14] attempted to extract a resonance strength for  $E_p = 213$  keV by compiling data from several different sources. Using the beta-delayed proton branch from Tighe *et al.* [12], the proton-to-gamma-ray branching of Peräjärvi *et al.* [13], and the lifetime of Jenkins *et al.* [1], Iacob *et al.* claimed a total strength of  $2.6 \pm 0.9$  meV, in contrast to our value of  $5.7^{+1.6}_{-0.9}$  meV. We consider the value of Iacob *et al.* to be unreliable. It is based on the observation of a  $\beta$ -delayed proton peak very close to detection threshold that would have been difficult to disentangle from noise. Indeed, Saastamoinen *et al.* [69] have shown that the  $\beta$ -delayed proton intensity deduced by Tighe *et al.* [12] was too large by a significant amount. In addition, Iacob *et al.*'s value is based on the lifetime of the

state, for which further documentation has not been published.

We have set upper limits on the 198- and 232-keV potential resonances. For  $E_p = 198$  keV, based on a search for the 5055-keV branch, we observe a possible presence in our fits with a non-zero strength at slightly over  $1\sigma$ . Jenkins *et al.* [1] suggested that this resonance could have a strength as high as 4 meV, whereas our 68% *C.L.* upper limit is a factor of 8 smaller. The resonance at  $E_p = 232$  keV also was not observed, based on our search for the two main branches reported by Ref. [1]. This resonance has been demonstrated to be the isospin analogue of the  $T = 3/2$   $^{23}\text{Al}$  ground state [69, 14] so its width for proton decay to  $T = 0$   $^{22}\text{Na}$  is significantly suppressed by isospin conservation, and thus it is expected to have a relatively small ( $p, \gamma$ ) resonance strength. Our direct measurement is consistent with this expectation.

Jenkins *et al.* [1] proposed a new level that corresponds to  $E_p = 209.4(17)$  keV, which produces gamma rays with energies of 5729.1(11) and 5067.1(11) keV and branches of 33(6)% and 66(8)%, respectively. The gamma ray at 5067 keV is very close in energy to the gamma ray from the possible resonance at 198 keV at 5055 keV, as they produce the same final state. We have investigated this resonance, but due to the size of the energy windows necessary on each peak ( $\sim 20$  to 45 keV), it is unclear from which potential resonance these possible gamma rays originate. Contrary to Jenkins *et al.*, Iacob *et al.* [14] attributed the gamma ray at 5729 keV to the resonance at 213 keV. Our branching ratios in Table 6.2 are consistent with Iacob *et al.* and not with Jenkins *et al.* An upper limit of 0.40 meV can be placed on the strength of the 209-keV resonance at the 68% confidence level, and it is possible that part of the contribution originates from the potential resonance at 198 keV.

Seuthe *et al.* [16] also measured resonances at  $E_p = 503, 740$ , and 796 keV that we did not investigate. These resonances do not play an important role in the nova scenarios we consider here, but we nevertheless included our estimate for their contributions in our calculation of the thermonuclear reaction rate. We assumed that the *relative* strength of the resonances to the 454- and 610-keV resonances is correctly given by the result of Seuthe *et al.* Because we observe an average factor of  $2.5 \pm 0.5$  larger for the strengths of resonances observed here with respect to those in Ref. [16], we scaled the  $\omega\gamma$  values in Ref. [16] by this factor.

It is surprising that our strengths are several times higher than those from the previously reported direct  $^{22}\text{Na}(p, \gamma)$  measurements [16, 17]. However, those strengths were determined relative to res-

onance strengths from one experiment performed in 1990 [16], discussed previously in Sec. 1.3.1, also with implanted targets but with  $2\times$  the implantation energy and into a different substrate material. We rastered the beam over the entire target, whereas the measurement of Ref. [16] used a centered beam, which can degrade the target locally in ways that are difficult to characterize. The gamma-ray energy window in that experiment was several MeV for most of the data, although two resonances were measured at peak yield with a high resolution detector. Our energy windows were always narrow, with a maximum of a few tens of keV to incorporate only the relevant peak. Along with a cosmic-ray anticoincidence system, our method employed full excitation functions integrated over proton energy and was independent of absolute stopping-power estimations. Our method required knowledge of only the total number of target atoms, determined from the target activity, and the requirement that the beam covered all target atoms, which we could monitor with the information from the raster. The price paid for eliminating the dependence on the target distribution was the difficulty of determining the beam density. This was accomplished experimentally using a  $^{27}\text{Al}$  coin target, and systematic effects were carefully considered. In addition, our detector efficiency was determined with two radioactive sources and two resonances in the  $^{27}\text{Al}(p, \gamma)$  reaction on two different substrates, spanning a gamma-ray energy scale of 1.3 to 11 MeV, in addition to calculation with detailed simulations. Furthermore, the validity of our method has been confirmed with the  $^{23}\text{Na}(p, \gamma)$  measurement. A target was implanted, and result for the resonance strength are within  $89 \pm 24\%$  of the currently accepted value. Although the error on this quantity is not negligible, it is not a factor of  $\sim 3$  we observe in the  $^{22}\text{Na}(p, \gamma)$  resonance strengths. Thus we are confident in the absolute values we have obtained for the strengths.

Table 6.2: Branches and partial strengths of  $^{22}\text{Na}(p, \gamma)$ .  $E_x$  and  $E_t$  are the excitation and transition energies, respectively. The value given for the branch was determined from the sum of all data for a particular resonance. Systematic errors are not included in the partial strengths. 68% confidence levels are given for all data, and both an upper limit and measurement have been given for  $E_p = 198$  keV. Total strengths are shown in Table 6.4. All upper limits for partial strengths were derived assuming their excitation function was the same shape as for the strongest branch.

$E_x^b$ (keV)	$E_p$ (keV)	$E_t^b$ (keV)	$E_f$ (keV)	$I_f^t$	Branches (%) <sup>a</sup>				$\omega\gamma_{\text{partial}}$ (meV)	
					Previous <sup>c</sup>		Present			
					Ref. [16]	Ref. [17] <sup>d</sup>	Ref. [1]	Ref. [14] <sup>d</sup>		
7770.2±1.4	198	5055	2715	9/2+, 5/2+	-	-	58±8	-	-	$\leq 0.30 (0.20^{+0.15}_{-0.13})$
		2317	5453	-	-	-	42±7	-	-	-e
7782.2±1.2	209	5730	2052	7/2+	-	-	33±6	-	-	-f
		5067	2715	9/2+, 5/2+	-	-	66±8	-	-	$\leq 0.26$
7784.7±1.2	213	7785	0	3/2+	-	≤ 29	-	3.1±2.0	-	$\leq 0.09$
		7334	451	5/2+	-	100	100	80.8±3.6	89.4±5.3	5.1 ± 0.5
		5732	2052	7/2+	-	≤ 29	-	16.2±3.4	10.6±5.3g	0.6±0.3g
		5426	2359	1/2+	-	≤ 29	-	-	-	$\leq 0.24$
		5070	2715	9/2+, 5/2+	-	≤ 29	-	-	-	$\leq 0.33$
		5014	2771	1/2-	-	-	-	-	-	$\leq 0.17$
		4877	2908	(3/2, 5/2)+	-	-	-	-	-	$\leq 0.24$
7802.2±1.4	232	7802	0	3/2+	-	-	-	66.4±2.4	-	$\leq 0.44$
		7351	451	5/2+	-	-	-	29.9±2.4	-	$\leq 1.04$
		5750	2052	7/2+	-	-	-	3.7±1.3	-	-
7856.1±1.0	288	7856	0	3/2+	-	≤ 4.3	-	-	-	$\leq 0.69$
		7405	451	5/2+	-	10.8±2.9	-	-	6.7±2.9	2.6±1.5
		5804	2052	7/2+	36±12	27.2±2.7	-	-	26.2±4.1	10.4±1.9
		5497	2359	1/2+	-	≤ 4.3	-	-	-	2.2±1.6h
		5141	2715	9/2+, 5/2+	64±12	62.0±3.1	100	-	67.1±4.4	26.2±2.9
		5085	2771	1/2-	-	-	-	-	-	$\leq 0.52$
		4948	2908	(3/2, 5/2)+	-	-	-	-	-	$\leq 0.81$
8015.3±0.8	454	8015	0	3/2+	-	-	-	-	-	-i
		7565	451	5/2+	-	-	-	-	4.5±0.8	5.3±1.7
		5963	2052	7/2+	-	-	29±12	-	43.6±1.2	74.7±5.2
		5656	2359	1/2+	-	-	-	-	-	$\leq 1.1$
		5301	2715	9/2+, 5/2+	100	-	71±16	-	51.9±1.2	85.9±5.5
		5244	2771	1/2-	-	-	-	-	-	$\leq 0.8$
		5107	2908	(3/2, 5/2)+	-	-	-	-	-	-j
8163.9±0.8	610	8164	0	3/2+	65±5	65.0±2.3	-	-	61.3±1.8	376±16
		7713	451	5/2+	19±2	15.0±1.8	-	-	18.6 ± 1.3	97±16
		6112	2052	7/2+	16±2	20.0±1.8	100	-	(20.0±1.8) <sup>k</sup>	(118±13) <sup>j</sup>
		5805	2359	1/2+	-	≤ 1.4	-	-	-	$\leq 24$
		5449	2715	9/2+, 5/2+	-	≤ 1.4	-	-	-	$\leq 11$
		5393	2771	1/2-	-	-	-	-	-	$\leq 18$
		5256	2908	(3/2, 5/2)+	-	-	-	-	-	$\leq 18$

<sup>a</sup> We assume the sum of all observed branches adds up to 100%.

<sup>b</sup> Derived from our results in Table 6.1. Otherwise from NNDC [49].

<sup>c</sup> Branches from upper limits are calculated as the partial strength relative to the total observed strength.

<sup>d</sup> Converted finite values into percents.

<sup>e</sup> Partial strengths cannot be determined. See Table 6.4 for upper limits on total strengths.

<sup>f</sup> Any contribution from this branch has been attributed to  $E_p = 213$  keV.

<sup>g</sup> Imposed the restriction that the shape of the excitation function must be the same as for the strongest branch.

<sup>h</sup> Because  $I_f = 1/2$ , this state is highly unlikely to have a detectable value so we attribute this value to statistical fluctuations and do not include it in  $\omega\gamma_{\text{total}}$ .

<sup>i</sup> Could not be determined due to a small percentage of pulser counts sorted into this energy window.

<sup>j</sup> Could not be determined due to  $^{19}\text{F}$  background.

<sup>k</sup> The value from Ref. [17] is used, as this gamma ray was obscured by  $^{19}\text{F}$  background in our measurements.

<sup>l</sup> Estimated from branch.

Table 6.3: Summary of systematic errors for each resonance strength. Note, the total error for the resonances at  $E_p = 198$  and 232 keV is dominated by statistical errors.

Source of Systematic Error	$E_p$ (keV)			
	454/610	213/198	288	232
Efficiency	6%	6%	6%	6%
Normalized beam density	10%	10%	10%	10%
Total number of atoms	2.6%	$^{+5.6\%}_{-2.6}$	$^{+7\%}_{-14}$	40%
Total	11.7%	$^{+12.7\%}_{-11.7}$	$^{+13.4\%}_{-18.1}$	42%

Table 6.4:  $^{22}\text{Na}(p, \gamma)$  resonance strengths. Upper limits are at the 68% confidence level. Both an upper limit and measurement have been given for  $E_p = 198$  keV. The total strength was equal to the sum of partial strengths given in Table 6.2 for all resonances, with the exception of  $E_p = 198, 209$ , and  $232$  keV where branches from Refs. [1, 14] must be used. If only an upper limit has been given to a particular branch in Table 6.2, then its value directly increased our upper uncertainty only, not the central value. This significantly affects the upper limit on the 213-, 288-, and 610-keV resonances.

	Present	Previous	Present
$E_p^{\text{lab}}$	$E_p^{\text{cm}}$ (keV)	$\omega\gamma_{\text{total}}$ (meV) <sup>a</sup>	$\omega\gamma_{\text{total}}$ (meV)
45	$43.1 \pm 1.7^{\text{b}}$	$(7.1 \pm 2.9) \times 10^{-14^{\text{b}}}$	$(7.1 \pm 2.9) \times 10^{-14^{\text{b}}}$
70	$66.6 \pm 3.0^{\text{b}}$	$(5.1 \pm 2.1) \times 10^{-10^{\text{b}}}$	$(5.1 \pm 2.1) \times 10^{-10^{\text{b}}}$
198	$189.5 \pm 1.8^{\text{c}}$	$\leq 4^{\text{c}}$	$\leq 0.51$ ( $0.34_{-0.22}^{+0.25}$ )
209	$200.2 \pm 1.6^{\text{c}}$	$(5 \times 10^{-2})^{\text{c}}$	$\leq 0.40^{\text{d}}$
213	$204.1 \pm 1.4$	$1.8 \pm 0.7^{\text{e}}$	$5.7_{-0.9}^{+1.6}$
232	$221.4 \pm 2.3^{\text{c}}$	$2.2 \pm 1.0^{\text{c}}$	$\leq 0.67$
288	$275.4 \pm 1.1$	$15.8 \pm 3.4$	$39 \pm 8$
454	$434.3 \pm 0.8$	$68 \pm 20$	$166 \pm 22$
503	$481 \pm 2^{\text{a}}$	$37 \pm 12$	$93 \pm 36^{\text{f}}$
610	$583.1 \pm 0.8$	$235 \pm 33$	$591_{-74}^{+103^{\text{g}}}$
740	$708 \pm 2^{\text{a}}$	$364 \pm 60$	$913 \pm 174^{\text{f}}$
796	$761 \pm 2^{\text{a}}$	$95 \pm 30$	$238 \pm 79^{\text{f}}$

<sup>a</sup> From Ref. [16, 17].

<sup>b</sup> From or derived from Ref. [19].

<sup>c</sup> From Ref. [1].

<sup>d</sup> Not included in the present reaction rate.

<sup>e</sup> Actual value measured was 1.4 meV, inflated to 1.8 meV to account for possible unknown branches.

<sup>f</sup> Scaled from Ref [16]. Not measured in this work.

<sup>g</sup> Includes estimated partial branch from  $E_{\gamma} = 6112$  keV.

## Chapter 7

### ASTROPHYSICAL IMPLICATIONS

#### 7.1 Re-evaluating the Thermonuclear Reaction Rate of $^{22}\text{Na}(p, \gamma)^{23}\text{Mg}$

Using the resonance energies and total strengths shown in Table 6.4, we calculated the contributions to the  $^{22}\text{Na}(p, \gamma)^{23}\text{Mg}$  thermonuclear reaction rate under the narrow-resonance formalism discussed in detail in Sec. 2.5.1. Monte Carlo methods were employed, assuming symmetric (asymmetric) gaussian distributions for all measured resonances with symmetric (asymmetric) uncertainties. For the proposed resonances at  $E_p = 198$  and  $232$  keV, their distributions were taken to be the curves shown on the right sides of Figs. 5.8 and 5.9.  $R_{\text{central}}$  is defined as the 50% quantile of the distribution of rates at a given temperature, and  $R_{\text{upper}}$  and  $R_{\text{lower}}$  are the 16% and 84% quantiles, respectively.

The proposed resonance at  $E_p = 209$  keV has not been included in the reaction rate, as its previously estimated strength [1] is so weak that its contribution should be negligible. In addition, the upper limit this work sets is conservative because of potential contributions from nearby resonances to the excitation function. The strengths of the resonances at  $E_p = 45$  and  $70$  keV are too low to be measured directly due to the Coulomb barrier but have been included in the calculation of the reaction rate derived from Ref. [19], based on the  $(^3\text{He}, d)$  spectroscopic factors of Ref [11].

In Fig. 7.1, we show the individual contributions to the thermonuclear rate for  $^{22}\text{Na}(p, \gamma)$  as well as relative contributions of selected resonances. As one can see, the possible contribution from the resonance at  $E_p = 198$  keV is less than that from the resonance at  $E_p = 213$  keV for all temperatures of interest to novae. Therefore, the resonance at  $E_p = 198$  keV does not dominate the reaction rate in this region, as Jenkins *et al.* [1] proposed it might. Rather, the resonance at  $E_p = 213$  keV makes the most important contribution. Also, at the higher temperatures around 0.4 GK, the contribution of the 288-keV resonance becomes significant. The other resonance contributions are effectively negligible at nova temperatures.

Fig. 7.2 illustrates the total reaction rate relative to previous direct measurements [16, 17], showing that our rate is inconsistent with previous work at all temperatures. The dashed line and hatched

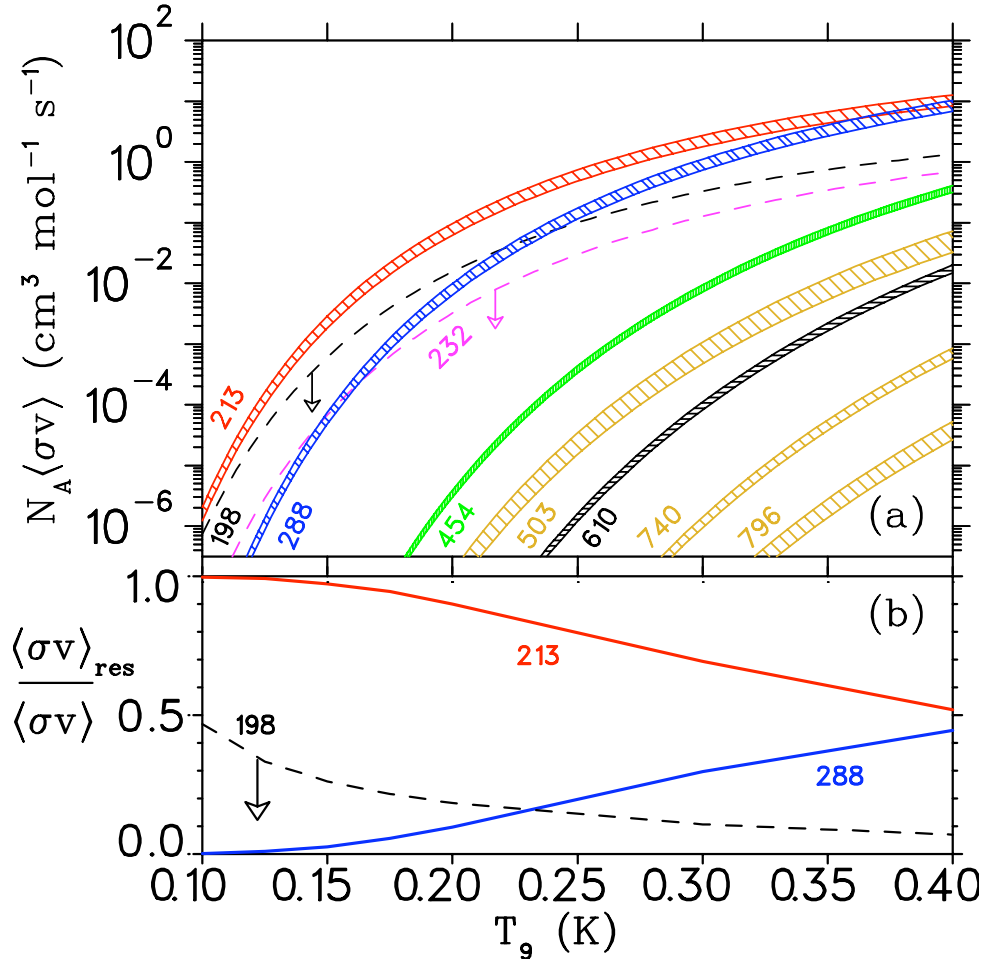


Figure 7.1: Thermonuclear  $^{22}\text{Na}(p, \gamma)^{23}\text{Mg}$  reaction rate as a function of temperature. Panel (a) shows contributions to the reaction rate from individual resonances labeled by  $E_p$  in keV, based on present measurements. Hatched regions represent 68% confidence levels (although the uncertainties are so small they may appear as solid lines), and dashed lines with arrows are 68% confidence level upper limits. Panel (b) shows the fraction contributions of selected resonances to the total rate, as calculated using the resonances illustrated in panel (a).

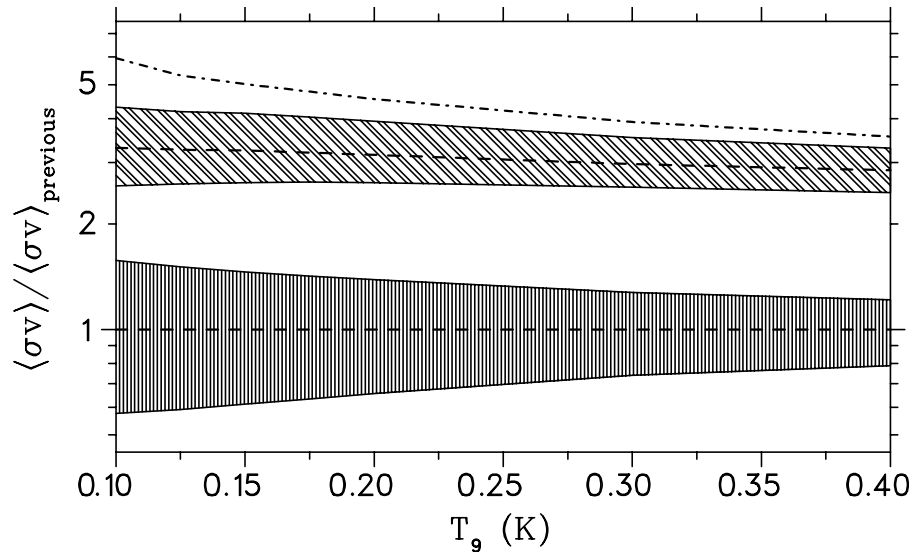


Figure 7.2: Ratio of present (slanted hatches) and previous (vertical hatches) [16, 17] to previous thermonuclear  $^{22}\text{Na}(p, \gamma)^{23}\text{Mg}$  reaction rate as a function of temperature. Hatched areas represent 68% *C.L.* error bands and dashed lines represent the central value, each relative to the previous central value. Both previous and present resonance strengths are listed in Table 6.4. Including the distributions for the resonances at  $E_p = 198$  and  $232$  keV increases the present upper limit to the dot-dashed line.

region in this figure do not include the distributions for proposed resonances at  $E_p = 198$  and 232 keV. The 232-keV resonance makes an insignificant contribution at all temperatures of interest to novae; however, although the 198-keV resonance was unobserved and an upper limit has been placed on its strength, including its potential contributions to the reaction rate has a non-negligible effect at low temperatures. Including the proposed resonances increases the upper limit of the reaction rate to the dot-dashed line shown in Fig. 7.2. Because of this difference, we have calculated the reaction rate for each of these two separate cases, and the values are shown in Table 7.1.

## 7.2 Consequences for Nucleosynthesis of $^{22}\text{Na}$

We can anticipate the general ramifications of the new rate on expected nucleosynthesis of  $^{22}\text{Na}$  in ONe novae using post-processing network calculations because the total energy generation is not affected appreciably by the  $^{22}\text{Na}(p, \gamma)$  reaction. Based on the one-zone calculations of Ref. [8], a specific model indicates that the production of  $^{22}\text{Na}$  is related inversely to the  $^{22}\text{Na}(p, \gamma)$  reaction rate, as shown in Fig. 7.3.

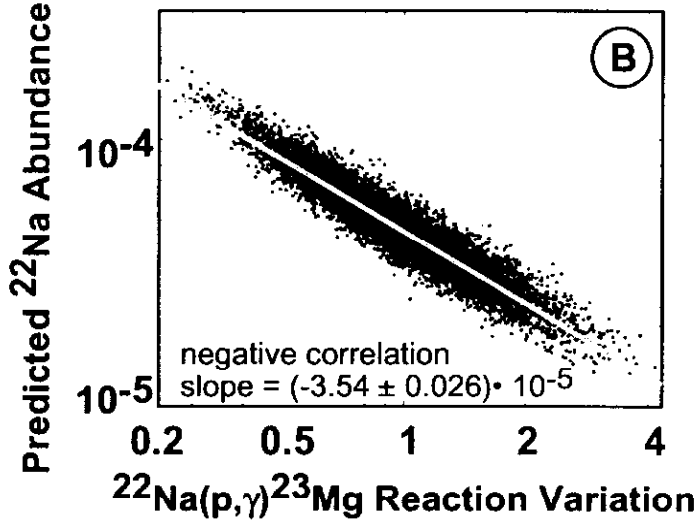


Figure 7.3:  $^{22}\text{Na}$  predicted abundance as a function of  $^{22}\text{Na}(p, \gamma)$  reaction rate [8].

The authors of Ref. [67] also varied the rate by a factor of two using various one-zone models of novae to extract the effect. Using the information given in these references and our change in the

Table 7.1: Table of the thermonuclear  $^{22}\text{Na}(p, \gamma)^{23}\text{Mg}$  reaction rate,  $R$ , as a function of temperature,  $T$ , determined using the energies and strengths given in Table 6.4. Two distributions of rates were calculated, one of which includes the probability density functions from resonances at  $E_p = 198$  and  $232$  keV and one which does not.  $R_{\text{central}}$  is the 50% quantile of the distribution of rates at a given temperature, and  $R_{\text{upper}}$  and  $R_{\text{lower}}$  are the 16% and 84% quantiles, respectively. The units of the rate are  $\text{cm}^3\text{mol}^{-1}\text{s}^{-1}$ .

$T$ (GK)	R (not including “198, 232” <sup>a</sup> )			R (including “198, 232” <sup>a</sup> )		
	$R_{\text{central}}$	$R_{\text{lower}}$	$R_{\text{upper}}$	$R_{\text{central}}$	$R_{\text{lower}}$	$R_{\text{upper}}$
0.01	$2.0 \times 10^{-30}$	$2.7 \times 10^{-31}$	$1.5 \times 10^{-29}$	$2.0 \times 10^{-28}$	$2.7 \times 10^{-29}$	$1.5 \times 10^{-29}$
0.02	$5.5 \times 10^{-20}$	$1.9 \times 10^{-20}$	$1.6 \times 10^{-19}$	$5.5 \times 10^{-20}$	$1.9 \times 10^{-20}$	$1.6 \times 10^{-19}$
0.03	$2.6 \times 10^{-16}$	$1.3 \times 10^{-16}$	$5.6 \times 10^{-16}$	$2.6 \times 10^{-16}$	$1.3 \times 10^{-16}$	$5.6 \times 10^{-16}$
0.04	$4.6 \times 10^{-14}$	$2.0 \times 10^{-14}$	$1.1 \times 10^{-13}$	$4.6 \times 10^{-14}$	$2.1 \times 10^{-14}$	$1.1 \times 10^{-13}$
0.05	$1.4 \times 10^{-12}$	$6.4 \times 10^{-13}$	$3.1 \times 10^{-12}$	$1.4 \times 10^{-12}$	$6.4 \times 10^{-13}$	$3.1 \times 10^{-12}$
0.06	$1.4 \times 10^{-11}$	$7.1 \times 10^{-10}$	$2.8 \times 10^{-11}$	$1.5 \times 10^{-11}$	$7.7 \times 10^{-12}$	$2.9 \times 10^{-11}$
0.07	$1.8 \times 10^{-10}$	$1.3 \times 10^{-10}$	$2.5 \times 10^{-10}$	$2.7 \times 10^{-10}$	$2.0 \times 10^{-10}$	$3.6 \times 10^{-10}$
0.08	$6.2 \times 10^{-9}$	$4.7 \times 10^{-9}$	$8.2 \times 10^{-9}$	$9.7 \times 10^{-9}$	$7.2 \times 10^{-9}$	$1.3 \times 10^{-8}$
0.09	$1.3 \times 10^{-7}$	$1.0 \times 10^{-7}$	$1.8 \times 10^{-7}$	$2.0 \times 10^{-7}$	$1.5 \times 10^{-7}$	$2.6 \times 10^{-7}$
0.10	$1.6 \times 10^{-6}$	$1.2 \times 10^{-6}$	$2.1 \times 10^{-6}$	$2.2 \times 10^{-6}$	$1.7 \times 10^{-6}$	$2.8 \times 10^{-6}$
0.15	$2.3 \times 10^{-3}$	$1.9 \times 10^{-3}$	$3.0 \times 10^{-3}$	$2.9 \times 10^{-3}$	$2.4 \times 10^{-3}$	$3.6 \times 10^{-3}$
0.2	$8.5 \times 10^{-2}$	$7.1 \times 10^{-2}$	$1.1 \times 10^{-1}$	$1.0 \times 10^{-1}$	$8.4 \times 10^{-2}$	$1.2 \times 10^{-1}$
0.3	$3.1 \times 10^{+00}$	$2.7 \times 10^{+00}$	$3.7 \times 10^{+00}$	$3.5 \times 10^{+00}$	$3.0 \times 10^{+00}$	$4.1 \times 10^{+00}$
0.4	$1.9 \times 10^{+01}$	$1.7 \times 10^{+01}$	$2.2 \times 10^{+01}$	$2.1 \times 10^{+01}$	$1.8 \times 10^{+01}$	$2.4 \times 10^{+01}$
0.5	$5.9 \times 10^{+01}$	$5.1 \times 10^{+01}$	$6.7 \times 10^{+01}$	$6.3 \times 10^{+01}$	$5.4 \times 10^{+01}$	$7.1 \times 10^{+01}$
0.6	$1.3 \times 10^{+02}$	$1.1 \times 10^{+02}$	$1.4 \times 10^{+02}$	$1.3 \times 10^{+02}$	$1.2 \times 10^{+02}$	$1.5 \times 10^{+02}$
0.7	$2.3 \times 10^{+02}$	$2.0 \times 10^{+02}$	$2.5 \times 10^{+02}$	$2.4 \times 10^{+02}$	$2.1 \times 10^{+02}$	$2.6 \times 10^{+02}$
0.8	$3.6 \times 10^{+02}$	$3.2 \times 10^{+02}$	$4.0 \times 10^{+02}$	$3.7 \times 10^{+02}$	$3.3 \times 10^{+02}$	$4.1 \times 10^{+02}$
0.9	$5.4 \times 10^{+02}$	$4.8 \times 10^{+02}$	$5.9 \times 10^{+02}$	$5.5 \times 10^{+02}$	$5.0 \times 10^{+02}$	$6.0 \times 10^{+02}$
1.0	$7.5 \times 10^{+02}$	$6.8 \times 10^{+02}$	$8.1 \times 10^{+02}$	$7.6 \times 10^{+02}$	$6.9 \times 10^{+02}$	$8.3 \times 10^{+02}$
1.5	$2.2 \times 10^{+03}$	$2.1 \times 10^{+03}$	$2.4 \times 10^{+03}$	$2.2 \times 10^{+03}$	$2.1 \times 10^{+03}$	$2.4 \times 10^{+03}$
2.0	$3.9 \times 10^{+03}$	$3.6 \times 10^{+03}$	$4.2 \times 10^{+03}$	$3.9 \times 10^{+03}$	$3.6 \times 10^{+03}$	$4.2 \times 10^{+03}$

<sup>a</sup> “198, 232” denotes resonances at  $E_p = 198$  and  $232$  keV.

reaction rate, the estimated abundance of  $^{22}\text{Na}$  in novae is expected to be reduced by factors of 2 to 3 of what was previously expected, depending on white dwarf mass and composition. This will directly affect the expected flux of  $^{22}\text{Na}$  gamma rays observed using orbiting gamma-ray telescopes.

In addition, the impact of our  $^{22}\text{Na}(p, \gamma)$  reaction rate on the amount of  $^{22}\text{Na}$  ejected during nova outbursts has been tested through a series of hydrodynamic simulations performed by Jordi José [21]: three evolutionary sequences of nova outbursts hosting ONe white dwarfs of 1.15, 1.25 and  $1.35M_{\odot}$  have been computed with the spherically symmetric, Lagrangian, hydrodynamic code SHIVA, extensively used in the modeling of such explosions (see Ref. [3], for details). Results have been compared with those obtained in three additional hydrodynamic simulations, for the same white dwarf masses described above and same input physics except for the  $^{22}\text{Na}(p, \gamma)$  rate, which was derived from Refs. [16, 17]. The network used for additional reaction rates is the relevant subset of that used in Ref. [70]. The estimated  $^{22}\text{Na}$  yields (mass-averaged mass fractions in the overall ejected shells) are listed in Table 7.2, which clearly shows that the impact of the central value of new rate roughly translates into lower  $^{22}\text{Na}$  abundances by a factor up to  $\sim 2$  with respect to previous estimates. This, in turn, directly affects the chances to potentially detect the 1275-keV gamma-ray line from  $^{22}\text{Na}$  decay, decreasing the maximum detectability distances by a factor  $\sim 1.4$ . The inclusion of the 198- and 232-keV distributions in the rate does not appreciably alter this factor.

The results from one-zone post-processing network calculations and full hydrodynamic simulations using SHIVA are complementary. The post-processing approach mimics the processes that occur in the deepest envelope layers, whereas the hydrodynamic simulations average the yields over all ejected shells. Convection also plays a critical role, supplying fresh, unburned material from external shells into the innermost one (and vice versa), and these effects cannot be simulated in a post-processing framework. As a result of the more realistic physics in the hydrodynamic model, the composition of the innermost shell is diluted by the compositions of the outermost ones. On the other hand, the post-processing calculations cover various nova models, a wider range of nova masses and compositions, and show that the correlation between the  $^{22}\text{Na}(p, \gamma)$  rate and  $^{22}\text{Na}$  production is robust even when other reaction rates are simultaneously varied. It seems reasonable to assume that the magnitude of the dilution from the hydrodynamic models ( $\approx 25\%$ ) applies generally to all of the post-processing results.

Table 7.2:  $^{22}\text{Na}$  yields from novae on ONe white dwarfs of various masses computed with SHIVA [3]. The total mass ejected is given for each case, along with the mass fractions of  $^{22}\text{Na}$  obtained using the central value of the previous [16, 17] and both present  $^{22}\text{Na}(p, \gamma)^{23}\text{Mg}$  reaction rates compiled in Table 7.1. The factor given is the ratio of previous to respective present amounts of  $^{22}\text{Na}$  ejected.

	$1.15M_{\odot}$	$1.25M_{\odot}$	$1.35M_{\odot}^{\text{a}}$
$M_{\text{eject}}$ (g)	$4.9 \times 10^{28}$	$3.8 \times 10^{28}$	$9.0 \times 10^{27}$
Previous <sup>b</sup>	$1.6 \times 10^{-4}$	$1.9 \times 10^{-4}$	$5.9 \times 10^{-4}$
Present <sup>c</sup>	$8.8 \times 10^{-5}$	$1.1 \times 10^{-4}$	$4.1 \times 10^{-4}$
Factor	1.8	1.8	1.4
Present <sup>d</sup>	$7.8 \times 10^{-5}$	$1.0 \times 10^{-4}$	$3.8 \times 10^{-4}$
Factor	2.0	1.9	1.5

<sup>a</sup> Statistically, there should be more novae of  $1.15M_{\odot}$  and  $1.25M_{\odot}$  than those hosting  $1.35M_{\odot}$ , due to the stellar mass function of the progenitors.

<sup>b</sup> From Ref. [16, 17].

<sup>c</sup> Not including “198, 232” from Table 7.1.

<sup>d</sup> Including “198, 232” from Table 7.1.

## Chapter 8

### **CONCLUSIONS, IMPROVEMENTS, AND FUTURE PROSPECTS**

We have measured the resonance strengths, energies, and branches of the  $^{22}\text{Na}(p, \gamma)^{23}\text{Mg}$  reaction directly and absolutely. Our method improved upon past measurements in several ways. The use of integrated yields makes the results independent of absolute stopping power calculations and is far more robust than using peak yields. We also utilized isotopically-pure, implanted targets that demonstrated nearly zero loss during bombardment, and relied on robust integrated yields instead of peak yields. HPGe detectors exhibit excellent energy resolution, providing the ability to use narrow energy windows, and anticoincidence shields enabled suppression of the cosmic-ray background. Absolute detector efficiency was also vital, which we determined by fusing measurement and simulation. Finally, the rastering of the beam across the target not only aided in maintaining target integrity, but also removed the requirement of detailed knowledge of the target distribution. A determination of the beam density was mandatory and was ascertained by both measurement and modeling. As a consequence of the aforementioned points, our results should be substantially more reliable than previous measurements.

By exploiting these advantages, our measurement has shown that four previously measured resonance strengths are 2.4 to 3.2 times higher than previously reported [16, 17]. Jenkins *et al.* also proposed that a new  $^{22}\text{Na}(p, \gamma)$  resonance with  $E_p = 198$  keV could dominate the reaction rate in novae [1]. We have demonstrated that this is not the case, and that the main contributions arise from the resonance at  $E_p = 213$  keV. As a result of the higher resonance strengths, the estimated flux of  $^{22}\text{Na}$  gamma rays from novae is expected to be about a factor of 2 less than what was previously expected, determined by using both post-processing network calculations and hydrodynamic simulations. The lack of observational evidence of  $^{22}\text{Na}$  in the cosmos is consistent with the previous reaction rate; however, the present rate makes detection  $\sim 1.4$  times more difficult.

Improvements to the present measurement could include a more rigorous determination of the beam density and its uncertainties. Our central value for this parameter was extracted from mea-

surements on our “coin”  $^{27}\text{Al}$  target at only two separate times. It is possible that in the interim measurements that the beam density had a different value. Measuring this quantity more often would increase our confidence and decrease its uncertainty. However, this method requires a change of target and possible change in beam tune. A more accurate method would be to construct a device to measure the density *in-situ*, such as in the experiment by Ref. [26]. A simple alternative would have been to sweep the beam over a much larger area such that the beam density would be entirely uniform over the 8-mm collimator and would be equal to the charge on the target divided by the collimator area. Although this is straightforward, it would have led to a prohibitive amount of time for our experiment to collect data for comparable statistics. Of course, an intermediate raster smaller than previously suggested but larger than our standard raster might be a better compromise.

Smaller improvements would be taking all non- $^{22}\text{Na}(p, \gamma)$  data in the presence of the  $^{22}\text{Na}$  sources to minimize any rate-dependent effects, such as detector gain shifts. Although the background rate for  $^{22}\text{Na}(p, \gamma)$  gamma rays was dominated by beam-related Compton gamma rays, the cosmic ray shielding geometry could also have been optimized for the experimental setup, instead of borrowing shielding from a previous experiment. This was not done because costs were exorbitant for a slight enhancement of the rejection probability.

The main source of dead time was using the Ge amplifiers in pile-up-rejection mode. Many signals were rejected because the amplifier had not finished processing one signal before another began, due to the long integration time to maintain a high resolution in a large detector. If there were some method to improve the detector technology to collect the deposited charge faster, this would be a very beneficial way to improve the statistics of a measurement.

Although we have determined that the 198-keV resonance does not dominate the  $^{22}\text{Na}(p, \gamma)$  reaction rate, the upper limit we have set indicates that its contribution could be up to 50% of the 213-keV resonance contribution at 0.1 GK. Further measurements could be performed to decrease this limit or more precisely measure the resonance strength, if it is indeed this strong. Direct measurements could also be performed in inverse kinematics to further confirm the absolute value of the resonance strengths, at least at the higher proton energies where the strengths are hundreds of meV.

## BIBLIOGRAPHY

- [1] D. G. Jenkins *et al.* *Phys. Rev. Lett.*, 92:031101, 2004.
- [2] R. D. Gehrz, J. W. Truran, R. E. Williams, and S. Starrfield. *Publ. Astron. Soc. Pac.*, 110:3, 1998.
- [3] J. Jose and M. Hernanz. *Astrophys. J.*, 494:680, 1998.
- [4] S. Starrfield, J. W. Truran, M. Wiescher, and W. M. Sparks. *Nucl. Phys. A*, 621:495, 1997.
- [5] C. Iliadis, A. Champagne, J. José, S. Starrfield, and P. Tupper. *Astrophys. J.s*, 142:105, 2002.
- [6] J. José, M. Hernanz, and C. Iliadis. *Nucl. Phys. A*, 777:550, 2006.
- [7] J. José, A. Coc, and M. Hernanz. *Astrophys. J.*, 520:347–360, 1999.
- [8] W. R. Hix, M. S. Smith, S. Starrfield, A. Mezzacappa, and D. L. Smith. *Nucl. Phys. A*, 718:620, 2003.
- [9] S. Kubono *et al.* *Zeit. Phys. A*, 348:59, 2009.
- [10] H. Nann, A. Saha, and B. H. Wildenthal. *Phys. Rev. C*, 23:606, 1981.
- [11] S. Schmidt, C. Rolfs, W. H. Schulte, H. P. Trautvetter, R. W. Kavanagh, C. Hategan, S. Faber, B. D. Valnion, and G. Graw. *Nucl. Phys. A*, 591:227, 1995.
- [12] R. J. Tighe, J. C. Batchelder, D. M. Moltz, T. J. Ognibene, M. W. Rowe, J. Cerny, and B. A. Brown. *Phys. Rev. C*, 52:2298, 1995.
- [13] K. Peräjärvi, T. Siiskonen, A. Honkanen, P. Dendooven, A. Jokinen, P. O. Lipas, M. Oinonen, H. Penttilä, and J. Äystö. *Phys. Lett. B*, 492:1, 2000.
- [14] V. E. Iacob, Y. Zhai, T. Al-Abdullah, C. Fu, J. C. Hardy, N. Nica, H. I. Park, G. Tabacaru, L. Trache, and R. E. Tribble. *Phys. Rev. C*, 74:045810, 2006.
- [15] J. Görres, M. Wiescher, S. Graff, R. B. Vogelaar, B. W. Filippone, C. A. Barnes, S. E. Kellogg, T. R. Wang, and B. A. Brown. *Phys. Rev. C*, 39:8, 1989.
- [16] S. Seithe *et al.* *Nucl. Phys. A*, 514:471, 1990.

- [17] F. Stegmuller *et al.* *Nucl. Phys. A*, 601:168, 1996.
- [18] T. A. D. Brown, K. Deryckx, A. García, A. L. Sallaska, K. A. Snover, D. W. Storm, and C. Wrede. *Nucl. Instr. and Meth. B*, 267:3302, 2009.
- [19] C. Iliadis, R. Longland, A. Champagne, and A. Coc. *Nucl. Phys. A*, 841:31–250, 2010.
- [20] A. L. Sallaska *et al.* *Phys. Rev. Lett.* 105, 152501 (2010).
- [21] A. L. Sallaska *et al.* *Phys. Rev. C* (submitted); arXiv:1009.3925v1 [nucl-ex].
- [22] G. A. P. Engelbertink and P. M. Endt. *Nucl. Phys.*, 88:12, 1966.
- [23] P. W. M. Glaudemans and P. M. Endt. *Nucl. Phys.*, 30:30, 1962.
- [24] Z. E. Switkowsi *et al.* *Aust. J. Phys.*, 28:141, 1975.
- [25] B. M. Paine and D. G. Sargood. *Nucl. Phys. A*, 331:389, 1979.
- [26] A. R. Junghans *et al.* *Phys. Rev. C*, 68:065803, 2003.
- [27] C. E. Rolfs and W. S. Rodney. *Cauldrons in the Cosmos*. The University of Chicago Press, 1988.
- [28] By Richard Powell minor adjustments by:penubag (original image) (The Hertzsprung Russell Diagram) [Public domain, CC-BY-SA-2.5 ([www.creativecommons.org/licenses/by-sa/2.5](http://www.creativecommons.org/licenses/by-sa/2.5)) or CC-BY-SA-2.5 ([www.creativecommons.org/licenses/by-sa/2.5](http://www.creativecommons.org/licenses/by-sa/2.5))], via Wikimedia Commons.
- [29] <http://www.enchantedlearning.com/subjects/astronomy/stars/lifecycle/>.
- [30] C. Iliadis. *Nuclear Physics of Stars*. Weinheim: Wiley-VCH, 2007.
- [31] K. S. Krane. *Introductory Nuclear Physics*. John Wiley & Sons, Inc., 1987.
- [32] <http://sci.esa.int/integral/>.
- [33] R. Diehl, *INTEGRAL and Gamma-Ray Lines from Cosmic Nucleosynthesis*, 11th Symposium on Nuclei in the Cosmos, Heidelberg, Germany, 2010.
- [34] S. Amari, X. Gao, L. R. Nittler, E. Zinner, J. José, M. Hernanz, and R. S. Lewis. *Astrophys. J.*, 551:1065, 2001.
- [35] D. C. Black. *Geoch. Cosmoch. Acta*, 36:447, 1972.

- [36] S. Amari. *NewAR*, 46:519, 2002.
- [37] [http://ircamera.as.arizona.edu/astr\\_250/Lectures/Lec17\\_sml.htm](http://ircamera.as.arizona.edu/astr_250/Lectures/Lec17_sml.htm).
- [38] C. Kittel and H. Kroemer. *Thermal Physics*. W. H. Freeman and Company, 1998.
- [39] D. D. Clayton and F. Hoyle. *Astrophys. J.l*, 187:L101, 1974.
- [40] R. Diehl *et al.* *Nature (London)*, 439:45, 2006.
- [41] C. Ruiz *et al.* *Phys. Rev. Lett.*, 96:252501, 2006.
- [42] A. F. Iyudin *et al.* *Astron. Astrophys.*, 300:422, 1995.
- [43] S. Bishop *et al.* *Phys. Rev. Lett.*, 90:162501, 2003.
- [44] M. Hernanz and J. José. *New Astro. Rev.*, 48:35–39, 2004.
- [45] R. D. Hoffman S. E. Woosley, D. H. Hartmann and W. C. Haxton. *Astrophys. J.*, 356:272, 1990.
- [46] L. Bildsten, *Nuclear Physics and Astrophysics of Exploding Stars*, Joint National Nuclear Physics Summer School and TRIUMF Summer Institute, Vancouver, BC, Canada, 2010.
- [47] D. Garfinkle. *Am. J. of Phys.*, 77:683, 2009.
- [48] J. J. Sakurai. *Modern Quantum Mechanics*. Addison-Wesley Publishing Company, 1994.
- [49] <http://www.nndc.bnl.gov/>.
- [50] Private communications between K. Snover and D. G. Jenkins.
- [51] J. D. Jackson. *Classical Electrodynamics*. John Wiley & Sons, Inc., 3rd edition, 1999.
- [52] S. DeBenedetti. *Nuclear Interactions*. John Wiley & Sons, Inc., 1964.
- [53] H. Frauenfelder and E. M. Henley. *Subatomic Physics*. Prentice-Hall, Inc., 1974.
- [54] M. Bacrania. Ph.D. thesis, University of Washington (2006).
- [55] F. Salvat, J. M. Fernández-Varea, and J. Sempau, PENELOPE-2006: a code system for Monte Carlo simulation of electron and photon transport NEA Report 6222 <http://www.nea.fr/html/science/pubs/2006/nea6222-penelope.pdf> (2006).

- [56] F. Salvat, J. M. Fernández-Varea, J. Sempau, E. Acosta, and J. Baró. *Nucl. Instr. and Meth. B*, 132:377, 1997.
- [57] K. B. Swartz, D. W. Visser, and J. M. Baris. *Nucl. Instr. and Meth. A*, 463:354, 2001.
- [58] J. F. Ziegler, J. P. Biersack, TRIM (2008.01), <http://www.SRIM.org>.
- [59] <http://www.isotopeproducts.com/>.
- [60] P. M. Endt, C. Alderliesten, F. Zijderhand, A. A. Wolters, and A. G. M. van Hees. *Nucl. Phys. A*, 510:209, 1990.
- [61] M. A. Meyer, I. Venter, and D. Reitmann. *Nucl. Phys. A*, 250:235, 1975.
- [62] Canberra. Detector specification and performance data, 2004.
- [63] P. W. M. Glaudemans and P. M. Endt. *Nucl. Phys.*, 42:367, 1963.
- [64] C. Angulo *et al.* *Nucl. Phys. A*, 656:3, 1999.
- [65] Saastamoinen *et al.* *Phys. Rev. C*, 80:044330, 2009.
- [66] M. Mukherjee *et al.* *Eur. Phys. J. A*, 35:31, 2008.
- [67] C. Iliadis, J. M. D'Auria, S. Starrfield, W. J. Thompson, and M. Wiescher. *Astrophys. J.*, 134:151, 2001.
- [68] M. A. Meyer, J. P. L. Reinecke, and D. Reitmann. *Nucl. Phys. A*, 185:625, 1972.
- [69] Saastamoinen *et al.* *J. of Phys. Conf. Ser.*, 202:012010, 2010.
- [70] J. José, F. Moreno, A. Parikh, and C. Iliadis. *Astrophys. J. Suppl.*, 189:204, 2010.